Master's thesis

Petrology and Economic Geology

Petrography, lithology, geochemistry and geochronology of the Takanen greenstone belt, eastern Finland

Nikolaos Karampelas

2022

Supervisors: Ville Järvinen, O Tapani Rämö & Tapio Halkoaho

Master's Programme in Geology and Geophysics

Faculty of Science

HELSINGIN YLIOPISTO
HELSINGFORS UNIVERSITET
UNIVERSITY OF HELSINKI
MATEMAATTIS-LUONNONTIETEELLINEN TIEDEKUNTA
MATEMATISK-NATURVETENSKAPLIGA FAKULTETEN
FACULTY OF SCIENCE

Tiedekunta – Fakultet – Faculty Faculty of Science	Koulutusohjelma – Utbildningsprogram – Degree programme Master's programme in Geology and Geophysics	
Opintosuunta – Studieinrikting – Study track Petrology and Economic Geology		
Tekijä – Författare – Author Nikolaos Karampelas		
Työn nimi – Arbetets titel – Title Petrography, lithology, geochemistry and geochronology of the Takanen greenstone belt, eastern Finland		
Työn laji – Arbetets art – Level Master's thesis	Aika – Datum – Month and year 03/22	Sivumäärä – Sidoantal – Number of pages 79

Tiivistelmä – Referat – Abstract

Archean cratons hold information of the early crustal development of the Earth, in conditions much different than the ones that exist today. Archean cratons consist of felsic plutonic rocks and greenstone belts. These belts are a useful tool for the understanding of the development of the early geological processes that shaped the Earth. There has been a variety of suggestions regarding the origin and geodynamic conditions that formed the Archean greenstone belts and there are several possible geotectonic scenarios that could form them. This thesis focuses on the Takanen greenstone belt found in the Karelia province in the Fennoscandian shield. The main objective of this study is to constrain the age of the greenstone belt, as well as to classify and group the formations found in it and compare it with its neighbouring, and much larger, Suomussalmi-Kuhmo-Tipasjärvi greenstone belt system - the biggest complex of its kind in the Karelian craton. A diamond drilling profile across the Takanen belt has been sampled. The various rocks found in the belt are divided into 5 groups based on their thin-section petrography and major and trace element geochemistry, outlining the general stratigraphy of the belt. There are also whole rock analyses that help to obtain major and trace element geochemical data for multiple samples from different locations throughout the belt. There are 3 calc-alkaline units (CALC1, CALC2, CALC3, named after their predominantly calc-alkaline nature) that include felsic, to intermediate volcanic/volcanosedimentary rocks and 2 units that consist of channelized komatiitic lavas and tholeiitic basalts (KOMBAS, named after the komatiites and basalts of the unit), olivine/olivine-pyroxene cumulates and high-Mg to tholeiitic basalts (OLIAD, named after the abundance of olivine adcumulates). The CALC1 unit is found lowest in the stratigraphy of the area and bares the oldest age of 2.95 Ga, while CALC3, which is the youngest formation of the belt, gives an age of 2.7 Ga. There is a direct correlation with the lowest CALC1 unit and the Luoma group in the Suomussalmi greenstone belt in terms of petrography, geochemistry and age, indicating that Takanen is the continuation of the Suomussalmi-Kuhmo-Tipasjärvi system to the north. Based on the initial Lu-Hf isotope composition of the dated samples, and the stratigraphic layering of Takanen, the oldest units in the belt originate from a process of continental rifting, while the youngest ones were most likely formed by a combination of continental rifting and some interaction of the continental crust with oceanic lithosphere. The Takanen greenstone belt lies on top of a large positive gravimetric and magnetic anomaly in the Koillismaa area called the ''hidden dyke'', composed of mafic-ultramafic cumulates and hypothesized to be related to the Paleoproterozoic Koillismaa-Näränkävaara Layered Intrusion Complex. The dyke and Takanen may not be genetically related, yet their overlapping existence points to a large crustal structure that served as a magma pathway throughout the Archean and the Paleoproterozoic. The potential of an economic orthomagmatic nickel deposit related to Takanen should not be completely overlooked, as there are some favorable indications in the geochemistry of the komatiitic units, as well as their possible interaction of these units with older sulphur rich units of the belt.

Avainsanat – Nyckelord – Keywords
Archean, greenstone belts, absolute age, Karelia, U-Pb zircon dating, komatiites, Ni - exploration

Säilytyspaikka – Förvaringställe – Where deposited
HELDA – Digital repository of the University of Helsinki

Muita tietoja – Övriga uppgifter – Additional information
This thesis was done in collaboration with the University of Helsinki and the Geological Survey of Finland

Contents

INDEX OF FIGURES

INDEX OF TABLES

INDEX OF ABBREVIATIONS

AGBs – Archean greenstone belts

BIF – Banded iron formation

BSE – Back-scattered electrons

CHUR – Chondritic uniform reservoir

GGMs - Granodiorites-granites-monzogranites

GTK – Geological Survey of Finland

HREEs – Heavy rare earth elements

ICP-OES - Inductively coupled plasma - optical emission spectrometry

ICP-MS – Inductively coupled plasma mass spectometry

LA-ICP-MS – Laser ablation inductively coupled plasma mass spectrometry

LILE – Large ion lithophile elements

LREEs – Light rare earth elements

KLIC - Koillismaa-Näränkävaara Layered Igneous Complex

MC-ICP-MS – Multicollector inductively coupled plasma mass spectometry

MORB – Mid-oceanic ridge basalt

PGEs – Platinum group elements

QQs - Quartz diorites-quartz monzodiorites

REEs – Rare earth elements

SEM – Scanning electron microscope

SKT – Suomussalmi – Kuhmo – Tipasjärvi

TAS – Total Alkali versus Silica

TGB – Takanen greenstone belt

TTGs - Tonalite -trondhjemite-granodiorites

UVD - Ultra-variable-pressure detection

XRF - X-ray fluorescence

1. INTRODUCTION

Archean greenstone belts have been traditionally investigated for both academic and economic reasons. They provide information regarding the formation and growth of Archean terrains and help explain the evolution of the early Earth (Kröner 2010). Understanding them in terms of age and stratigraphy, also means understanding the early procedures of the planetary plate tectonics. In addition, greenstone belts are important for economic reasons, as they host many types of mineral deposits, (mainly komatiite-Ni, orogenic Au, Cu, Ag and the PGEs) (Condie 1981)

Greenstone belts are typically long, curvilinear accumulations of various rocks, surrounded by large granitoid complexes (Condie 1981, Thurston 2015). They are a mesh of ultramafic, mafic, and sedimentary rocks. They are formed in areas of collisions or rifts in Archean terrain although some argue that Archean and early Precambrian greenstone belts can be related to mantle plumes (Dostal and Mueller 2013). Due to their complex nature and heterogeneous composition, greenstone belts offer more data regarding the time of activation of the lithospheric plate margin compared to the more homogenous granitoids that usually surround them.

Furthermore, greenstone belts offer valid targets for mineral exploration as they are rich in nickel, copper, iron, gold, and PGEs (Naipal et al. 2019). Their main commodity is komatiite nickel deposits. These deposits are formed when the Ni rich komatiite flow assimilates sulphur from surrounding rocks and Ni-sulphides accumulate gravitationally (Lesher and Groves 1986). Other types of mineralisation are generally associated with structurally controlled lodes, shears, and quartz veins and they can carry a considerable amount of metals (Fallon et al. 2010).

The Takanen greenstone belt (referred to as Takanen or the TGB) is located in Northern Finland, 50 km south from the town of Kuusamo, in the Archean Karelian province in the Fennoscandian Shield (see Figs. 1 and 2). It took its name from the Takanen lake that covers most of the greenstone belt. The belt is located 30 km north of the Suomussalmi-Kuhmo-Tipasjärvi greenstone complex (referred to as SKT). This complex extends north to south and is 220km long. The rock formations in the TGB are roughly similar to the ones found in SKT (Iljina 2003, Lehtonen 2016) and it is hypothesized that Takanen is the continuation of the SKT system to the north.

Takanen is also located between the mafic-ultramafic layered intrusions of the Paleoproterozoic Koillismaa-Näränkävaara Layered Igneous Complex (referred to as KLIC) (Alapieti 1982, Karinen 2010, Järvinen et al. 2020, 2021). Location of Takanen relative to the KLIC is interesting (see Figs. 1 and 2), as Takanen overlaps a 50 km long linear geophysical anomaly (the hidden dyke, see Fig. 3) that connects the intrusions of the KLIC and is speculated to represent a large-scale magmatic feeder channel for the Paleoproterozoic magmatism that formed the KLIC. (Alapieti 1982).

Takanen has been known since the 1990's as an area of potential academic and economic interest (Iljina et al. 2006). The greenstone belt has been sampled as part of an exploration project which targeted igneous complexes and possible Ni-PGE-Cu and Au mineralisation (Iljina 2003). The main work of the project included diamond drilling, geophysical surveys, and geological mapping, yet no stratigraphical interpretations or geological correlations where attempted. This MSc thesis is the first in depth investigation on the petrology and chronology of the Takanen belt.

In an attempt to intersect the geophysical hidden dyke anomaly, the 1.4 km deep drill hole R339 was drilled (later extended with daughter-hole R339B), collared within the Takanen belt (see Fig. 4) (Iljina et al. 2006). From top to bottom, R339 first intersected an intermediate volcanic layer, then a thick sequence of mafic volcanic rocks, then two Fe-sulphide rich layers and lastly a sequence of felsic volcanosedimentary rocks in contact with the Archean granite-gneiss basement complex. Results of a magnetic downhole measurement suggested that the hidden dyke is somewhat offset and not directly under the greenstone belt rocks as previously thought. In addition, a density measurement performed in R339, suggested that the feeder dyke is actually deeper than believed, at around 1500 m (Iljina et al. 2006).

Despite of the sampling procedures that took place in the area, Takanen remained without further investigation until 2020, when new drilling took place with a clear aim to discover and sample the aforementioned feeding system. The drilling was performed about 20 km to the west of the TGB. The hidden dyke was finally intercepted at a depth of 1400 m. (Karinen et al. 2021) but the data from that research was not used in this thesis.

It is clear that the possibility of the Takanen greenstone belt being Archean creates interest, as the area may give information regarding the evolution of the Archean Finnish terrain. The belt may also be a potential target for Ni- exploration, as 1) it hosts komatiitic olivine cumulates, which are typical host-rocks for komatiite-hosted Ni-deposits (Barnes et al. 2004), and 2) some

units in the Takanen stratigraphy are rich in volcano-sedimentary sulphides, presenting a potential S-rich wall-rock for younger Proterozoic magmas to assimilate sulphur from (Barnes et al. 2015).

The main purpose of this study is to give age constrains to the Takanen greenstone belt, as well as to characterize the rock formations found in the area. This may (1) give insight to the origin of the belt, (2) clarify its possible connection to the neighbouring greenstone belts found in the Karelia province, and (3) be used in conjunction with other studies to further understand the complex geology of the Archean in Finland.

In addition, understanding the stratigraphy of the Takanen belt as well as its age can provide information on the mineral potential of the area.

2. GEOLOGIC SETTING

2.1. General Geology of the Karelian Province

Takanen is located in the Taivalkoski block of the Archean Karelian province (simply referred to as Karelia) in the north-east part of the Fennoscanian shield (Hölttä et al. 2012). The Karelian province represents most of the bedrock of eastern Finland and extends to the western part of the Kola Peninsula, Russia (Fig. 1). The contact between Karelia and Kola is a décollement zone (namely the Belomorian mobile belt) where the granulites of Lapland have been thrusted south-westward over the Karelian rocks (Vaasjoki et al. 2001, Sorjonen-Ward & Luukkonen 2005).

The bedrock of the province is mostly formed of 3.5 to 2.6 Ga granitoids. The oldest rocks are located in the west and north sections of the province. The granitoid rocks are classified into four groups (Hölttä et al. 2012):

1. tonalite -trondhjemite-granodiorites (TTGs),
2. sanukitoids,
3. quartz diorites-quartz monzodiorites (QQs) and
4. granodiorites-granites-monzogranites (GGMs).

The TTGs are separated into high-HREE and low-HREE groups, which marks a difference in the depth of melt formation. The sanukitoids are related to partial melting of a metasomatized

subcontinental mantle. The GGMs originated from partial melting of the TTG crust. In addition to the granitoids, the basement complex is interrupted at times by medium-grade greenstone and metasedimentary belts (Hölttä et al. 2012). In Karelia, there are amphibolite layers from basaltic and andesitic protoliths in the TTGs, as well as evident migmatization of the original igneous rocks. The basaltic rocks are LREE-depleted, pointing to a mid-ocean ridge origin. (Hölttä et al. 2012). The andesitic rocks are enriched in LILE and LREE and represent dykes with some crustal assimilation. In essence, the Archean of Karelia is an amalgamation of TTGs and greenstone belts (Hölttä et al. 2012).

The general area of Taivalkoski (where Takanen is found) consists of the TTGs of the Karelian province. These TTGs have ages of 2.83-2.72 Ga, and primarily belong in two age sub-groups the older being 2.83-2.78 Ga and the younger 2.76-2.72 Ga, thus creating a 20 Ma gap between the sub-groups (Hölttä et al. 2021)

Fig. 1: Composite map of the Karelian province showing the Archean TTGs and major greenstone belts. The red arrow points to the location of the Takanen greenstone belt (Shown here as TK). Modified after (Huhma et al. 2012).

2.2. Greenstone belts

2.2.1. Geological characteristics

Greenstone belts are composed of metamorphosed ultramafic or mafic volcanic sequences and also include volcanosedimentary rocks. They are mostly Archean (Vearncombe 1986), although some have formed during the Paleoproterozoic, like for example the Central Lapland (Hanski and Huhma 2005) greenstone belts, which are typically situated within Archean

cratons and are surrounded by granitoids or felsic gneiss. The length of a greenstone belt can range from less than a hundred to a few thousand km's.

The belts primarily consist of basalts and komatiites, the latter defined as extrusive rocks with over 18 wt.% Mg (Le Bas 2000, Arndt and Lesher 2004). Other rock types commonly found are felsic to intermediate volcanosedimentary rocks as well as banded iron formations (BIFs). Felsic dykes are also commonly found (Huhma et al. 2012). The felsic volcanic and volcanosedimentary beds in a greenstone belt can be representative of the felsic complexes surrounding the belt, but in various cases they are found in large unconformities on top of the basement complex, making the identification of their origin much harder (de Wit & Ashwal 1995).

Greenstone belts are dynamically active systems and thus most of them have been subjects to deformation. The belts are oftentimes metamorphosed to gneiss and schists. Overall, the term greenstone derives from the metamorphic minerals commonly found in the formation, namely amphiboles (actinolite-tremolite series) and chlorite (Vearncombe et al. 1986).

Greenstone belts are often associated with sulphide ores mainly komatiite nickel, as well as other commodities like gold, iron, copper and platinoid elements. Komatiite-hosted Ni deposits are produced because of the komatiite flows interacting with underlying rocks (such as the Archean felsic rocks surrounding the belt) that are rich in sulphur. The occurring sulphides are separated from the olivine cumulate gravitationally. This increases the research interest, as greenstone belts are good potential targets for mining exploration.

2.2.2 Genesis of greenstone belts

The granitoids that include the greenstone belts are quite homogeneous and the rocks are at least locally of a unified origin, without much variation of differentiation at an exploration scale. On the other hand, the wide variety of rock types present in greenstone belts, reflects different evolutionary formation conditions and widespread metasomatic, metamorphic, deforming and mineralization effects. This makes greenstone belts better markers of lithospheric events than their granitoid hosts (Anhaeusser 2014). Greenstone belts represent a sort of scar that indicates the area of an ancient spreading or collision. Thus, understanding the origin and lithological content of greenstone belts is a key factor to understanding the geological history and evolution of the planet during the Archean.

The genesis of greenstone belts is a complicated process and many different models and mechanisms have been suggested for their formation (Lehtonen 2016 and references therein). There are two distinct petrotectonic paradigms with lithosphere movement dominated by either a vertical or a lateral component (Stein & Hofman 1994, Benn & Moyen 2008, Vogt & Gerya 2014). The main contention between the two models arises from different opinions regarding the maturity (in terms of temperature, composition and thickness) of the Archean lithosphere and the time when modern-style subduction began. (Lehtonen 2016, and references therein).

The main mechanism in the vertical lithosphere movement is the stagnant lid model, which suggests that the upwelling of the mantle happened through diapirs and/or mantle plumes with different levels of crustal contamination. This would be the most primitive form of mantle derived volcanism. According to Sm-Nd isotope data, this was a possible situation before 3.0 Ga (Stein and Hofman 1994, Debaille et al. 2012).

Models for lateral lithosphere movements include the subduction model (see below) and the flat subduction model. The flat subduction model is similar to the modern situation (that occurs in subduction zones), but with a shallower angle of the subducting warm (buoyant) plate, and without the formation of a mantle wedge (e.g., Abbot et al. 1994, Smithies et al. 2003). In this case, the melts formed by the melting of the slab at a shallow depth can form TTGs. This model has been argued against, using numerical modelling by van Hunen et al. (2004).

At this point it must be noted that greenstone belts originating from mantle plumes, may inherit a ‘‘pseudo-subduction’’ geochemical signature if they are contaminated by continental crust, evident through Ta and Nb depletion and enrichment in Th (Tomlinson and Condie 2001). This is an issue that can make the distinction of the origins of greenstone belts somewhat harder.

The subduction model is basically the one that appeared the latest and has been active until today. It is powered by the slab pull, as a cool plate subducts under the continental crust. The subducting plate is recycled in the mantle/core boundary. The diverging plates form mid-oceanic ridges where the mantle is able to reach the surface in forms of ophiolites. There has been disagreement regarding the percentage of Archean greenstone belts having formed due to subduction. The argument is concerning the way that the mafic rocks were formed and the way the linear belts were emplaced in their final position. Furnes et al. (2015) used geochemistry of immobile elements in basalts to estimate that 85% of the formation of the greenstone belts is due to subduction. This is disputed by other scientists that point out the fact that geochemistry alone cannot be a decisive factor for tectonic models, as there can be similarities between rocks

of different geotectonic environments (e.g., van Hunen & Moyen 2012), and others use the example of modern-day basalts that share very similar geochemical traits, even though they are originating from different environments. Li et al. (2015) and van Hunen & Moyen (2012), suggest that subduction was present in the Archean but only partially as a proto-subduction zone. This means that there were some small local subduction zones, that did not fully extend to their modern-day analogue and there was only a percentage of slab pull.

Although their general stratigraphy is similar, Archean and Proterozoic greenstone belts can differ in composition. Archean greenstone belts generally have more ultramafic material whereas in Proterozoic belts the volume of the ultramafic volcanic rocks decreases, in favour of more sedimentary rocks (Condie 1981, 1994). This is related to the maturity of the plate tectonics in the Proterozoic, and the fact that MgO rich melts form in higher mantle temperatures than the ones found in modern Earth (Nisbet et al. 1993). The composition of komatiites also differs between Archean and Proterozoic greenstone belts. The Archean komatiites are MgO richer as they are products of a hotter mantle and hence, higher degree of partial melting.

During the Proterozoic, most magmatic events took place around already formed cratons, with recycling of the crust and the plate tectonics being similar to how they are today. This means that there are more processes that can cause the formation of a greenstone belt. Thus, there is a greater variety of formations related to Proterozoic e.g., the Proterozoic greenstone belts of the West African Shield, that contain a variety of felsic to mafic components, but no komatiite flows (Attoh 1986). These newer, Proterozoic belts can contain tholeiitic MORBS, komatiites, deep-marine sediments turbidites shales, towards epiclastic sediments sandstone carbonatites and calc-alkaline arc-volcanics, alongside the mafic to intermediate intrusions.

2.3. Greenstone belts in the Karelia

The Archean greenstone belts in Karelia consist of komatiites, mafic dykes, other volcanic rocks, and felsic volcanosedimentary interlayers, while some cherts, BIFs and sulphide-rich units can also be present (Condie 1981). The belts are not tied to one specific geodynamic setting. They can be related to subduction, collision, continental rifting or mantle plumes (in some cases) (Bibikova et al. 2003).

The prominent Archean greenstone belts in Karelia are the Suomussalmi-Kuhmo-Tipasjärvi belt and the Illomantsi belt.

The Suomussalmi-Kuhmo-Tipasjärvi complex (referred to as SKT) has a typical age of Archean greenstone belts in Finland at 2.94-2.79 Ga (Lehtonen 2016 and references therein) and is probably partially related to continental rifting (Luukkonen 1992).

The Suomussalmi belt, which is the northernmost part of the SKT system, is approximately 70 km long and 10 km wide. The belt has been dated, using the U-Pb on zircon method, and is somewhat older than the rest of the SKT complex, with four age groups of 2.94, 2.87, 2.84 and 2.82 Ga (the first two found only in Suomussalmi). Sm-Nd isotope data also indicate that the Suomussalmi belt originates from an older source than the Kuhmo and Tipasjärvi belts (Lehtonen et al. 2016b). The Illomantsi belt is younger than other Archean greenstone belts in Karelia with an age range of 2.76-2.72 Ga (Sorjonen-Ward & Luukkonen 2005).

2.4. General geology of the Takanen greenstone belt

Takanen greenstone belt is located about 30 km directly north of the Suomussalmi greenstone belt (Fig. 1). Takanen is oriented East to West and is about 3-4 km long. It is mainly a volcanosedimentary formation, but also has mafic and felsic volcanic rocks as well as komatiites. Some banded iron formations have been reported nearby in the area of Korpuajärvi. The belt is completely surrounded by an Archean granite-gneiss complex. It overlaps with a large gravimetric anomaly, possibly related to 2.45 Ga mafic layered intrusions also present in the area (see Figs. 2 and 3).

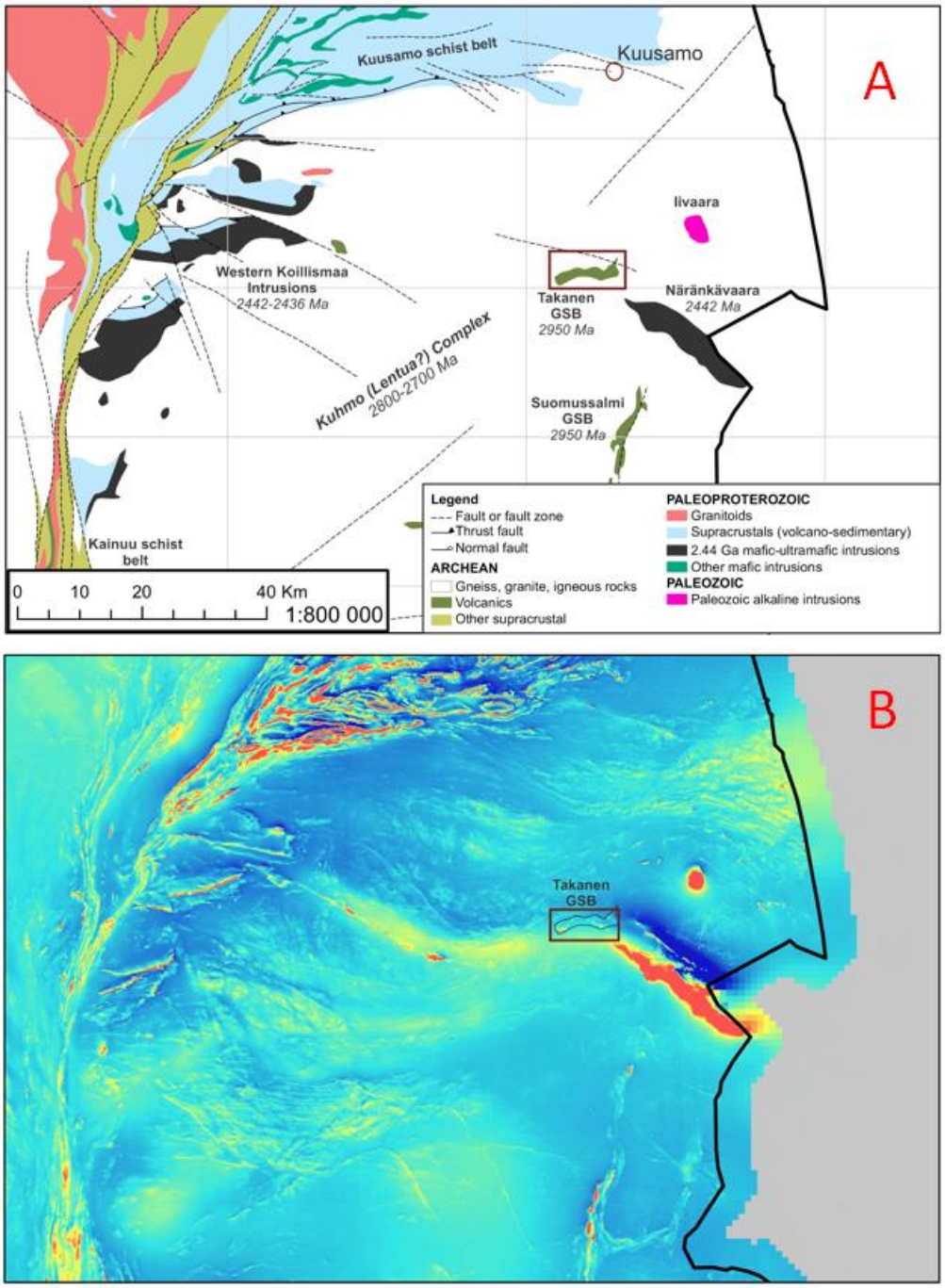

Fig. 2: A: Geological map showing the simplified geology of the Koillismaa area, including Takanen shown in the red box, as well as some known absolute ages and major fault shear zones in the extended area. B: The aeromagnetic map shows the same area and the large-scale gravitational anomaly that goes underneath Näränkävaara and Takanen end extends to the west. Age references: Näränkävaara (Järvinen et al. 2022), Suomussalmi (Lehtonen et al. 2016b), Koillismaa (Alapieti 1982), Kuhmo Lentua complex (Hölttä et al. 2012), Takanen (this study). Adapted after (Bedrock of Finland, DigiKP – Seamless bedrock map of Finland by the GTK. Coordinate system euref fin).

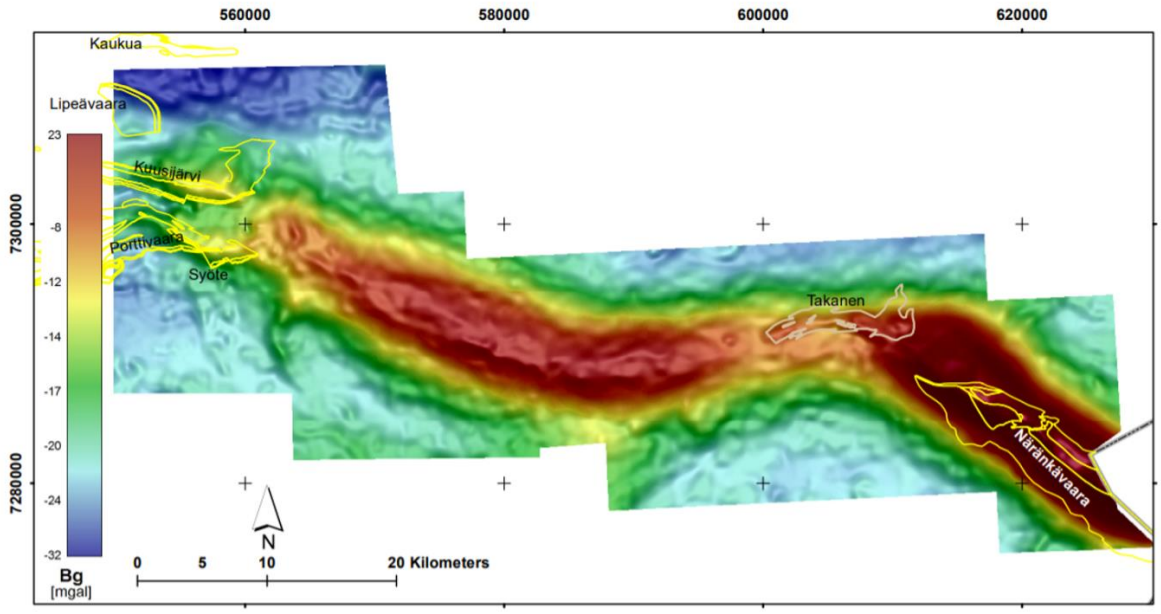

Fig. 3: Geophysical map showing the major gravitational anomaly in the Koillismaa area with Takanen and Näränkävaara outlined. Figure courtesy of Heikki Salmirinne (GTK).

3. MATERIALS AND RESEARCH METHODS

3.1. Materials

The materials utilised for this research project mostly come from previous samplings performed by the Geological Survey of Finland (Iljina 2003). Outokumpu Mining Exploration has also performed drilling in the area (Vesanto 2003). The main material to work with is drill core. A total of 32 drill holes have been made in the study area (labelled in Fig. 4), with a total length of 4 km. A total of 200 hundred thin sections have been made, representing all major units in the drill core. During the sampling for the thin sections, points of lithological contacts were emphasised. There are thus representative samples from points of interest for understanding the relationships between the rock formations. All drill-core has been logged and thus the whole-rock geochemical data accurately represents the units found in the TGB. Data produced from geophysical surveys in the area have also been used in order to assess the structures of the study area.

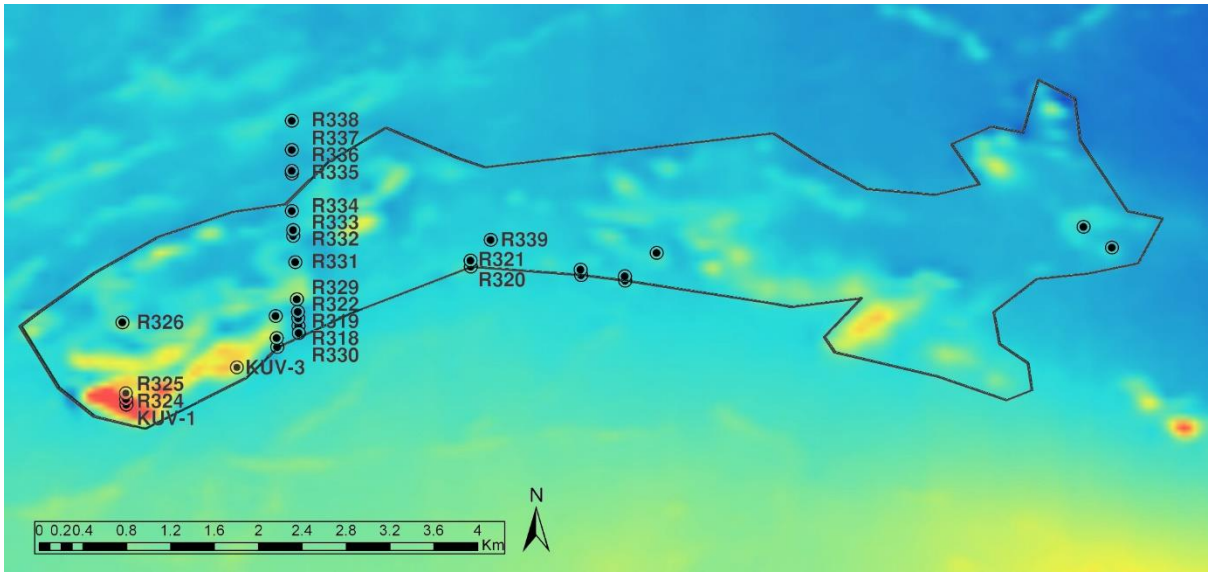

Fig. 4: Close up of the aeromagnetic map from Fig. 2 that shows the outline of the Takanen greenstone belt, including the drill hole names. The main drilling profile was used to group the various units of the belt complimented by the deep R339 hole. Figure made by Ville Järvinen.

3.2. Methods

3.2.1. Field work

A short field trip in the area took place in late July 2020; however, the research team was unsuccessful in locating outcrops, finding boulders or collecting hand samples. The area surrounding the Takanen lake consists mainly of forest and swamp terrain, which renders sample recovery almost impossible. A few boulders were present in the area; however, they were glacifluvial and were not studied further as they most likely do not represent the bedrock underneath. The Suomussalmi belt was visited in order to study known formations, with probable similarity to the TGB. The outcrops that were observed included komatiite flows, altered pyroxenites, pillow lavas, well researched mineralisation areas and other basaltic lava flows. In addition, 2.94 Ga felsic to intermediate volcanosedimentary rocks in the Luoma area were visited. This visit aided to understand the geochemistry better and to create a better image of the general situation of the belt, which simplifies classification via petrography and geochemistry.

3.2.2. Petrography

Optical petrography was used to study all 200 thin sections. The purpose was to make a classification for the existing rock types. The original drill core procedure created a very

complex early rock-type classification. This was also partially because the core had been logged by different people, making the logs prone to some inconsistencies. Bearing this limitation in mind, the lithological classification in this work is based on drill core logs combined with thin-section petrography with whole-rock geochemical classifications, to give a clear view of what kind of rock type the samples represent.

Another impactful part of the petrographic examination was the utility it brought when it came to look for possible samples for zircon separation and dating. In accordance with the geochemical data provided, three possible drill core intersections for zircon sampling were chosen, as shown later in the zircon isotope analyses paragraph. These intersections showed high zircon concentrations in whole-rock, and zircon grains were visible in thin sections as well, making it easier to judge that the sample was suitable for zircon separation. Because of the nature of greenstone belts and the many metamorphic events that have occurred in Finland, it is possible that at least some of the zircons found are inherited. Therefore, it was crucial to look for volcanic structures in the potential rock samples. The selected sampling intervals represent intermediate to felsic volcanic rocks with high zircon contents, enough to sometimes be visible in the optical microscope. There were many more small crystals found as inclusions (mostly in biotite) and distinguished from their radioactive halo.

3.2.3. Whole-rock geochemistry

Whole-rock geochemical analyses for the samples were previously performed at the Labtium Oy in Finland. Total numbers of whole-rock analyses available for Takanen are 200 X-ray fluorescence spectroscopy (XRF) analyses, 150 Inductively coupled plasma mass spectometry (ICP-MS) analyses (for REEs and trace elements), 350 partial leach Inductively Coupled Plasma Optical Emission Spectroscopy (ICP-OES) analyses (for base metals) and 400 Au+Pd+Pt analyses (Iljina 2003, Rasilainen et al. 2007). Sometimes more than one method is available for a single drill core sample and, depending on the element of interest each time, the correct one should be selected. The software ioGAS-64-7.2 was utilised to classify the rocks based on their geochemical characteristics. For the analytical results for major elements and some important trace elements for this work, refer to table 4 in Appendix 9.2.

3.2.4. Zircon isotope analyses

For the purpose of dating of the Takanen greenstone belt with the zircon U-Pb method, 3 drill core intervals were selected for zircon separation by means of thin section petrography and whole-rock geochemical characterization. The priority targets were igneous felsic-intermediate rocks, in order to get higher zirconium concentrations. These rocks would ideally be found as interlayers between mafic lavas. This means that they represent a part of a continuous volcanic activity with different acidity.

Drill core intervals selected for zircon separation are listed below. See Fig. 4 for drill core locations and Figs. 5 and 13 for sample locations (see also Figs. 22, 24 & 25 in Appendix 9.1 for drill core pictures)

a) M452398R318 (R318) at a depth 23.90-26.9m.

b) M452398R339 (R339) at a depth of 277-279 m.

c) M452398R332 (R332), at the depth of 61.5-63.6 m.

Sample preparation: Sample preparation and analyses were performed by the Geological Survey of Finland (GTK). The samples were washed, crushed and separated for heavy minerals, using a methylene iodide liquid. The separation from magnetite took place in an isodynamic separator (Frantz; 0.5A and 1.4A). The zircon crystals were then handpicked with the aid of a binocular microscope. The crystals were mounted in epoxy and then polished.

Laser ablation inductive coupled mass spectrometry: The selected method to date the TGB was U-Pb analysis on zircon, utilizing the LA-ICP-MS method (Kröner et al. 2014).

U–Pb dating analyses were performed using a Nu Plasma AttoM single collector ICPMS connected to a Photon Machine Excite laser ablation system at the Geological Survey of Finland in Espoo. Samples were ablated in He gas (gas flows = 0.4 and 0.1 l/min) within a HelEx ablation cell (Müller et al. 2009). Typical ablation conditions were: beam diameter: 25 μm, pulse frequency: 5 Hz, beam energy density: 2.17 J/cm2. A single U–Pb measurement included a short pre-ablation, 10 s of on-mass background measurement, followed by 30 s of ablation with a stationary beam. ^{235}U was calculated from the signal at mass 238 using a natural $^{238}U/^{235}U=137.88$. To minimize the effects of laser-induced elemental fractionation, the depth-to-diameter ratio of the ablation pit was kept low, and isotopically homogeneous segments of the time-resolved traces were calibrated against the corresponding time interval for each mass

in the reference zircon. Plotting of the U-Pb isotopic data and age calculations were performed using the Isoplot/Ex 3 program (Ludwig 2003). It was decided to also perform analysis for Lu-Hf isotopes alongside the U-Pb analysis. The isotopic composition of this system aided to decipher if the zircons found in the samples are magmatic, not inherited (Andersen 2012) and in combination with the SEM imaging, minimized the possibility of a sample selection error.

The main results of the analysis were the isotopic compositions of U and Pb in the zircons (see tables 2 & 3 in Appendix 9.2). These were used to compile Concordia plots in order to calculate the age of the samples and that of the TGB with the aid of Isoplot 3.00, a tool for geochronological calculations in Microsoft Excel (Ludwig, 2003**)** The samples do not belong in the same stratigraphic areas in the overall column, so the result is a range of ages spanning across the time that the TGB was active.

Lu-Hf isotopic compositions: The Lu-Hf compositions of the zircons analysed for U-Pb data were determined with the use of a Nu Plasma Hr multicollector ICP-MS at the GTK labs in Espoo. The ablations were targeted as close as possible to the original U-Pb ablation spots for better accuracy. The samples were ablated in a helium gas chamber within a HelEx ablation cell (Müller et al. 2009). The parameters for the analyses were: beam diameter: 50 mm, pulse frequency: 5 Hz, beam energy density: 3-3.8 J/cm2. Isotope data was collected for (^{173}Yb, ^{175}Lu, ^{176}Hf-Yb-Lu, ^{177}Hf, ^{178}Hf, ^{179}Hf). The ratios were measured through the use of the Nu Plasma time-resolved analysis software and later calculated via an Excel spreadsheet (provided by Yann Lahaye of the GTK). The filtering for the data was at 2s and was corrected for mass discrimination. For the calculation of the Hf mass ^{179}Hf/^{177}Hf=0.7325 was assumed. The effect for the Yb correction was evaluated on a GTK standard LV11 (Andersen et al. 2019), as it presents similar Yb/Hf ratios with the zircons selected from the study area. The value 0.7961 for ^{176}Yb/^{173}Yb (Chu et al. 2002) was utilised for the correction of the Yb interference on ^{176}Hf. Similarly, the 0.02656 value for ^{176}Lu/^{175}Lu was used to correct for the Lu interference on ^{176}Hf (Scherer et al. 2001, Vervoort et al. 2004). The decay constant of ^{176}Lu was 1.867×10-11 a-1 used throughout the calculations (Söderlund et al. 2004; Scherer et al. 2001, 2007).

The εHf values calculations were done based on present-day chondritic ^{176}Hf/^{177}Hf=0.282785 and ^{176}Lu/^{177}Hf=0.0336 (Bouvier et al. 2008). The standards were run as unknowns. The average ^{176}Hf/^{177}Hf value of LV11 was 0.28284±10 (2-sigma, n=17, which is just within error with the results obtained by solution analyses MC-ICP-MS by Heinonen et al. (2010) the value if which is 0.28283±3. This method was run and presented by Yann Lahaye of the GTK.

For the initial Lu-Hf isotopic analyses results, refer to table 1 in Appendix 9.2.

3.2.5. Scanning electron microscope (SEM)

The imaging of the zircons was performed using the SEM microscope JEOL JSM 5900 LV SEM model. During the procedure, the primary X-ray produced by the instrument interacts with the sample and produces backscattered electrons that are collected from the instrument's sensors. This creates an accurate picture of the sample and more specifically the possible zoning in the zircons. This is important for understanding the origin of the zircons and also to decipher which is the best area of the zircon to target for laser ablation, to extract the U-Pb data. There were two types of imaging collected from the procedure, namely Back-Scattered Electron (BSE) and ultra-variable-pressure detection (UVD) images.

3.2.6. Geophysics

The existing geophysical data were used to assist with the interpretation of the setting of the greenstone belt. The data was mainly utilized to get a better understanding of the relationship of the system with its mafic feeder dyke, which lies underneath it (see Fig. 3) and also show how deep below the surface the dyke is (Salmirinne and Iljina 2003). All this will be valuable information for the understanding of the TGB in terms of origin and geological setting (cf. de Beer 1991).

4. RESULTS

4.1. Rock classifications

Given the lack of outcrops in Takanen the rock classification given here is based on the drilling profile across the short axis of the Takanen belt (Fig. 4). A cross section (Fig. 5) and stratigraphic column (Fig. 13) have been compiled, based on drill core logs and photographs as well as whole-rock geochemical classifications and thin section petrography. The classification contains gaps in areas where thin sections or whole-rock geochemical analyses

are not available. The cross section in Fig. 5 shows the rock units that appear in the main profile and represent the general lithology of the TGB. The tectonic structures are used as the explanation of abrupt changes in the continuation of the stratigraphy.

The TGB consists of the following rock types: Felsic to intermediate volcanosedimentary rocks, intermediate volcanic rocks, tholeiitic basalts, high-Mg basalts, komatiites and olivine adcumulates. Based on the geochemical data as well as petrography the rocks of the TGB can be unified into 5 stratigraphic units. Three felsic to intermediate volcanic units named CALC1, CALC2, CALC3 based on their predominantly calc-alkaline origin, a mafic-ultramafic unit given the joint name KOMBAS after its abundance in komatiites and tholeitic basalts and a mostly ultramafic unit with some mafic layers, named OLIAD as it consists mainly of olivine and olivine-pyroxene cumulates. The units are layered from bottom to top in this order: CALC1, KOMBAS, CALC2, OLIAD, CALC3 as can be seen in Fig. 5.

4.1.1. Location

CALC1 is the southernmost unit on the surface, appearing first at the upper part of R330. This unit is the lowest stratigraphic part of the TGB, and it is positioned exactly on top of the Archean basement plutons. The sample that was used for U-Pb dating from drill hole R339 was selected from the same corresponding unit and thus represents the earliest formed igneous layer of the stratigraphic column of Takanen (see Fig. 13). CALC1 extends throughout the profile and reappears at the northern part of the belt in drill hole R336 (see Figs. 4 & 5) as part of a large-scale syncline that extends in the main part of the belt.

KOMBAS is deposited right above the CALC1 and on the surface is found immediately to the north of CALC1. It first appears close to the surface lever at R318 and continues to the north. It also resurfaces at the northernmost part of the TGB at drill hole R336 (see Figs. 4 & 5) right above the CALC1 layer.

CALC2 is the next series of calc-alkaline rocks and is emplaced on top of KOMBAS. This effectively makes KOMBAS an interlayer between CALC1 and CALC2. CALC2 is very similar to the CALC1 unit geochemically wise. Bearing this in mind, the main criteria for separating the two units is the fact that the KOMBAS1 layer is found between them in all circumstances where they appear (Figs. 5 & 13).

OLIAD appears in the main profile as a small unit that is found exclusively on the shallowest parts of R329. Stratigraphically it is placed above CALC2. In the main drilling profile, there is only one sample of the OLIAD unit, but it appears to its full extend in the KUV1 and KUV3 drill holes nearby (see Figs. 4 & 5)**.**

CALC3 appears at R331 and continues on the entirety of R332 and the upper part of R333. It is most likely the top part of the stratigraphy of Takanen and defines a syncline structure with the main fold axis being in the middle of the drilling profile. The sample used for U-Pb dating that was taken from R332 is representative of this stratigraphic unit. CALC3 appears continuously near the surface, and it expands from R331 to R332 to R333 and then is lost (Fig. 5).

It needs to be mentioned that at the lowermost part of R333 another mafic layer is found (see Figs. 4 & 5) This layer is exclusive to this area, and it is almost impossible to correlate with any other of the existing units. This unit has been logged as ultramafic rock but petrographic examination as well as the geochemical data disagree with this statement. This layer is apparently a tholeiitic basalt.

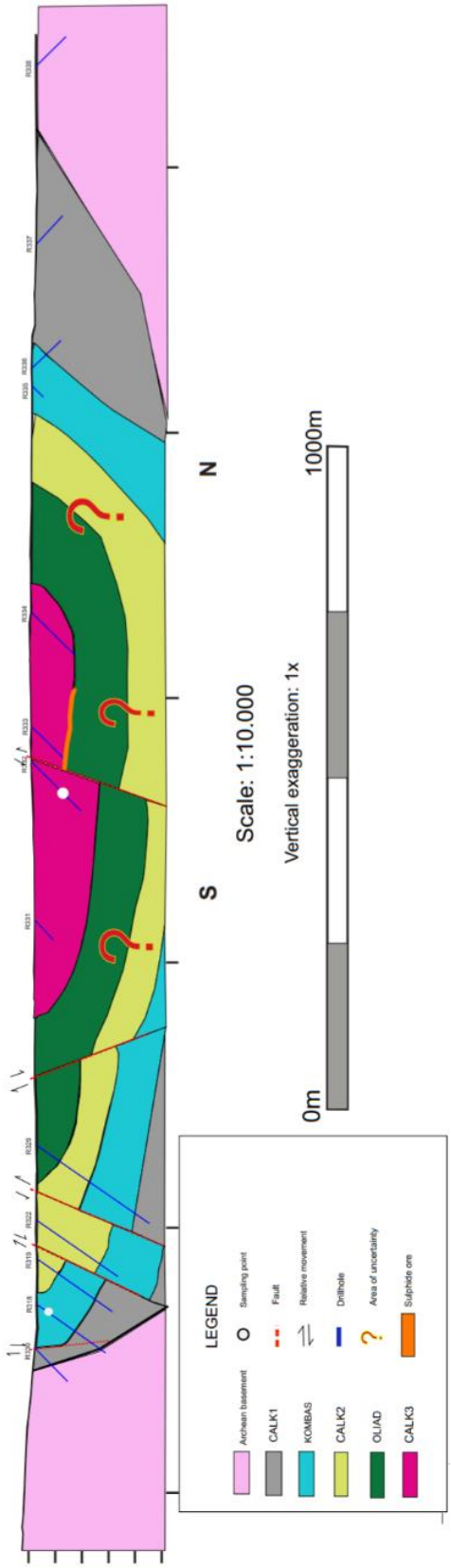

Fig. 5: The geological interpretation of the TGB. The structural components, namely the large syncline and the faults and relative movements have been proposed to explain the way the units are placed in the TGB. The different orientation of the drill holes (southern holes dipping south and northern holes dipping north) enhances the possibility of a syncline structure. Notice the large area of uncertainty in the middle of the main drilling profile due to the lack of available data. The cross-section also shows the areas of sampling for U-Pb at drill holes R318 and R332.

4.1.2. Petrology and petrography

At the base of CALC1 there is a smooth transition from Archean granite gneiss to the first felsic-intermediate rocks of the actual unit. CALC1 rocks range from intermediate to felsic being mostly dacites, rhyolites or andesites in composition. The unit seems to retain some of its primary bedding but is also heavily folded. The rocks show distinct foliation but retain the primary igneous minerals and textures. In some samples, large plagioclase phenocrysts define an especially evident porphyritic texture. Porphyries are mostly found in samples from the R339 drill hole (see Fig. 6 and also Fig. 22 Appendix 9.1). Textures, however, can vary throughout the CALC1 unit, ranging from plagioclase-porphyric andesites to more equigranular quarztofeldspathic schists. No systematic layering is found in the unit, but dacitic samples often appear as interlayers between the more felsic rock types of the unit. The unit itself bears disseminated fine grained pyrrhotite, which at points becomes a massive interval with felsic inclusions. This massive interval is found near the contact of CALC1 with the predominantly mafic KOMBAS unit above it. The zircon dating sample that gave the oldest 2.95 Ga age was collected from drill hole R339 at a depth of 277-279 m, near the contact of CALK1and KOMBAS. The CALC1 unit is penetrated by aplitic veins that have similar geochemical traits with the volcanic and volcanosedimentary rocks of the unit. Amongst the felsic veins there is also a xenolith bearing ultramafic vein logged as lamprophyre.

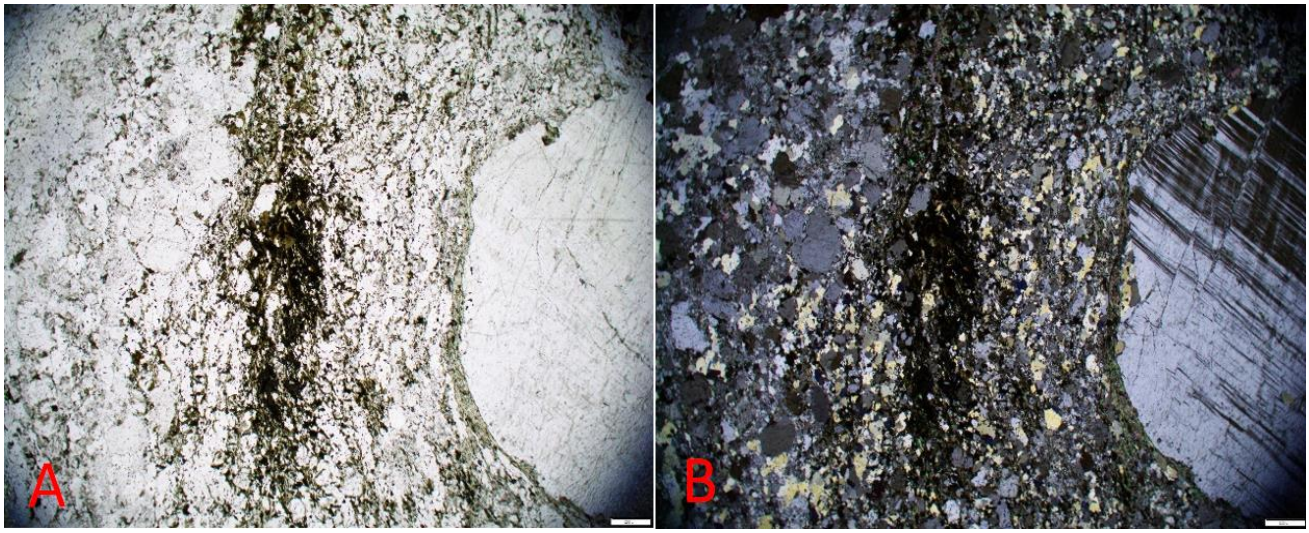

Fig. 6: Thin section photograph showing the petrography of sample R339 at 277.5 m depth. Picture A is taken in plain polarized light. Picture B is taken from the same area in cross polarized light. Notice the porphyric texture with the large plagioclase crystals among the matrix of other minerals. A zircon sample was taken from this interval in the drill hole resulting in an age of 2.95 Ga (sample b in text). The image is representative of the CALC1 unit. Scale for both images: 1 cm=200 µm

KOMBAS consists of komatiites, komatiitic basalts and high Mg tholeiitic basalts overlapping each other in cycles. The mineralogy contains mainly plagioclase and amphiboles (see Fig. 7 and also Fig. 23 in Appendix 9.1). There is clear foliation in the basaltic rocks of the unit and graded bedding is evident in some of the samples. Some residual olivine is still preserved in the komatiitic parts of the unit. There are also some intermediate volcanosedimentary layers in the unit (one of which was the selecting point for sample R318). The unit is penetrated by felsic pegmatitic veins.

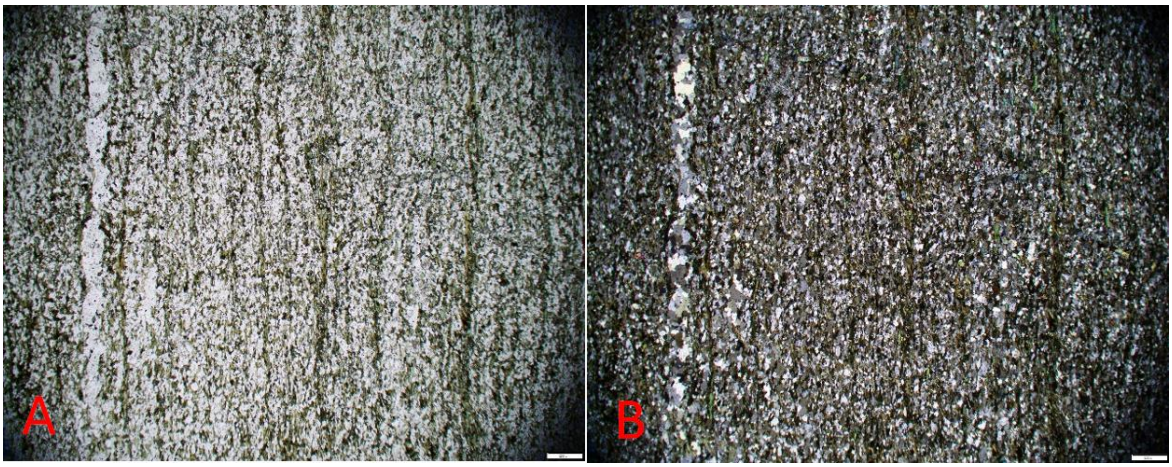

Fig. 7: Thin section photographs showing an intermediate volcanosedimentary petrographic thin section from around the depth of sampling from R318 belonging to the KOMBAS unit. Picture A is taken in plain polarized light. Picture B is taken from the same area in cross polarized light. This unit is not representative of the main bulk of the unit that mainly consists of mafic and ultramafic volcanic rocks. It was this reason that this specific area was initially considered ideal for U-Pb sampling as it is found in between two mafic volcanic layers and has very low risk of an inherited zircon age. Scale for both images: 1 cm=200 µm

CALC2 is a thinly interlayered unit that includes generally felsic to intermediate rocks with some sporadic appearances of more mafic samples. The main rocks are andesites, dacites and rhyolites. The upper part of the unit includes some more mafic calc-alkaline rocks that almost plot in the basalt field. The more mafic parts mostly include amphiboles and plagioclase with clear foliation in their mineralogical composition. At the lowest part of the unit, graded bedding is visible both in thin section and macroscopic scale. The felsic rocks of the unit consist mostly of biotite, quartz, plagioclase and feldspars. The more mafic ones consist of mostly biotite, plagioclase, amphibole and chlorite with distinct foliation. They generally retain their igneous porphyritic structure with very little to no foliation (see Fig. 24 in Appendix 9.1). The rocks of

the unit have been subjected to regional metamorphism in greenschist-facies conditions, as is evident from the foliation and the metamorphic minerals described above

OLIAD in the main profile appears as a single sample from an olivine adcumulate layer. Drill hole R329 lacks thin-sections, but according to the drill core log, the rock types of the hole consist of small grained olivine crystals which have been serpentinized and/or altered to talc in places. Some disseminated fine grained sulfides are present. The lower part of this adcumulate assemblage is schistose and amphibole-altered. The rocks from the drill holes KUV1 and KUV3, located to the east of the main profile, contain layers of similar olivine adcumulates amongst other ultramafic rocks. For this reason, they have been classified as part of the same unit. The full unit consists of komatiites and komatiitic/high Mg basalts. These coarse grained serpentinized rocks have been logged as a basal portion of a magma pulse/lava flow. The lower part (found in KUV1 hole) is a mafic volcanic rock that is heavily foliated and penetrated by a few felsic veins.

CALC3 is otherwise similar to CALC1 and CALC2, but unique in the sense that it is the only unit that contains garnets. The rocks are quartz-feldspar schists with geochemical traits of dacites. The lower part of the unit is massive and homogeneous and includes biotite (which is not present in the rest of the unit). Plagioclase throughout the unit is occasionally oval shaped and there are pyroclast like quartz-feldspar fragments, which is attributed as a primary volcanic texture. Some small garnets are present. The main bulk of the unit shows banding at points, with some garnet bearing beds at times alternating with quartz-feldspar biotite layers (see Fig. 25 in Appendix 9.1). There are also some calc-silicate amphiboles, garnet and disseminated pyrite bearing layers. The unit includes a quartz rich interval. A massive sulfide ore can be found at 35.95-37.17m depth (Fig. 5) which is almost exclusively pyrrhotite with a small inclusion (max 30mm) composed of fine-grained quartz, plagioclase, biotite, chlorite, and K-feldspar. A mafic dyke cuts through the rock at depth 98.80-99.10 which is schistose and amphibolised

4.1.3. Geochemistry

By studying the major oxide binary plots and the Jensen-diagrams (Jensen, 1976) that were drawn for every individual unit, the rocks can be divided into komatiites, komatiitic and tholeiitic basalts, and felsic to intermediate volcanosedimentary rocks ranging from andesite to rhyolite. The komatiites generally have high Ni and MgO (see Figs. 27 & 29 in Appendix 9.3). Komatiitic and tholeiitic basalts, however, are sometimes hard to distinguish as they bear

geochemical traits that could be products of different geotectonic environments. The FeO content of the basalts also seems to be variable without many visible trends, possibly due to variable oxidation states. There is, however, the signature of a tholeitic trend for some of the basalts, as seen in the Jensen diagrams that follow, showing the individual unit compositions. The Cr and Ni content of the basalts is relatively low and the Zr content follows a visible pattern (see Figs. 27 & 29 in Appendix 9.3). The intermediate rocks found in the different calc-alkaline units are chemically very similar as shown by the TAS diagrams (Figs. 7, 9 & 11) and the Jensen diagrams shown in figures (Fig. 7, 9 & 11). Their SiO_2 ranges from 55 to 65 wt.%, and they show higher Ti content higher than the felsic rocks described below. The Aluminium content can be quite variable in the samples from CALC2, but it shows a linear pattern in CALC1 (see Fig. 26 & 28 Appendix 9.3). The dacitic samples are mostly represented in the CALC1 one and generally show a tight clustering for most elements. Their Si content is between 65-70%w.t These dacites have generally low zircon content (see Fig. 26 in Appendix 9.3). The more felsic samples fall in the rhyolite field as shown In the TAS and Jensen diagrams (Figs. 7, 9 and 11) and they have SiO_2 at 70-75% wt. they have low Ti and Al contents and their Zr content can have very different values.

CALC1: Some of the rocks of the unit show zircon depletion relative to their otherwise more felsic nature. This is particularly evident with the dacites of the unit. This Zr anomaly is consistent with the basement rocks, some of which have a very similar geochemical trait. CALC1 rocks are very similar in REE patterns being enriched in LREEs and depleted in HREEs.

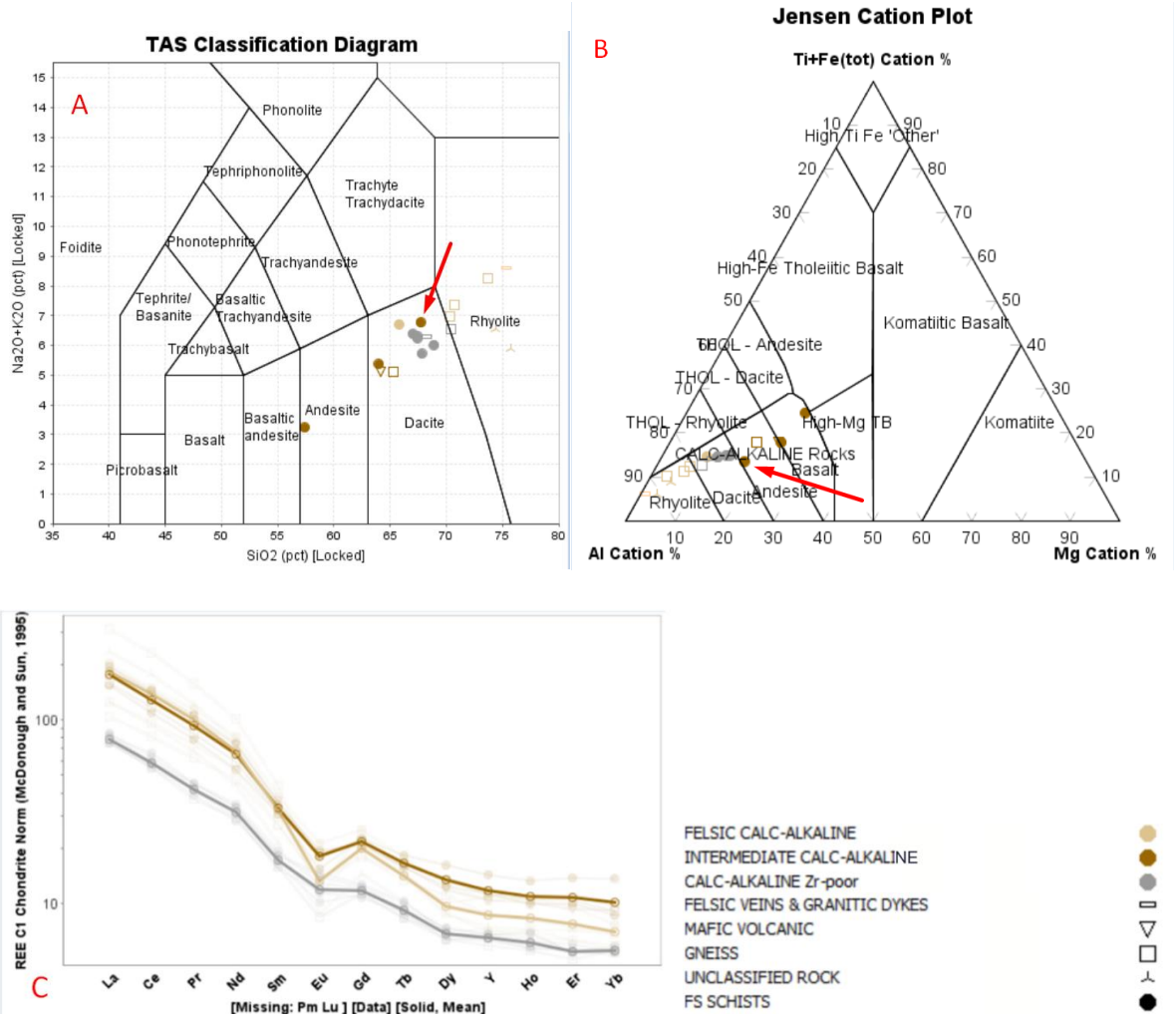

Fig. 8: Geochemistry of the rocks of unit CALC1. A: TAS volcanic diagram B: Geochemical trend of the CALC1 unit, projected in a Jensen diagram. Many of the samples were initially logged as gneiss which makes identification from the Archean bedrock harder. C: REE plot of the CALC1 unit. The red arrow in A and B points to the one sample of the unit appearing on the north part of the TGB in drill hole R336 to pinpoint how the unit reappears there (see Fig. 5). The symbols represent the classification of the samples from the drill core log.

.

KOMBAS1: The rocks begin from near melt komatiitic composition to komatiitic basalts and to High-Mg tholeiites. There are also some intermediate volcanosedimentary interlayers, but these generally don't have many analyses made for the KOMBAS unit. The komatiites have a typical trend that shows general depletion in REEs. There are two distinct groups in terms of REE patterns with a group with distinct enrichment in LREEs including basalts with possible crustal contamination and another group with a flat LREE pattern. This second group includes komatiite lava flows, high-Mg basalts, and tholeiitic basalts.

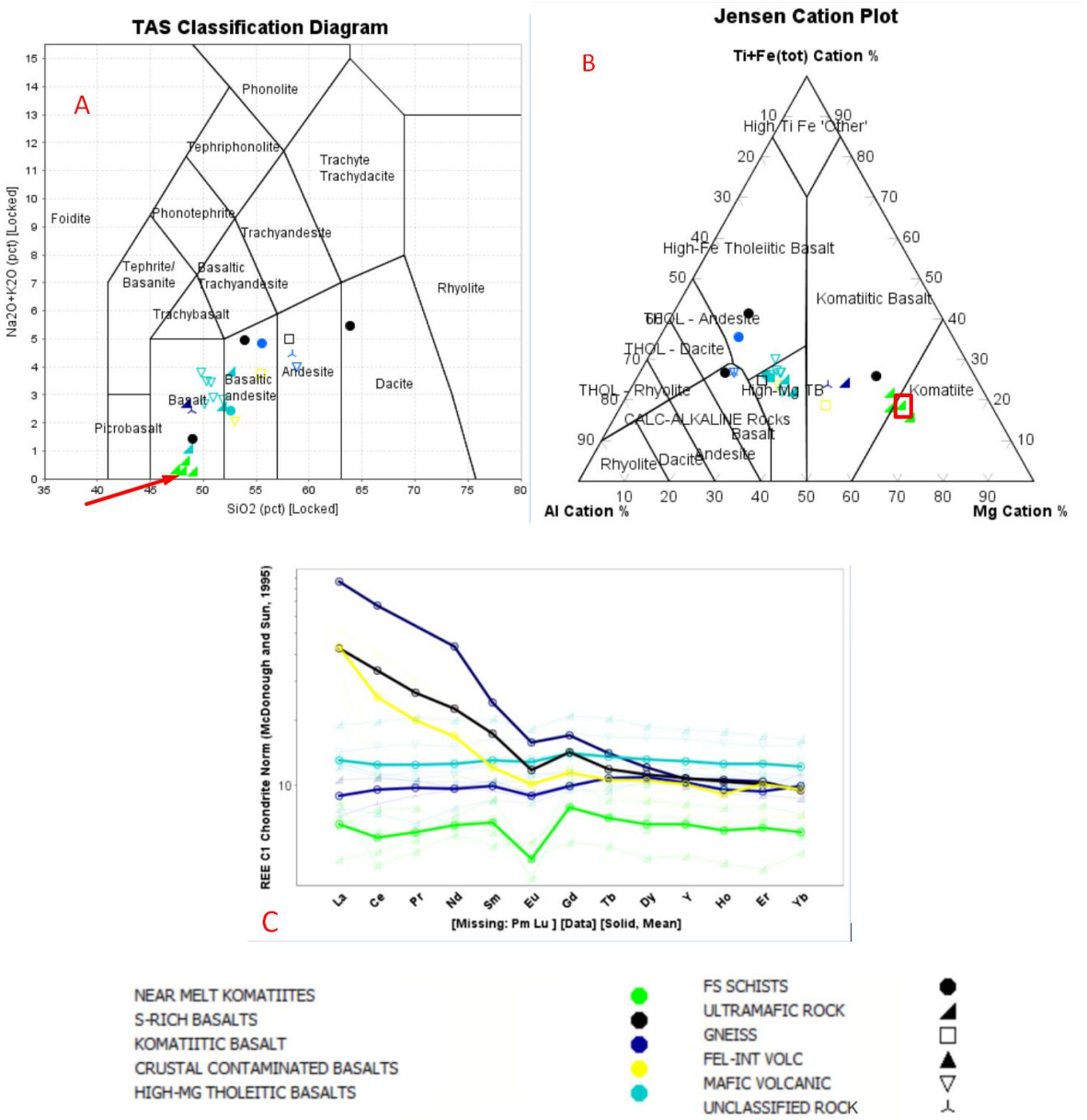

Fig. 9: The rocks of the KOMBAS unit. A: TAS volcanic diagram of the rocks B: The plot of the geochemical trend of the KOMBAS unit in a Jensen diagram. C: the REE trend for the KOMBAS unit. The sample that the arrow points in A and the sample in the red square in B represents the single sample at the North of the drilling profile, found in R336, that also belongs to the KOMBAS (see Fig. 5). The symbols represent the classification of the samples from the drill core log.

CALC2: The rocks show enrichment in LREEs and depletion in HREEs. The more felsic parts also have an enrichment in Gd. Otherwise the unit is very similar with to CALC1.

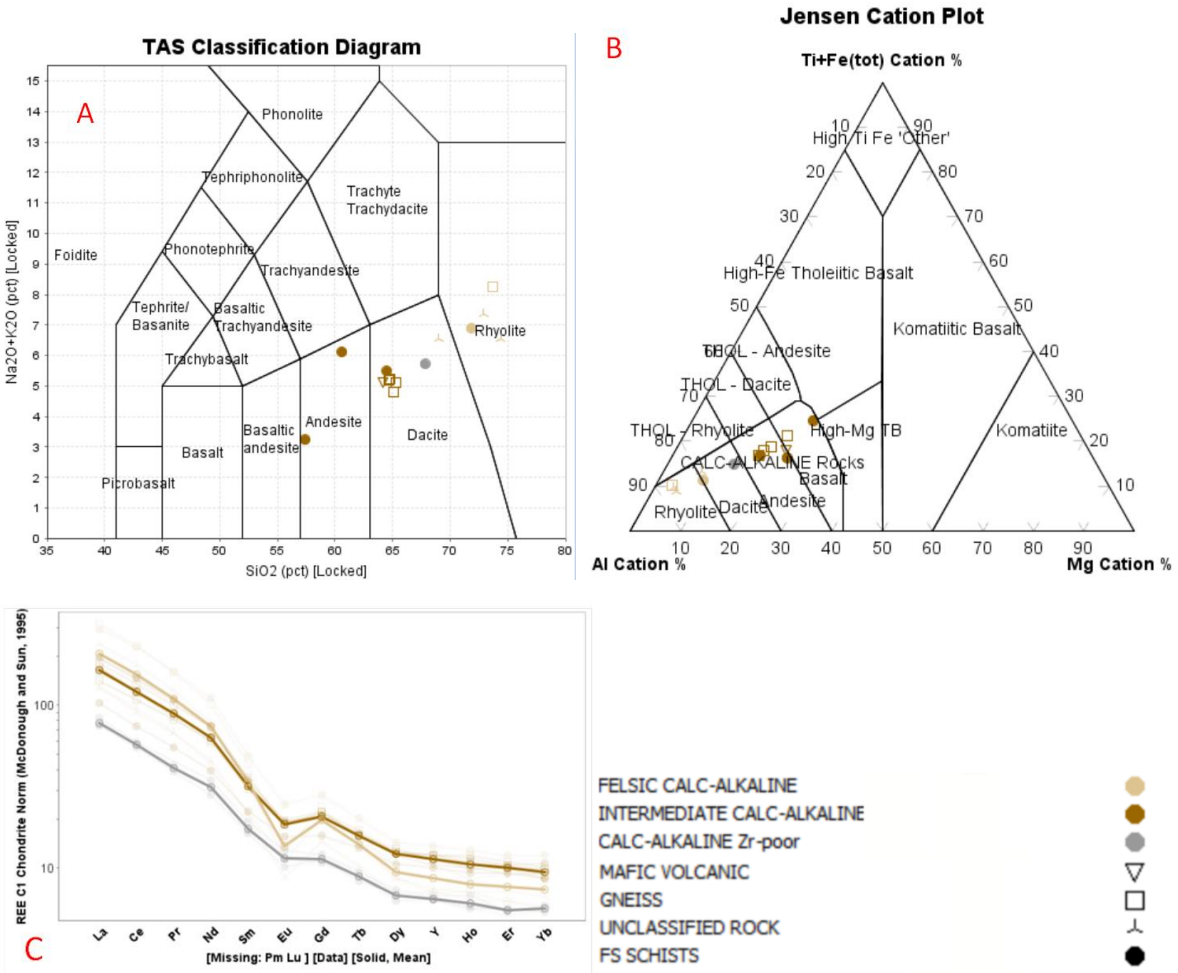

Fig. 10: The rocks of unit CALC2. A: TAS volcanic plot of the rocks B: Geochemical trend of the CALC2 unit shown in a Jensen diagram. There are noticeable similarities between this unit and CALC1 (see Fig.9). C: REE plot of CALC2 unit. The grey circles represent intermediate samples with low Zr levels (see Fig. 28 in appendix 9.3). The symbols represent the classification of the samples from the drill core log.

OLIAD: Only one sample from the OLIAD unit is available from the main drilling profile. Plotted together with olivine cumulates from the KUV drill holes (as previously discussed), the OLIAD rocks plot in the komatiite field as it mostly consists of altered or serpentinized olivine. The unit is generally depleted in all kinds of REEs, with a small negative anomaly on Dy.

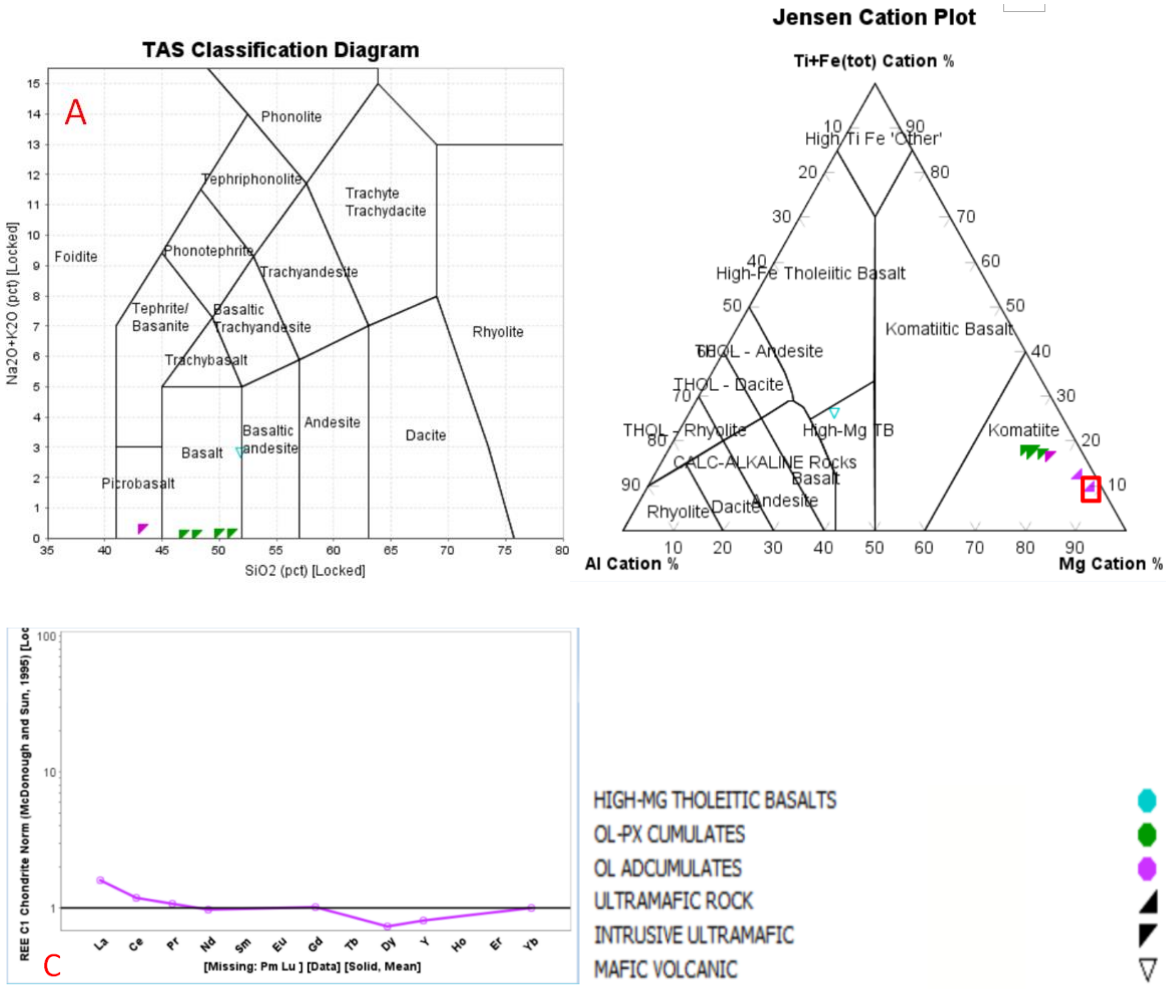

Fig. 11: The rocks of the OLIAD unit. A: TAS volcanic plot B: Geochemical trend of Unit OLIAD shown in a Jensen plot. The sample in the red box represents the singular sample appearing in the drilling profile. C: REE pattern of the OLIAD unit. There was a lack of analyses for the KUV1 and KUV2 drill holes hence the only appearing sample is the one from the drilling profile. The symbols represent the classification of the samples from the drill core log.

CALC3: The unit plots on the fields of dacite and the lower part has a LREE enrichment with a depletion in HREE possibly due to the presence of garnet. The whole-rock analyses apparently did not contain much garnet which is typically enriched in HREE, and thus the HREE depletion in the results. The uppermost part has a flat depleted trend in REEs overall.

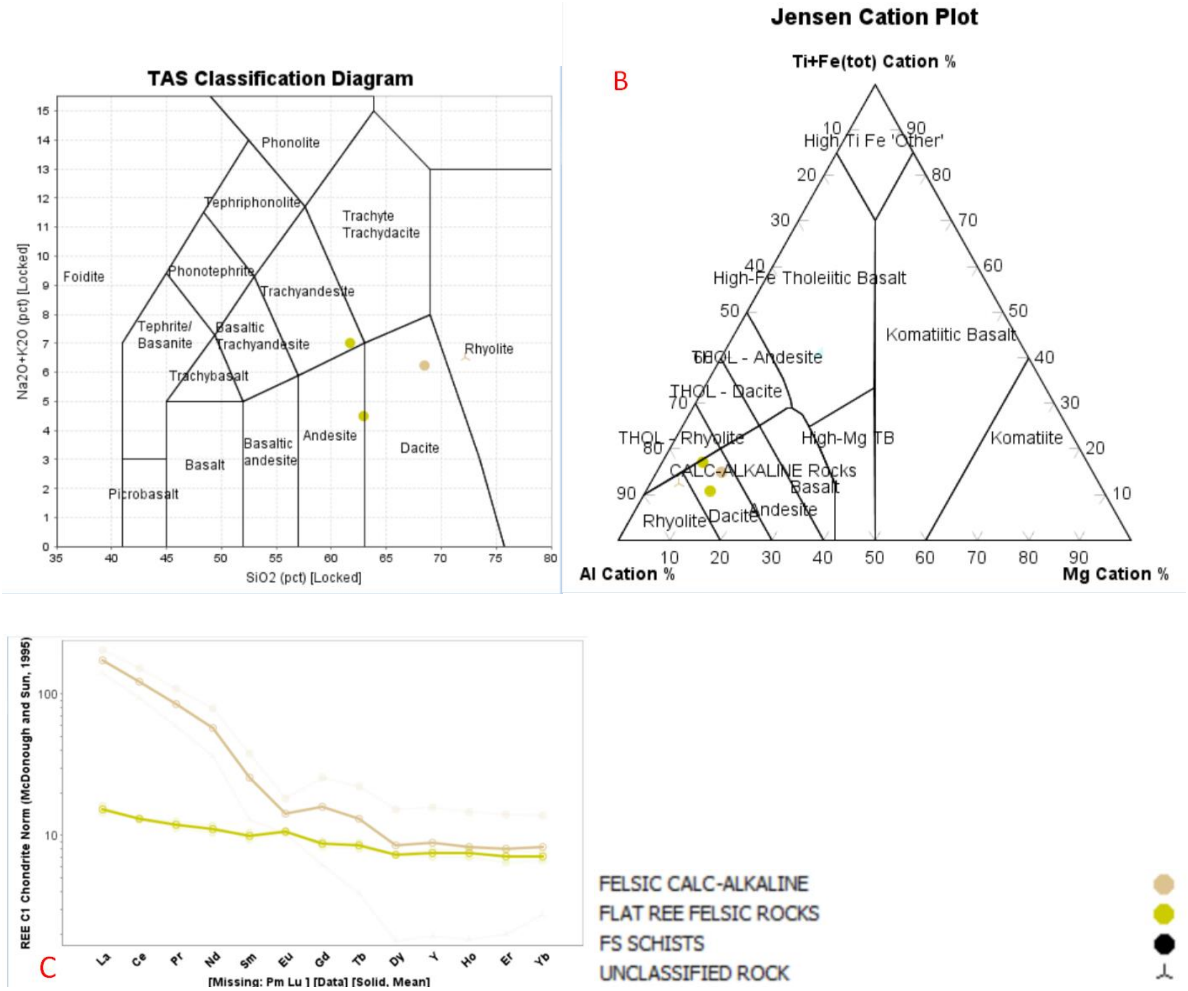

Fig. 12: The rocks of unit CALC3 A: TAS volcanic diagram. B: Geochemical trend of the CALC3 unit shown in a Jensen plot. C: REE pattern of the CALC3 unit. The symbols represent the classification of the samples from the drill core log.

4.1.4. Short overview of drill hole R339

Out of all the different drill holes, R339 is the deepest and it encounters many of the units classified already (Fig. 13). Even though it is not part of the main profile it overlaps with the stratigraphic sequence in the main profile to a certain extent. For these reasons it was used as an ‘‘anchor’’ hole to further understand the general stratigraphy of the TGB.

The contact of the unit with the underlying basement is the same found in the drilling profile, that is, the smooth and gradual transition between the Archean basement complex and the volcanosedimentary sequences. The lower part of the belt begins with volcanosedimentary/volcanic rocks that represent the CALC1 unit. The unit that the drill hole intercepts above CALC1 is a thick sequence of mafic volcanic rocks, similar to the ones belonging to the KOMBAS unit. There is a lack of ultramafic appearances (like the komatiite

flows found in KOMBAS), yet the mafic volcanic sequence is very thick. The rocks encountered in this sequence range from high Mg to komatiitic basalts. The REE trends of this unit also are almost identical to the ones observed at the main profile for the corresponding rock-types (see Figs. and 9 & 14). The upper part of the drill hole is another felsic unit which correlates to the CALC2 unit from the main profile. The REE patterns for these rocks are also almost identical to the ones found in CALC2 (see Figs. 10 and 14)

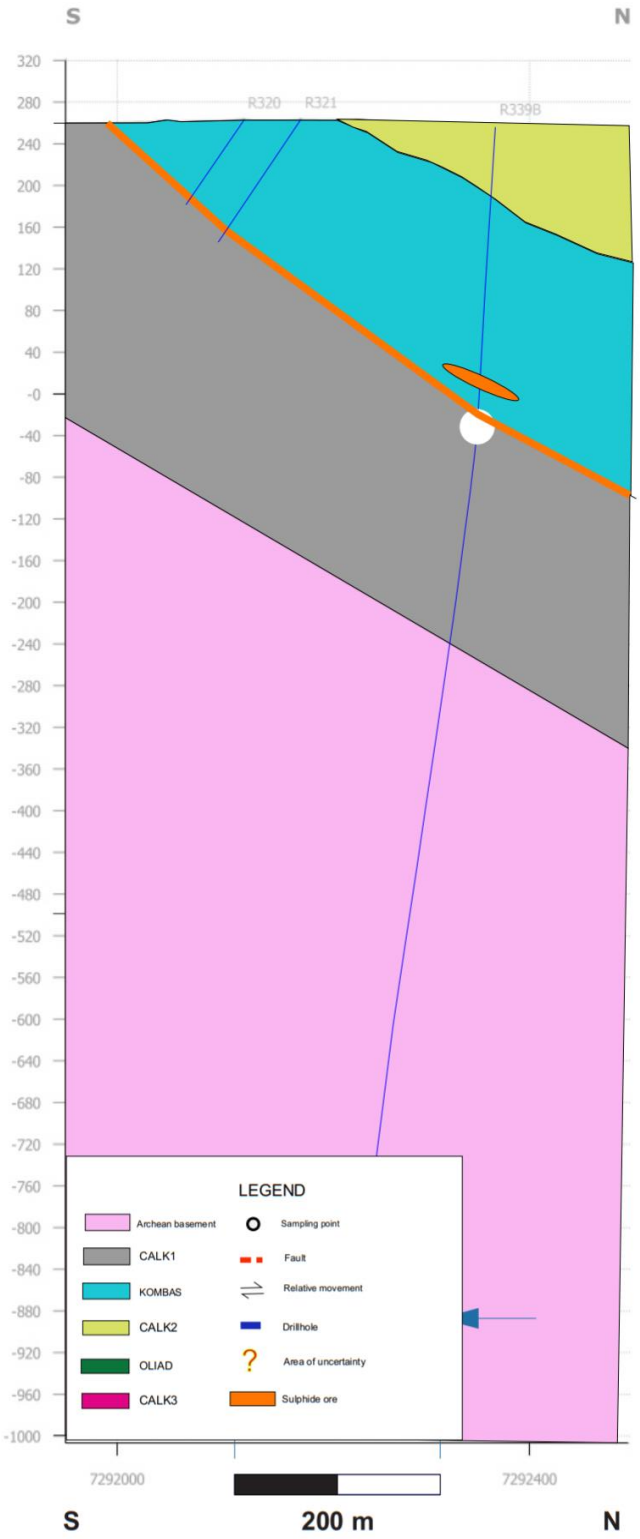

Fig. 13: Cross section of the long R339 drill hole and the nearby R320 and R321. R339 includes many of the units encountered in Takanen (CALC1, KOMBAS and CALC2). At the contact between CALC1 and KOMBAS is a Fe-sulfide ore; it is massive in R339 and turns to a disseminated sulfide schist in the other two drill holes. R339 also encounters a second massive sulfide layer found inside the KOMBAS unit, that does not appear in the other two holes. The sampling point for U-Pb is found right below the sulfide layer at the contact between the CALC1 and KOMBAS unit. The ore found in the KOMBAS unit is approximately 10 m thick.

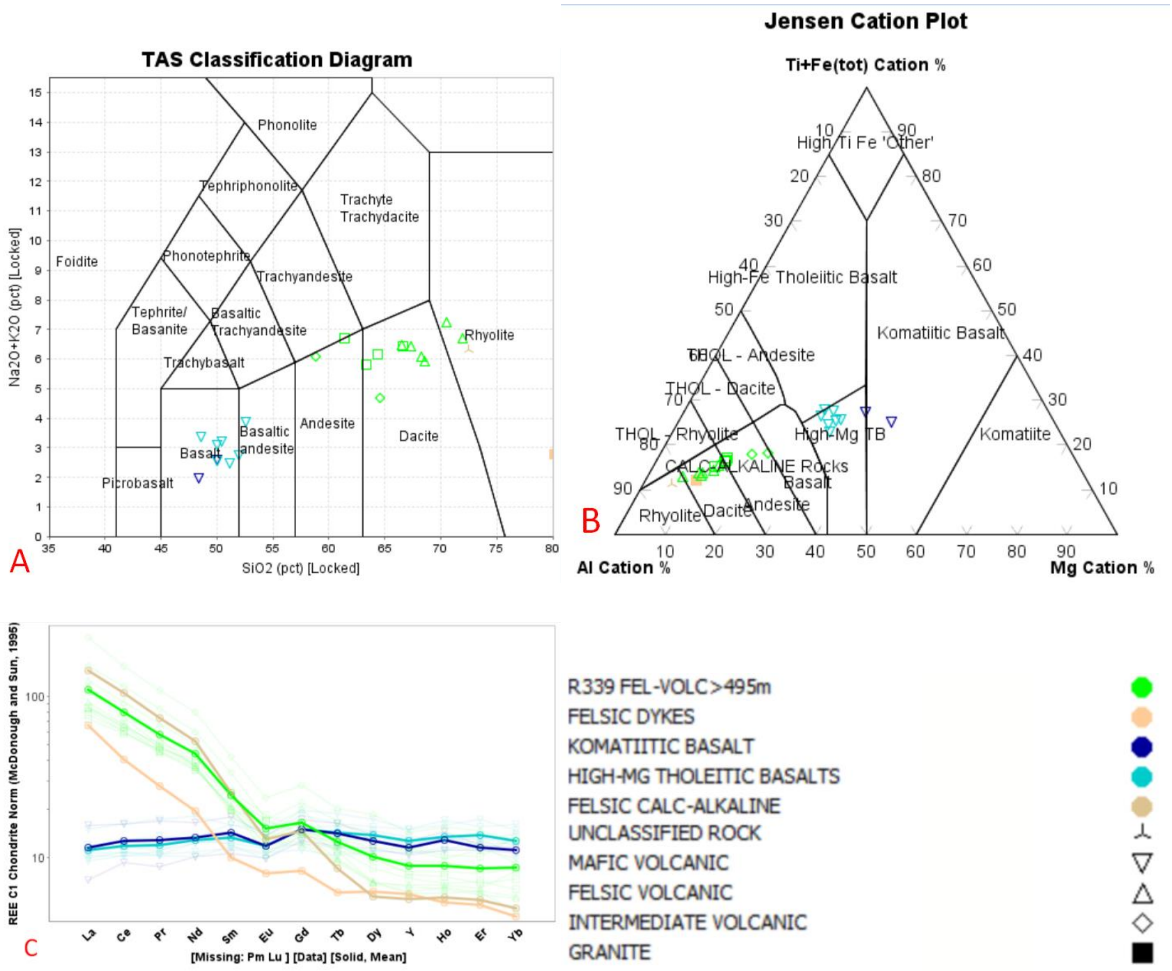

Fig. 14: The rocks of R339. A: TAS volcanic plot. B: The Jensen plots shows the rocks found in the drill hole. The drill hole intercepts the basement and continues with various samples of Archean granite compositions which have been omitted from this diagram for simplicity. C: The REE plot of R339. The green colored samples are the equivalent of the CALC1 unit in the drilling profile. For R339 this unit been grouped this way to signify the lowest and thick volcanic/volcanosedimentary unit in contact with the basement. The symbols represent the classification of the samples from the drill core log.

4.2. U-Pb age dating in zircons from selected samples

The requirements for the dating of the greenstone belt have been discussed in the methods section. With these criteria in mind the 3 candidates with the highest probability of igneous zircon were selected. These are:

a) M452398R318 (R318) taken from a depth of 23.90-26.90 m from the drill hole (Fig. 5) The sample contains 191 ppm of Zr. It is an intermediate to felsic volcanic rock, interlayered between two mafic formations. This ensures that the layer is a part of the volcanic sequence and minimizes the possibility of inherited sedimentary zircons. The sample is foliated with greenstone assemblages of plagioclase, amphibole, biotite and quartz. No primary textures could be observed.

b) M452398R339 (R339) taken from a depth of 277-279 m from the drillhole (Fig. 13). The sample contains 118ppm of Zr. This sample has been metamorphosed into a biotite quartz schist but was initially a volcanic rock (Iljina 2003). Now it consists of plagioclase, quartz, biotite and amphibole. The sample is taken from near the top of a thick felsic volcanic rock sequence deposited on top of a thin mafic volcanic layer. The next layer above the sampled location is a thin Fe-sulphide layer, followed again by mafic volcanic rocks. The sample retains some structures that might be considered primary, namely unoriented coarse porphyric plagioclase with an euhedral habit. This sample was collected deeper from the others and represents the initial stages of volcanic activity in Takanen

c) M452398R332 (R332), from a depth of 61.5-63.6 m from the drill hole (Fig. 5). The sample contains 217 ppm of Zr. The sample comes from an intermediate volcanic rock, that has metamorphosed into an amphibolite, containing mostly biotite and plagioclase. The sampled layer lies on top of an ultramafic unit. No primary structures are maintained in the sample.

Heavy mineral separation was successful in recovering zircons from samples R339 and R332. Sample R318 was originally the highest priority sample but heavy mineral separation failed to present zircons and thus, this sample will not be discussed further.

4.2.1. Petrographic characteristics of the zircons

Regarding sample R339:

The zircon grains from R339 are generally subhedral to euhedral. Some grains show distinct zonation, while in others there is no zonation at all. There are a few elongated zircons which oftentimes show zonation, although there are exceptions to this.

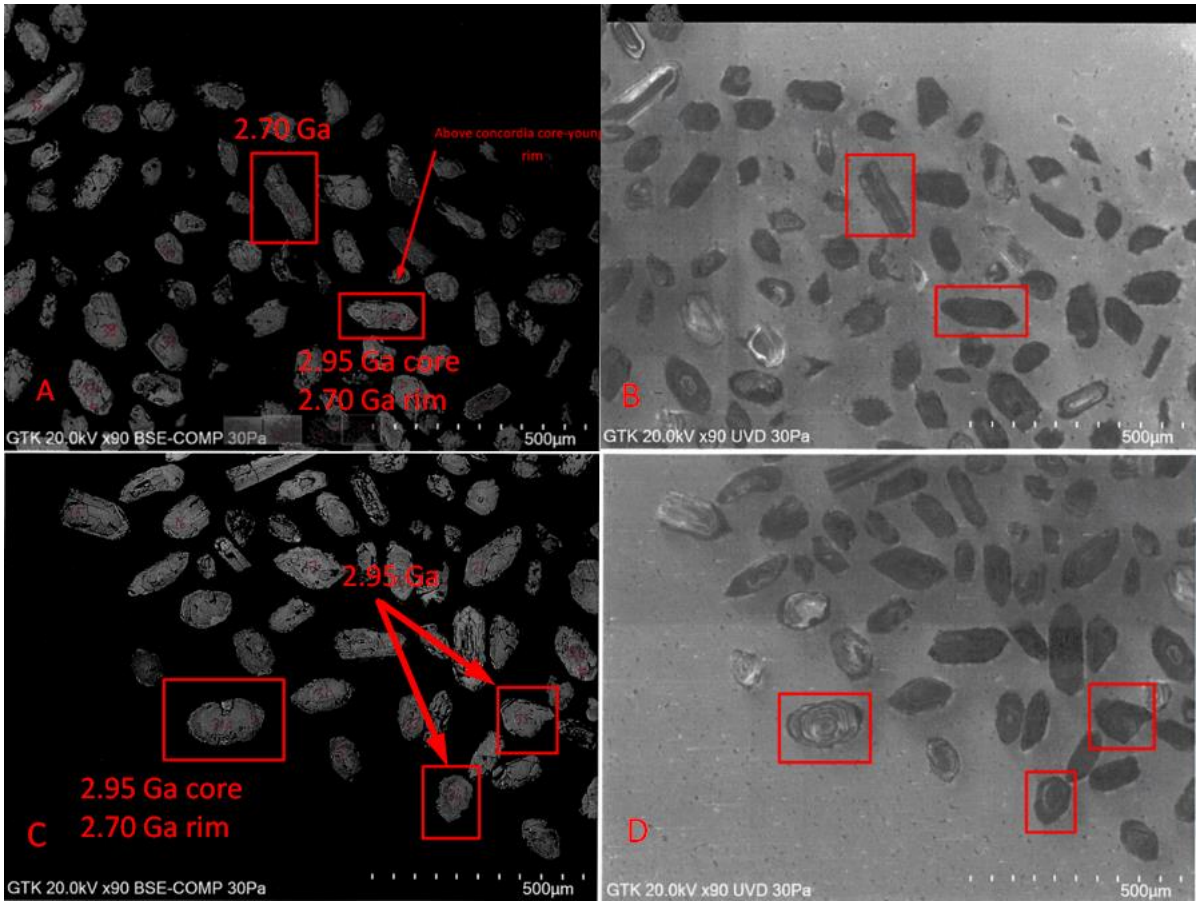

Fig. 15: Zircon crystals from the sampling point of R339. Pictures A and B on top and C and D on the bottom are taken from the same spot. Pictures on the left show imaging of zircon crystals from backscattered electrons. Pictures on the right show imaging of zircon crystals via the use of ultra-variable-pressure detection (UVD). The upper outlined grain in A is a typical elongated zircon crystal often found in R339. These elongated crystals seem to give almost exclusively above Concordia ages. The right outlined crystal pointed with an arrow is an example of a crystal where the core is of older age above Concordia, surrounded by a younger rim. In C, the outlined crystal on the left is heavily zoned. The core consists of the old concordant age that characterizes the group, and the rim is younger. The highlighted crystals pointed with an arrow, on the right are weakly zoned old age concordant zircons.

Regarding the R332 sample:

Samples from R332 range from euhedral to completely anhedral. Some zircons have distinct zonation, while others do not show any (mostly visible in the UVD method pictures) (Fig. 16). Some crystals show a prominent simple two-part zonation with a homogeneous core, surrounded by the outer part, in the form of a thin cluster around it (see Fig. 16 B and D). This structure seems to be pointing to the fact that these zircons may have been affected by a later event.

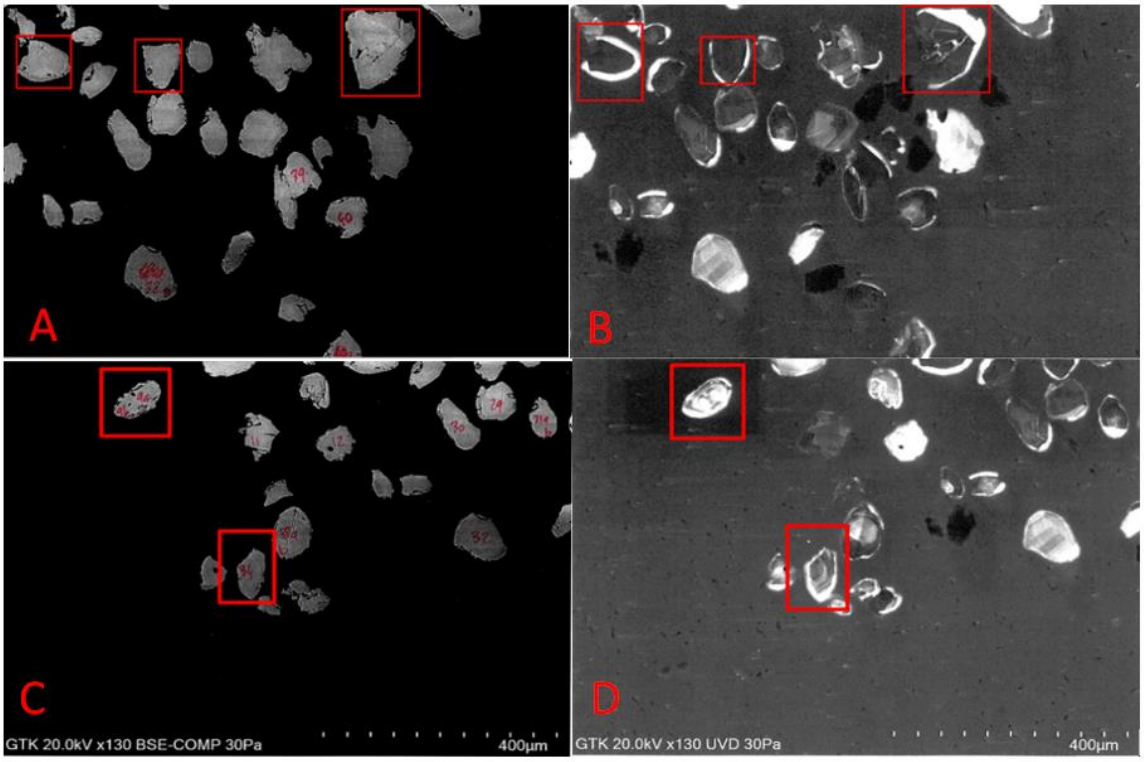

Fig. 16: Examples of the simple two-part zonation from zircons from sample R332. Pictures A and B on top and C and D on the bottom are taken from the same spot. Pictures on the left show imaging of the zircons from backscattered electrons and pictures on the right show imaging of the zircons via the use of ultra-variable-pressure detection (UVD). The heterogeneity of the two parts is visible in both A and B and then C and D respectively. In A and B, the highlighted grains in red show a homogeneous core surrounded by a distinct rim (visible in the UVD method). In C and D, the highlighted grains display the typical zonation observed in crystals from the R332 sample (visible in the UVD method). All the results for this sample give an age of 2.70 Ga.

4.2.2. U-Pb age dating results

Sample R339 revealed 3 different groups of ages that will be presented below. It should be noted that the younger ages usually are found on the outer rims of the zircons. Few exceptions occur where the entire crystal is of a younger age. The cores are almost exclusively older concordant ages or above Concordia ages (see Fig. 17).

Similarly, there are some grains where both the core and the rim are either concordant old ages or above Concordia ages. The crystals that are exclusively above Concordia tend to be elongated and heavily zoned.

The other possibility is that an above Concordia core is surrounded by an old age concordant rim.

One group consists of younger ages at 2726+/-19 Ma. The other two groups represent older ages. The first group, which the majority of the samples belong to, is concordant ages of

2969+/-5.Ma. The other group plots above Concordia, showing intersects at 2957+/-9Ma and 0 Ma (Fig. 17 A and B). This effect is thought to be related to U-fractionation of U/Pb isotopes during laser ablation, resulting from the matrix effects that take place inside the older zircons. In most cases, the results that are above the concordia belong to older cores, or at least the inner parts of zircon crystals. These older cores have undergone metamictization. This causes the matrix of the standard (used for the correction of the isotope ratios) to be different than the actual sample, which results in the above Concordia group, as the matrix effects cause some U/Pb fractionation. Because of these matrix-effects, the age determinations are based on $^{207}Pb/^{206}Pb$ ratios rather than U/Pb ratios.

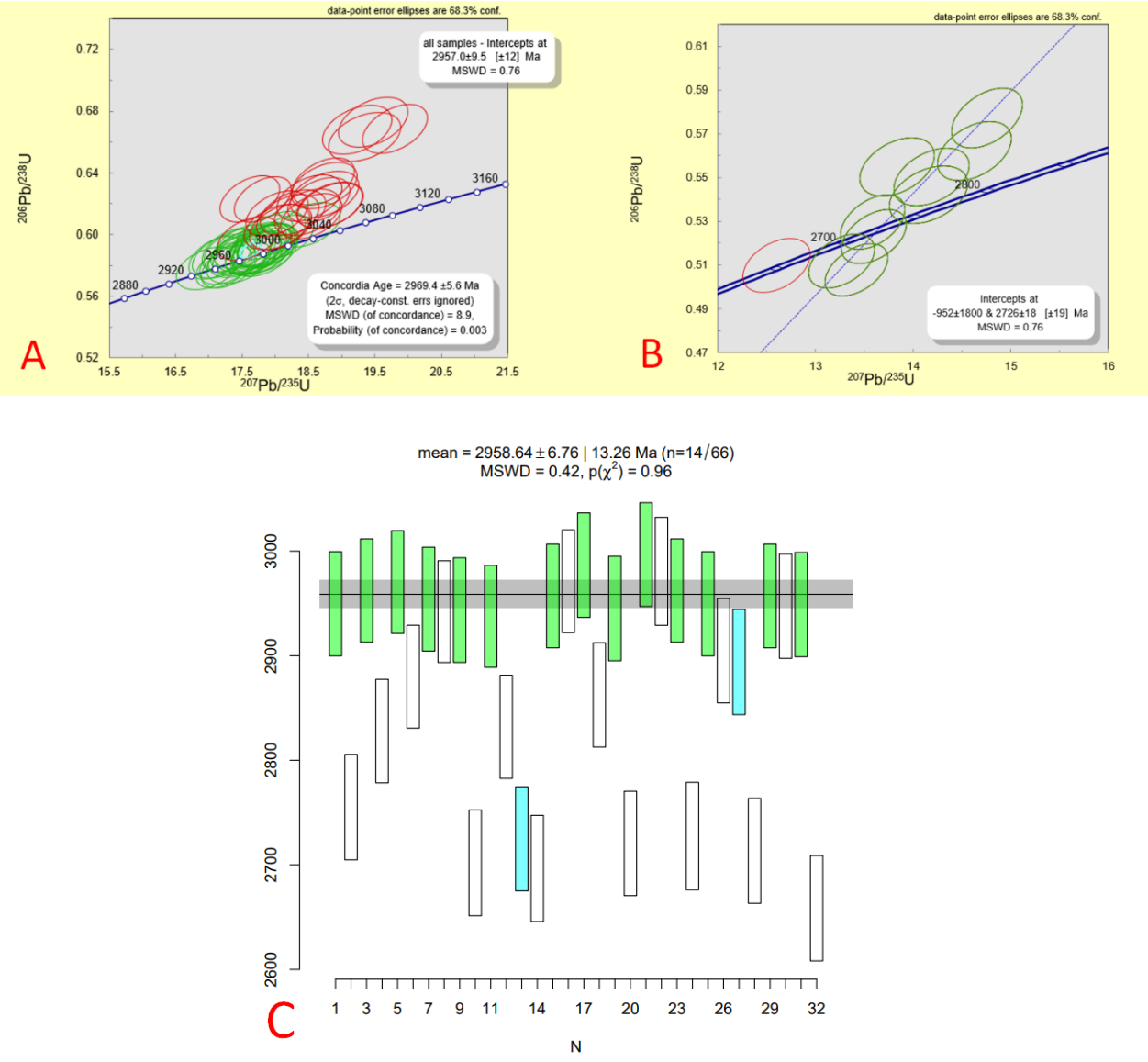

Fig. 17: A: The Concordia plot of the older (2.95Ga) concordant samples in R339; discordant above-concordia laser-ablation spot analyses in red. B: the Concordia plot of the younger (2.7Ga) samples in R339. C: Weighted average 207Pb/206Pb age of the zircon dating for sample R339. The green bars represent grain cores analyzed and the white bars represent grain rims analyzed. Figures A and B made by Yann Lahaye of the GTK, and figure C made by Ville Järvinen.

Sample R332 gives one group of younger concordant ages of 2700+/-4.1Ma (Fig. 18). These younger zircons may originate from a more recent magmatic event, but they can also be of metamorphic origin. The hypothesis of a metamorphic event as a zircon U-Pb system reset mechanism, is based the general structural characteristics of the zircon grains of R332, as was described earlier.

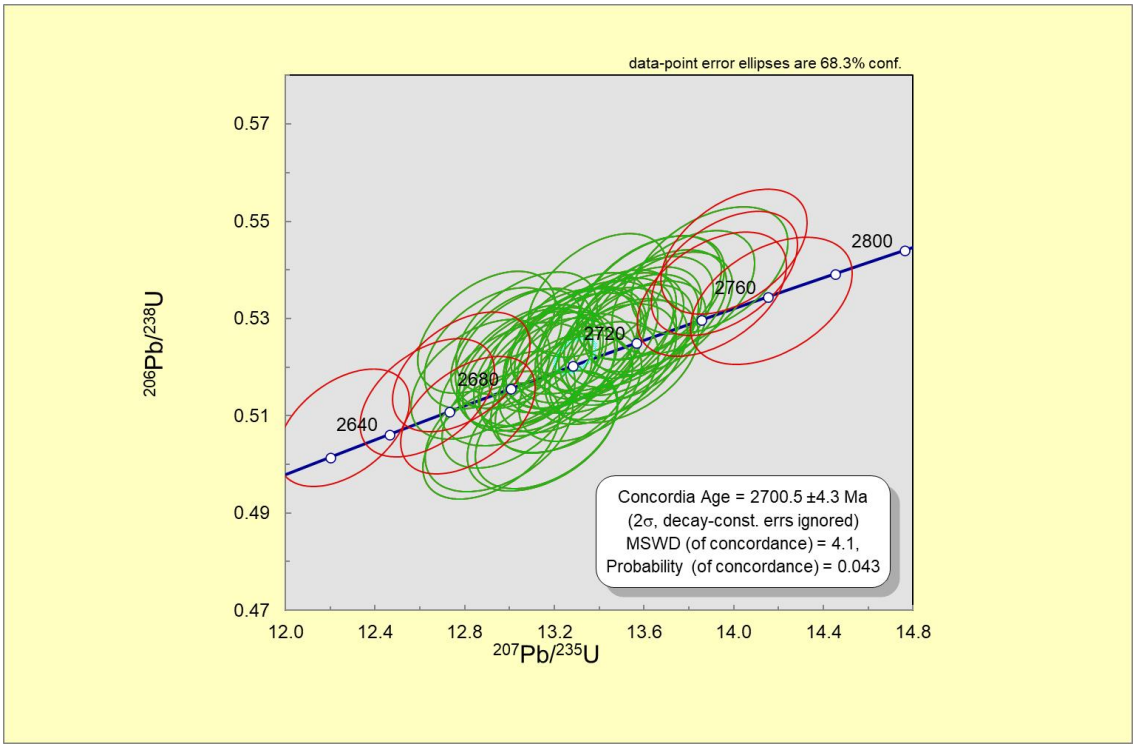

Fig. 18: Concordia diagram for sample R332. Most of the samples are concentrated in the concordia line in a cluster. Figure made by Yann Lahaye of the GTK.

4.3. The Lu-Hf isotope results

The two samples where zircon grains were successfully isolated are the ones from drill holes R339 and R332. Based on initial Hf isotope composition, the two stratigraphic domains of the Takanen greenstone belt show distinctly different origins (Fig. 19). The R332 samples are tightly packed directly on the CHUR line, which means that they have an isotopic fingerprint identical to primitive mantle melts. The data has small deviation with no visible anomalies and their collective 1σ values for both samples range from 0.4-0.6. The samples from R339 show a larger range in Lu-Hf values (statistic description). Samples are projected below the CHUR

line and towards isotope evolution lines consistent with mixing with 3.2 to 3.6 Ga Archean crust. The fact that there is only a small deviation in the data produced from the Lu-Hf method also ensures that there has been little to no Pb leaking during different processes affecting the system and thus the U-Pb method performed for this thesis is more accurate.

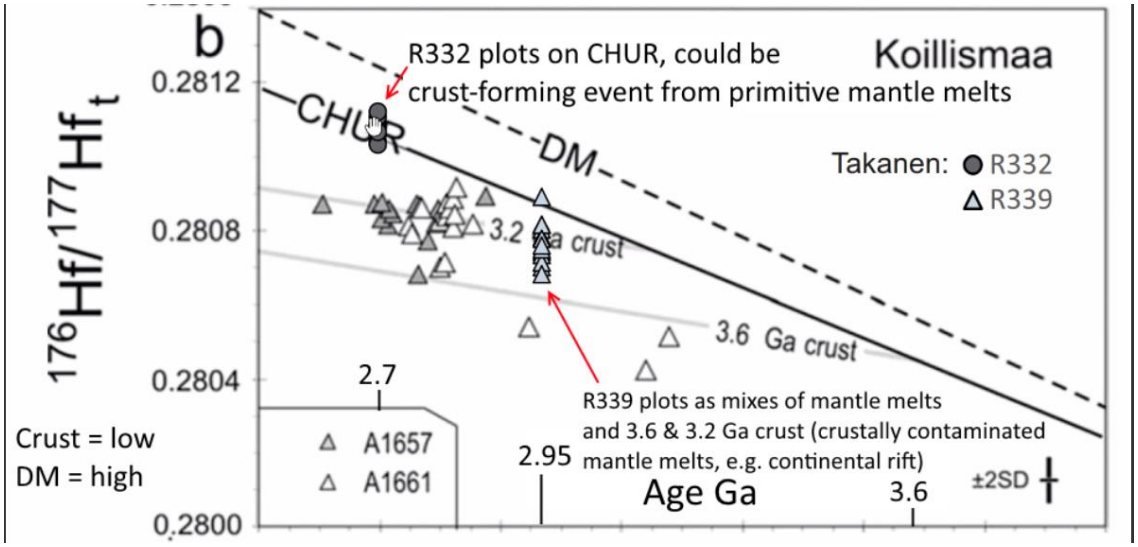

Fig. 19: The geochemical plot of initial $^{176}Hf/^{177}Hf$ isotopic compositions versus the $^{207}Pb/^{206}Pb$ ages from the samples from holes R339 and R332 in Takanen. The data has been plotted on a pre-existing plot made from Lauri et al. (2011), regarding the Koillismaa area samples. The 3.2 and 3.6 Ga curves represent systems with an average $^{176}Lu/^{177}Hf$ ratio of 0.015 originating from CHUR. The CHUR reservoir curve according to Bouvier et al. (2008) as well as the depleted mantle curve after Griffin et al. (2000) are plotted in the diagram. Compiled by O Tapani Rämö of the University of Helsinki.

5. DISCUSSION

5.1. Evaluation of the results and their accuracy

Greenstone belts and, in extent the TGB, are very complex systems with possibly multiple different magmatic events partaking in their formation, and with combined geotectonic situations that drive these events. In addition to these factors the belts have been metamorphosed and deformed through geological time. It is, therefore, important to notice that the geological interpretation of the TGB presented here is very simplified based on the relatively small amount of data produced for this thesis. The cross-section itself depicts a very simple model, given the usual structural complexity of these belts. There were no whole-rock geochemical or thin-section data available for this work from drill holes R334 and R335 (Figs. 4 & 5). These two drill holes are in the middle of the main drilling profile, and this creates a

large area of uncertainty in the cross-section. In addition, having only 2 samples for age dating is enough to constrain the general age of the belt but not enough to have a full image of the temporal evolution of the TGB.

To create a more accurate depiction of the real version of the system more detailed age dating of different layers would be necessary. This would make classification, unit grouping and stratigraphic modelling more accurate, as there would be better correlation between the various parts of the TGB (and neighbouring greenstone belts). Despite these limitations, the belt can still be understood at a fundamental level.

Another thing to be noted is that the mafic layer found only in R333 (see paragraph 4.1.1) is considered to be a part of the OLIAD unit for the purpose of this thesis, based on the fact that stratigraphically it is placed exactly under the CALC3 unit. Further evidence to support this is in the KUV3 drill hole, which includes some similar tholeiitic basalts amongst the thick layers of olivine adcumulates. However, this inference is uncertain, and the contact between this rock and the layers above it could be of tectonic origin.

5.2. Correlation of the TGB to the SKT system based on age and stratigraphy

The data collected from this research strongly suggest that the TGB is the northern continuation of the SKT greenstone belt system. The oldest age of the TGB (2.95 Ga) seems to correspond to the oldest age found at the Suomussalmi greenstone belt (2.94Ga) (Lehtonen et al. 2016b). Because the SKT is known to become younger towards the south (Lehtonen 2016,), this could mean that the TGB is the oldest part of the bigger SKT system, and that the formation of the combined system began from the north with Takanen and gradually developed towards the south with the Kuhmo and Tipasjärvi belts being the youngest.

More importantly there seems to be overlap between the TGB stratigraphy and the rock groups found in Suomussalmi. The key unit in this comparison is CALC1 which shows lots of similarities with the Luoma group described from the Suomussalmi belt (Piirainen 1998). The Luoma group represents the oldest rocks in this belt with a reported age of 2.94 Ga (Huhma et al. 2012, Lehtonen et al. 2016b), which corresponds very well to the 2.95 Ga age of CALC1 from sample R339 (see Fig. 20)

Furthermore, the Luoma group consists of felsic-intermediate-mafic tuff and tuffitic rocks, banded amphibolite and quartz porphyry dykes (Papunen et al. 2009, Lehtonen et al. 2016b). The description of these rocks overlaps almost perfectly with the felsic-intermediate-mafic volcanosedimentary rocks, often penetrated by quartz veins, that are described from the CALC1 unit in Takanen.

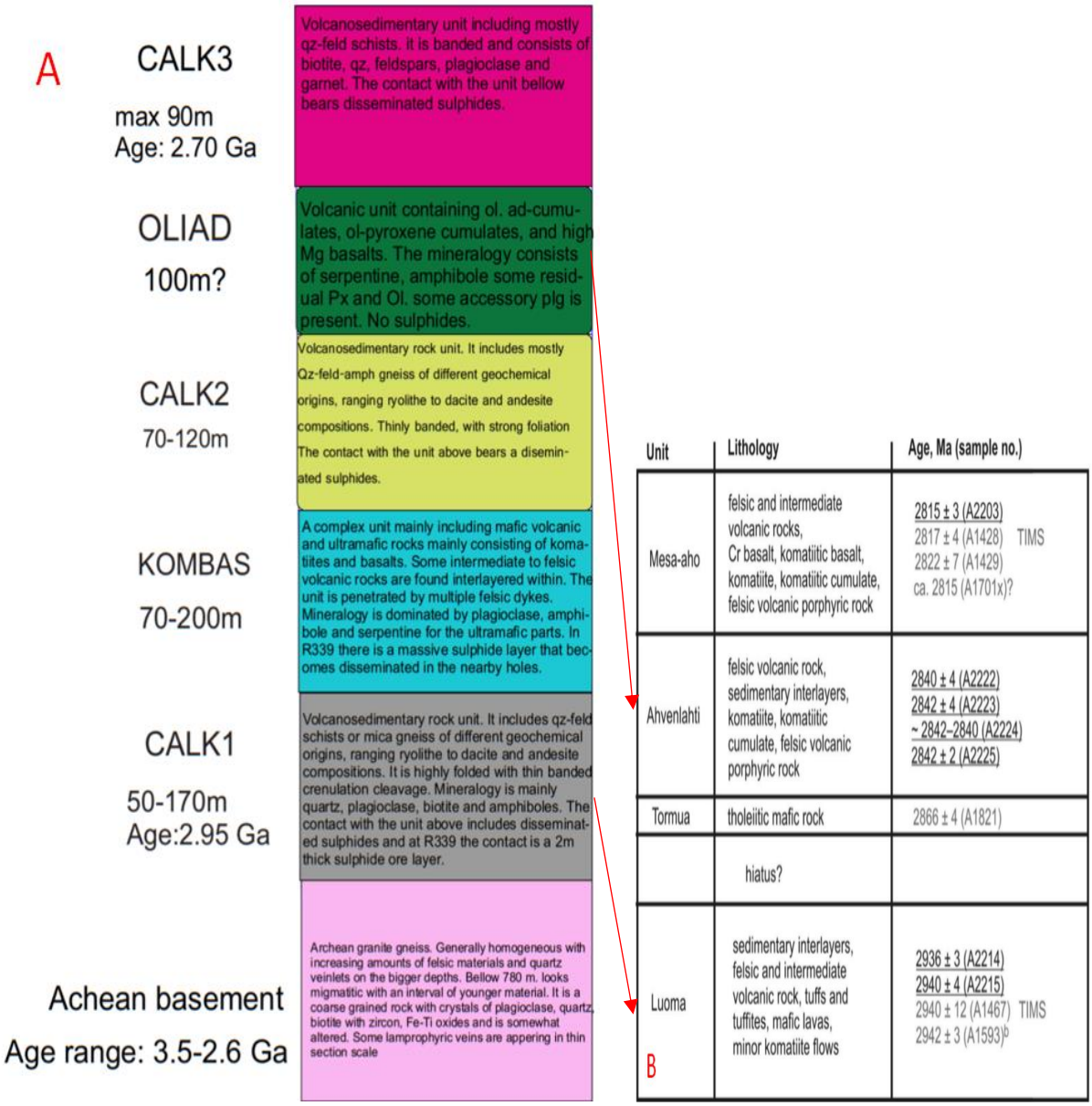

Figure 20: A: Simplified stratigraphic column, showing the 5 rock groups encountered in Takanen, as well as the minimum and maximum thickness of the units. B: Stratigraphic column made by Lehtonen (2016b) showing the rock units found in the Suomussalmi greenstone belt. The red arrows starting from Fig. 20 A, show the possible correspondence between the units found in Takanen and the ones found in Suomussalmi. These are namely the correlations between the CALC1 unit and the Luoma group and the OLIAD unit with the Ahvenlahti group. Fig. 20 A was made by Karampelas (2022) and Fig. 20 B by Lehtonen et al. (2016b).

It should be mentioned that the Luoma group also contains some small komatiite flows and mafic lavas (Lehtonen et al. 2016b). This could suggest that the KOMBAS unit in Takanen

could be part of the Luoma group. This points to a model of bimodal volcanism where injections of magma from different origins, reach the surface. Although there is sufficient evidence to support a bimodal volcanism model, for the purpose of this thesis the CALC1 unit and the KOMBAS unit will be treated as separate entities based strictly on their geochemistry. Regardless, the KOMBAS unit itself includes some isolated intermediate volcanosedimentary interlayers that enhance the idea of a bimodal volcanism system to a certain extend.

Another possible correlation is that the OLIAD unit from Takanen to the ultramafic rocks found in the bimodal unit of Ahvenlahti in the Suomussalmi belt (Lehtonen et al. 2016b). This is a hypothesis based only on the stratigraphic similarities between the ultramafic rocks found in both units (Fig. 20). The ultramafic Kellojärvi cumulate complex contains komatiitic basalts and olivine cumulates similar to the ones found in OLIAD especially at the KUV1 and KUV3 holes. This is not decisive evidence, but it could be tested. Based on the age dating of the felsic interlayers found between the ultramafic rocks in Ahvenlahti the age of these komatiite flows is 2.84Ga (Lehtonen et al. 2016b). If a later study in Takanen dates the OLIAD unit specifically and finds a similar age, this could mean that these units are related.

Finally, the age data from the youngest zircons sampled from R332 shows an age of 2.7Ga which is almost the same with the Ronkaperä unit in the Kuhmo greenstone belt. This unit represents the youngest formation in Kuhmo, and it consists of quartz-rich sandstone, quartzite, conglomerate, mica gneiss and schist, and volcanosedimentary rocks (Lehtonen et al. 2016a). However, this age comparison and the existence of felsic volcanosedimentary rocks is not enough evidence to convincingly correlate the two units. It should be noticed that both units are also found on top of ultramafic sequences so the idea of them being somehow related can still be entertained.

The TGB, despite its small size compared to the rest of the SKT, seems to include multiple units found in the bigger belts, concentrated in a small area. Further research focusing on the individual layers of the TGB could uncover its correlation to the SKT system in a more detailed level.

5.3. Emplacement of the TGB into the Archean basement

A) Based on geological contacts and whole-rock geochemistry:

The explanation of the geological positioning of the TGB on its current location above the Archean basement is rather difficult to be understood. According to the drill core and

geochemical data, there is a very smooth and gradual transition from the granitic bedrock to the volcanic/volcanosedimentary rocks of the lower CALC1 unit. This is especially evident in the south part of the drilling profile and the lowermost part of R339 (see Iljina 2003). This transition suggest that the belt is autochthonous, and its formation began right on top of the Archean felsic plutonic rocks (Lehtonen et al. 2016b and references therein). In addition, CALC1 has very similar geochemical trends with the Archean basement directly beneath them, further suggesting some sort of genetic correlation with the basement (see Figs. 31 & 32 in Appendix 9.3)

B) Based on previously reported zircon U-Pb ages:

On the other hand, the age dating from this study compared to ages known for the Archean basement complex of the area suggests a different possibility. The lower part of the Greenstone belt dated at 2.95 Ga is generally older than the TTGs which are the main Archean basement rock assemblages found in the Taivalkoski area. The Kuusamo area shows ages of 2.80-2.70 Ga for the TTGs at the nearby Kuhmo granitoid complex (Hölttä et al. 2012), (see Fig. 2). Lack of older basement rocks would effectively mean that the TGB must be allochthonous and was emplaced on its current location after it was formed by some major structure. This contradicting evidence makes understanding the origin of the belt somewhat difficult.

C) Based on newer whole-rock Sm-Nd and U-Pb data:

There has been more dating done, that found ages older than the ones mentioned before. These areas were found in tonalites and trondhjemites in the areas of Suomussalmi and Taivalkoski. The oldest ages found were 2.98Ga in a Suomussalmi trondhjemite and 2.80-2.87 Ga in a tonalite in Taivalkoski amongst others (Hölttä et al. 2021). More importantly, many of these 2.80-2.87 Ga granitoids contained some inherited grains with ages of 2.9-3.2 Ga. This research suggests that there was older Archean crust and that the newer ages reported on the paragraph above result from reworking of this older crust. This indicates that the area surrounding the TGB may contain parts of this older (Mesoarchean) crust and therefore it is possible that the Takanen belt is autochthonous. It is possible that this situation would resolve if there was age dating data produced from the basement gneisses in the R339 drill core, directly below the CALC1 unit in the TGB. If the basement on this area happens to be of the same age with the belt or older, that would decisively suggest that the belt is found today near or at its place of initial formation.

The suggestion that has already been made by Lehtonen et al. (2016b) referring to the Suomussalmi greenstone belt, is that the lower part of the belt is stratigraphically layered upon the Archean basement, while the rest of the belt was juxtaposed upon it through a major unconformity or shear zone. This hypothesis would extend to the CALC1 from Takanen since the two represent the same paleogeographic environment. (Engel and Dietz 1989, Sorjonen-Ward and Luukkonen 2005).

With that in mind, a model of continental rifting can be suggested as the reason for the formation of at least the CALC1 unit, as it is the unit from Takanen that corresponds to the Luoma group. As continental rifting is responsible for bimodal volcanism it is possible that the KOMBAS unit above CALC1 is also a result of this process. The smooth transition from Archean granite to the first volcanosedimentary rocks could be a result of an older continental crust showing the first stages of rifting. Furthermore, the Lu-Hf isotope results for the sample from drill hole R339 and in extension the CALC1 unit projection, suggests that rifting is the most possible solution for the formation of the lower parts of the strata in the TGB (see Fig. 19).

There is some ambiguity regarding the Lu-Hf results from R332. The plot shown in Fig. 19 suggests that they might have come from a primitive mantle melt as they plot exactly on the CHUR curve. A further clue suggesting magmatic origin is that the R332 samples are all concordant. A slight discordance in the results would be evidence supportive of a metamorphic event that could have somewhat reset the system. On the other hand, the origin of these younger zircons is still not certain, and some might be originating from some metamorphic event that took place later. This idea is also supported by the image of the outer rims of old zircons from R339 that show these 2.7Ga ages in the U-Pb method (Fig. 15). In any case, the Lu-Hf method is a good tool for determining the reliability of a possible U-Pb reset in detrital zircons (Pokki et al. 2013). The combination of the Lu-Hf isotopic composition data with the available U-Pb results regarding the age of the TGB, produces a reliable case. Therefore, the most possible scenario is that the newer age of the zircons is due to a later partial melting event at around 2.7 Ga.

The lack of U-Pb and Sm-Nd isotope data for most of the main bulk of the TGB makes it hard to tie the rest of the belt to a specific geodynamic environment. The KOMBAS basalts do not show any of the typical LREE depleted pattern expected in MORBs so the possibility of them being MORB basalts is rejected. This suggests that there has not been a full rifting of

the area to the point of creating a new micro-ocean. Some of the basaltic trends are more similar to flood basalts. All in all, the highest probability is that the younger units of the TGB were formed from a combination of events that could include continental rifting (as shown by the LREE enriched rocks of the CALC units, suggesting crustal contamination), or some sort of continental plate-oceanic lithosphere interaction, similar to the case of the SKT complex (Lehtonen 2016, Lehtonen et al. 2016b).

At this point the major structure underneath the TGB must be mentioned. The large gravimetric and magnetic geophysical anomaly with a general orientation E-W is found directly below Takanen (Fig. 3). A new drill hole has been made that reached the depth that has intercepted the mafic dyke responsible for the anomaly. (Karinen et al. 2021). It has been assumed that the mafic-ultramafic dyke has acted as a feeder for later intrusions and is directly related to the 2.44 Ga Paleoproterozoic Koillismaa and Näränkävaara intrusions (Järvinen 2022). Although there are no dating results for the rocks found in the dyke, primitive mantle sourced rocks of both Archean and Paleoproterozoic age are found along it (Karinen et al. 2021, this study). This fact suggests that the structure has acted as a magma pathway to the surface for a long period of time and was perhaps active both in the Archean and the Paleoproterozoic. Certainly, the direct geographical overlapping of Takanen right on top of the anomaly caused by the dyke, means that there is a big crustal structure that allowed the primitive mantle rocks to reach the surface resulting in both the TGB Archean rocks and the nearby Paleoproterozoic intrusions in Näränkävaara. So far, there is no real evidence that the dyke itself is genetically related to Takanen but the detailed analysis of the new drill hole in the next year could produce results that say otherwise.

5.4. Possibility of an orthomagmatic Ni potential

The exploitability of orthomagmatic Ni deposits is usually limited by the availability and volume of the mafic-ultramafic rocks in a given area. In most cases, the footprint of such deposits is usually small when compared to the size of other types of deposits e.g., porphyry gold deposits (Barnes et al. 2013). The TGB is significantly smaller than most of the main greenstone belts that are known for their Ni deposits, and thus the possibility of Takanen having an exploitable orthomagmatic nickel deposit is rather small. Still, it is worth discussing this case, as the area can still have an adequate deposit somewhere nearby but not yet discovered.

In the TGB, the most sulphides are located at or near the contacts between mafic and felsic units and there is one local massive sulphide layer in the KOMBAS unit at the area of R339

(see Figs. 5 and 13). Most of the sulphides are disseminated with a few 1-2m thick layers in some contacts. Some other sulphide layers have been found in nearby drill cores that have not been mentioned in this thesis as they are not so strictly related to Takanen.

Given the geology of the TGB there are two main mechanisms that could trigger the formation of a Ni deposit. The key here are the sulphide layers found interlayered between the ultramafic/mafic volcanics and the calc-alkaline volcanic/volcanosedimentary rocks. This sulphide layers consist mostly of pyrrhotite and some pyrite and do not include any pentlandite or other Ni sulphides. However, they may have played a part in the formation of Ni deposits elsewhere in the Takanen komatiite flows. The possibilities are:

A) The sulphide layers pre-date some of the ultramafic lava flows. If this is the case, then the komatiite flows may have interacted with them and absorbed the S that is found in large quantities in them. The new S rich komatiite flow could have then gravitationally deposited Ni-sulphides at a point where the lava is cooled enough (Lesher and Groves 1986).

B) The sulphide layers were deposited after the lava flows. This would effectively mean that for a nickel deposit to exist, the komatiite flows would have to interact with the basement rocks in order to obtain the necessary sulphur

The relationship between the sulphide layers and the komatiite flows is not perfectly clear. However, if the stratigraphy of the TGB is as classified in this thesis, then the OLIAD unit that is found above the sulphide layers is younger than them and thus, there is a considerable chance that the ultramafic flows have somehow interacted with the sulphides.

A good test for the fertility of the komatiites is the Ni vs MgO diagram in komatiites. The best signature is the presence of both Ni-rich and Ni-poor rocks, which indicates that nickel has been stripped away from the lava flow with processes different than simple fractional crystallization, one of which is with the deposition of a Ni-rich sulphide layer. If only one of these conditions is met, this means that there has been no sulphide saturation at all (lack of depletion), or that the rocks have been completely stripped of nickel in a previous mineralization event (if all the rocks are depleted in Ni).

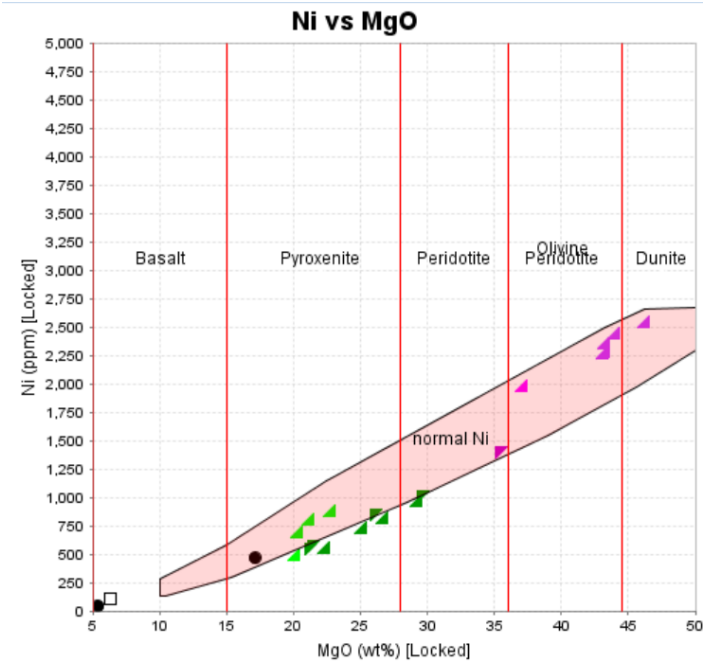

Fig. 21: The MgO vs Ni diagram for the ultramafic rocks in the TGB modelled after Brand (2004). This plot includes the ultramafic rocks intercepted from the drilling profile, as well as the KUV1, R324 and R325 holes which are found nearby and are located close to each other. The original diagram refers to cumulate assemblages, which corresponds well with the olivine and olivine-pyroxene cumulates found generally in the OLIAD unit (pink and purple colors). The ranges for liquid compositions such as the komatiite flows found in the KOMBAS unit (light and dark green colors) slightly differ and range from 18-28% MgO content for thin lava flows. However, since the samples generally project within these limits in this figure, it is used as a composite diagram for all ultramafic rocks of the TGB.

For the case of Takanen what is evident is that the ultramafic rocks are generally plotted in the field of normal Ni content, while there seems to be a slight depletion in the Olivine-Pyroxene cumulates found mostly in hole KUV1. These data show that the possibility of a Ni potential although rather small can maybe still researched further with a more detailed analyses on the OLIAD unit that contains these cumulates.

6. CONCLUSIONS

The Takanen greenstone belt is an Archean greenstone belt that presents a variety of rocks raging all the way from komatiitic olivine adcumulates to felsic calc-alkaline volcanic and volcanosedimentary rocks. The rocks of the belt are classified mainly based on their geochemical traits and their age based on U-Pb data from zircons into 5 units. Three calc-alkaline groups (namely CALC1, CALC2, and CALC3) and 2 mafic/ultramafic volcanic units (namely KOMBAS and OLIAD) that are layered in between these calc-alkaline groups. The age dating of the TGB produced 2 ages one at 2.95Ga for the lower part of the stratigraphy

taken from the CALC1 group and a younger 2.7 Ga for the upper part of the strata taken from CALC3.

Takanen appears as the northernmost part of the previously well studied SKT greenstone belt system. This is evident by the stratigraphic similarities between the units classified in Takanen and the Suomussalmi greenstone belt. The lower volcanic/volcanosedimentary rocks dated at 2.95 Ga are in agreement with the lower pieces of the strata from Suomussalmi, in terms of petrography, geological positioning over the Archean basement, geochemistry and age (2.94Ga). There is also the possibility that more units of the TGB are connected to the SKT system, but this remains to be proven.

The formation of the belt can be subject of various geotectonic models. According to the data collected from this thesis, the lowest part of the stratigraphic column is related to the initial stages of continental rifting and the rest of the belt, was most likely created by a combination of events, namely continental rifting, in addition to one or more interactions of Archean continental crust with oceanic lithosphere. Further data needs to be collected and the TGB needs to be compared to the SKT system in greater detail to decide on a definitive model. A collective study of these combined could be the key to explaining the formation of the general system and possibly, further understanding the creation mechanisms for greenstone belts overall. The TGB is also emplaced directly above the large-scale gravitational anomaly of the Koillismaa area, which indicates that there is a significantly large crustal structure underneath it that served as magma pathway for both the Archean supracrustal rocks of Takanen and the later Proterozoic intrusions nearby.

The TGB is a relatively small area for an orthomagmatic Ni deposit in terms of economic geology. The TGB contains some possible mechanisms for the creation of a Ni deposit, through the interaction of the komatiite flows with older sulphide layers found in the strata. However, the data from this thesis are not very promising in regard to nickel exploration, as there has been no Ni-rich layer discovered. The geochemistry does suggest the existence of a small Ni depletion in the ultramafic rocks of the OLIAD unit which could be explained by the stripping of nickel through a gravitational separation during a komatiite flow. Based only on this clue however, the possibility of a considerable hidden nickel deposit near the research area is rather small. Regardless, possible combined research including the SKT system and especially the Suomussalmi part, could show some positive evidence for nickel exploration in the future.

7. ACKNOWLEDGEMENTS

First and foremost, I would like to thank Ville Järvinen for the supervision and guidance of this project. Ville has helped me immensely with both the technical and purely academic questions that I had throughout this research. I would also like to thank my co-supervisors Ö. Tapani Rämö and Tapio Halkoaho for their most valuable comments and revision of my thesis. All three have been like mentors to me throughout this research.

I am grateful to the University of Helsinki for supporting and funding this project. Without this much appreciated help this work could never have been accomplished.

Many thanks to the GTK for providing me the drill core data and the geochemical analyses that were necessary to complete the project. I also wish to thank the GTK for accepting to undertake the U-Pb and Lu-Hf isotope analyses in their labs. Special thanks to Yann Lahaye, the person in charge for the zircon separation and the aforementioned analyses.

I would like to thank my summer internship colleagues and my fellow students back in the department. Our discussions and time spent together, kept my passion for Geology burning during the cold Finnish winter. Special thanks to my friends Giorgos and Christos, who were with me in Finland, making the transition of being away from my homeland a much smoother process.

Also, thank you to all these friends in Finland outside the university, for making my life a fun experience, but also my friends back in Greece. Keeping in touch throughout the years I have been far from home, helped me maintain a good morale even at the hardest of times.

I will be always grateful to my family, and especially my father Theodoros and my mother Elisabeth. They might not understand exactly what it is about rocks that I am so passionate about, but they still support me wholeheartedly, and are by my side whatever adventure I may embark on.

Finally, a truly special person who I hold very dear to my heart. Thank you for helping me grow, and growing with me, fighting against the entropy of this world. I love you.

8. REFERENCES

Abbot, D., Drury, R., Smith, W.H.F. 1994. Flat to steep transition in subduction style. Geology 22 (10), 937–940.

Alapieti, T., 1982. The Koillismaa layered igneous complex, Finland - its structure, mineralogy and geochemistry, with emphasis on the distribution of chromium. Geological Survey of Finland, Bull. 3, 19. 116 p.

Andersen, T. 2012. Age, Hf isotope and trace element signatures of detrital zircons in the Mesoproterozoic Eriksfjord sandstone, southern Greenland: are detrital zircons reliable guides to sedimentary provenance and timing of deposition? Geological Magazine, page 1 of 15, Cambridge University press 2012.

Andersen, T., Elburg, M.A., Van Niekerk, H.S. 2019. Detrital zircon in sandstones from the Palaeoproterozoic Waterberg and Nylstroom basins, South Africa: Provenance and recycling. South African Journal of Geology 122.1, 79-96; https://doi.org/10.25131/sajg.1220008

Anhaeusser, C.R. 2014. Archaean greenstone belts and associated granitic rocks – A review. Journal of African Earth Sciences, Volume 100, 684-732; https://doi.org/10.1016/j.jafrearsci.2014.07.019

Arndt, N., Lesher, C.M. 2004. Komatiite. Encyclopaedia of Geology, Elsevier, 260-268.

Attoh, K. 1986. Lithology, age and structure of early Proterozoic greenstone belts West African Shield. Workshop on Tectonic Evolution of Greenstone Belts. A Lunar and Planetary Institute Workshop, January 16-18th.

Barnes, S.J., Cruden, A.R., Arndt, N., Saumur, B., 2015. The mineral system approach applied to magmatic Ni-Cu-PGE sulphide deposits. Ore Geology Reviews, 76(94) https://doi.org/10.1016/j.oregeorev.2015.06.012

Barnes, S.J., Heggie, G.J., Fiorentini, M.L. 2013. Spatial Variation in Platinum Group Element Concentrations in Ore-Bearing Komatiite at the Long-Victor Deposit, Kambalda Dome, Western Australia: Enlarging the Footprint of Nickel Sulphide Orebodies. Economic Geology (2013), 108 (5), 913–933. https://doi.org/10.2113/econgeo.108.5.913

Barnes, S.J., Hill, R.E.T., Perring, C.S., Dowling, S. 2004. Lithogeochemical exploration for komatiite-associated Ni-sulphide deposits: Strategies and limitations. Mineralogy and Petrology 82(3), 259-293. https://doi.org/10.1007/s00710-004-0051-7

de Beer, J.H., Stettler, E.H. 1991. The deep structure of the Limpopo Belt from geophysical studies. Precambrian Research, volume 55 (1992) 173-186.

Benn, K., Moyen, J.-F. 2008. The Late Archean Abitibi-Opatica terrane, Superior Province: A modified oceanic plateau. Special Paper of the Geological Society of America 440, 173-197. https://doi.org/10.1130/2008.2440(09)

Bibikova, E.V., Samsonov, A.V. Shchipansky, A.A., Bogina, M.M., Gracheva, T.V., Makarov, V.A. 2003. The Hisovaara structure in the northern Karelian greenstone belt as a late Archean accreted Island arc: Isotopic geochronological and petrological evidence. Petrology 11 (3), 261-290.

Bouvier, A., Vervoort, J.D. & Patchett, P.J. 2008. The Lu–Hf and Sm–Nd isotopic composition of CHUR: Constraints from unequilibrated chondrites and implications for the bulk composition of terrestrial planets. Earth and Planetary Science Letters, 273, 48–57.

Brand, N.W. 2004. Geochemical Expressions of Nickel Sulphide Deposits. AIG Seminar, Advances and Innovations in the Exploration for Nickel Sulphide Deposits.

Chew, D.M., Petrus, J.A., Kamber, B.S. 2013. U–Pb LA–ICPMS dating using accessory mineral standards with variable common Pb. Chemical Geology, volume 363, 10 January 2014, 185-199.

Chu, N.C., et al., 2002. Hf isotope ratio analysis using multi-collector inductively coupled plasma mass spectrometry : an evaluation of isobaric interference corrections. Journal of Analytical Atomic Spectrometry 17 (12), 1567-1574.

Condie, K.C. 1981. Archean greenstone belts (Developments in Precambrian geology). Elsevier scientific publishing company. 433 pp. Published 1st April 2000.

Condie, K.C. 1994. Greenstone through time. In: Condie, K. C. (Ed.), Archean Crustal Evolution. Developments in Precambrian Geology. Elsevier, Amsterdam, volume 11, 85-120.

Debaille, V., O'Neil, G., Brandon, A.D., Haenecour, P., Yin, Q.-Z., Mattielli, N., Treiman, A.H. 2012. Stagnant-lid tectonics in early Earth revealed by ^{142}Nd variations in late Archean rocks. Earth and Planetary Science Letters 373, 83-92.

Dostal, J., Mueller, W.U., 2013. Deciphering an Archean mantle plume: Abitibi greenstone belt, Canada, Gondwana Research, volume 23, Issue 2, 493-505.

Engel, W.W., Dietz. G.J. 1989. A modified stratigraphy and tectonomagmatic model for the Suomussalmi greenstone belt, eastern Finland, based on the remapping of the Ala-Luoma area. Bulletin of Geological Society of Finland 61, 143-160.

Fallon, M., Porwal, A., Guj, P., 2010. Prospectivity analysis of the Plutonic Marymia Greenstone Belt, Western Australia. Ore Geology Reviews 38(3), 208-218 https://doi.org/10.1016/j.oregeorev.2010.03.009

Furnes, H., Dilek, Y., & Wit, M.J. 2015. Precambrian greenstone sequences represent different ophiolite types. Gondwana Research 27, 649-685.

Gerdes, A., Zeh, A. 2006. Combined U–Pb and Hf isotope LA-(MC-)ICP-MS analyses of detrital zircons: Comparison with SHRIMP and new constraints for the provenance and age of an Armorican metasediment in Central Germany. Elsevier, Earth and Planetary Science Letters, 249, 47-61.

Griffin, W.L., Pearson, N.J., Belousova, E., Jackson, S.E., van Achterbergh, E., O'Reilly, S. Y., Shee, S.R. 2000. The Hf isotope composition of cratonic mantle: LAM-MC-ICPMS analysis of zircon megacrysts in kimberlites. Geochimica et Cosmochimica Acta, 64, 133–147.

Hanski, E., Huhma, H. 2005. Chapter 4 Central Lapland greenstone belt. Developments in Precambrian Geology Elsevier, Volume 14, 2005, 139-193.

Heinonen, A.P., Andersen, T., Rämö, O.T. 2010. Re-evaluation of Rapakivi Petrogenesis: Source Constraints from the Hf Isotope Composition of Zircon in the Rapakivi Granites and Associated Mafic Rocks of Southern Finland. Journal of Petrology, Volume 51, Issue 8, August 2010, 1687–1709.

Hölttä, P., Heilimo, E., Huhma. H., Juopperi, H., Kontinen, A., Konnunaho, H., Lauri, L., Mikkola, P., Paavola, J. & Sorjonen-Ward, P. 2012. Archaean complexes of the Karelia Province in Finland. Geological Survey of Finland, Special Paper 54, 9−20.

Hölttä, P., Mänttäri, I., Huhma. H., Kurhila, M., Ruotoistenmäki, T., Kontinen, A. 2021. Growth of the Archean sialic crust as revealed by zircon in the TTGs in eastern Finland. Advance online publication of the Bulletin of the Geological Society of Finland, volume 93, 77-104.

Huhma, H., Mänttäri, I., Peltonen, P., Kontinen, A., Halkoaho, T., Hanski, E., Hokkanen, T., Hölttä, P., Juopperi, H., Konnunaho, J., Layahe, Y., Luukkonen. E., Pietikäinen. K., Pulkkinen, A., Sorjonen-Ward, P., Vaasjoki, M. & Whitehouse, M. 2012a. The age of the Archaean greenstone belts in Finland. Geological Survey of Finland, Special Paper 54, 74−175.

van Hunen, J., Moyen J.-M. 2012. Archean subduction: Fact or Fiction? Annual Review of Earth and Planetary Sciences 40, 195-219.

van Hunen, J., van der Berg, A.P., Vlaar, N.J. 2004. Various mechanisms to induce present-day shallow flat subduction and implications for the younger Earth: a numerical parameter study. Physics of the Earth and Planetary Interiors 146, 179-194

Iljina, M. 2003. Project 2106001, Layered Igneous Complexes in Northern Finland 1996-2002, Final Report. Report of project. Geological survey of Finland.

Iljina, M., Salmirinne, H., Heikura, P. 2006. Mineral exploration report of relinquished claim of Kuparivaara, Geological survey of Finland.

Järvinen, V., Halkoaho, T., Konnunaho, J., Heinonen, J.S., Rämö, O.T. (2020a). Parental magma, magmatic stratigraphy, and reef-type PGE enrichment of the 2.44-Ga mafic-ultramafic Näränkävaara layered intrusion, Northern Finland. Mineralium Deposita 55, 1535-1560.

Järvinen, V., Halkoaho, T., Konnunaho, J., Heinonen, J.S., Rämö, O.T. (2020b). The basal dunite of the Precambrian mafic-ultramafic Näränkävaara intrusion: Petrogenetic considerations and implications to exploration. Mineralogy and Petrology 115, 37-61.

Järvinen, V., Halkoaho, T., Konnunaho, J., Heinonen, J.S., Karinen, T., Rämö O.T. (submitted a). Petrogenesis of the Paleoproterozoic Näränkävaara layered intrusion, northern Finland, Part I: the northern peridotites and their relationships with the layered series and recharge events. Submitted to Bulletin of the Geological Society of Finland 01/2022

Järvinen, V., Halkoaho, T., Konnunaho, J., Heinonen, J.S., Kamo, S., Davey, S., Bleeker, W., Karinen, T., Rämö O.T. (submitted b). Petrogenesis of the Paleoproterozoic Näränkävaara layered intrusion, northern Finland, Part II: U-Pb age and Sm-Nd isotope systematics. Submitted to Bulletin of the Geological Society of Finland 01/2022.

Jensen, L.S. 1976. A new cation plot for classifying subalkaline volcanic rocks. Ontario Geological Survey Miscellaneous Paper No. 66 (1976), pp 21.

Johnson, D.M., Hooper P.R., Conrey, R.M., GeoAnalytical Lab, Washington State University 1999. XRF Analysis of Rocks and Minerals for Major and Trace Elements on a Single Low Dilution Li-tetraborate Fused Bead. Advances in X-ray Analysis volume 41, 843-867.

Karinen, T. 2010. The Koillismaa Intrusion, north-eastern Finland – Evidence for PGE reef forming processes in the layered series. Academic dissertation. Geological Survey of Finland Bulletin 404. pp 176.

Karinen, T., Salmirinne, H., Lahti, I., Konnunaho, J., Heinonen, S., Salo, A. 2021. The Koillismaa Deep Hole: insight to anomalous mafic intrusion. ARLIN- Online Workshop 1 (Apatity, 25.02.2021).

Kröner, A., Jaeckel, P., Brandl, G. 2000. Single zircon ages for felsic to intermediate rocks from the Pietersburg and Giyani greenstone belts and bordering granitoid orthogneisses, northern Kaapvaal Craton, South Africa. Elsevier, Journal of African Earth Sciences, volume 30, Issue 4, May 2000, 773-793.

Kröner, A. 2010. The role of geochemistry in understanding evolution. In: Kysky, T.M., Zhai, M.-G. and Xiao, W. (Eds.): the evolving continents: Understanding processes of continental growth. Geological society, London, Special Publications 338, 179-196.

Kröner, A., Wan, Y., Liu, X., Liu, D. 2014. Dating of zircon from high-grade rocks: Which is the most reliable method? Geoscience Frontiers volume 5, Issue 4, July 2014, 515-523.

Lauri, L.S., Andersen, T., Hölttä, P., Huhma, H., Graham, S. 2011. Evolution of the Archaean Karelian Province in the Fennoscandian Shield in the light of U–Pb zircon ages and Sm–Nd and Lu–Hf isotope systematics. Journal of the Geological Society, London, volume 168, 2011, 201–218. https://doi.org/10.1144/0016-76492009-159

Le Bas, M.J. 2000. IUGS Nomenclature Reclassification of the High-Mg and Picritic Volcanic Rocks. Journal of Petrology, volume 41, Issue 10, 1467–1470.

Lehtonen, E. 2016. Painting the volcanic landscape of early Fennoscandia – Geochronology of the Meso- and Neoarchaean Suomussalmi-Kuhmo-Tipasjärvi greenstone complex, Karelia Province, Finland. Unigrafia. Helsinki. 40 pages, 2 tables and 12 figures.

Lehtonen, E., Heilimo, E., Halkoaho, T., Käpyaho, A., Hölttä, P. 2016a. U-Pb geochronology of Archean volcanic-sedimentary sequences in the Kuhmo greenstone belt, Karelia Province – Multiphase volcanism from Meso – to Neoarchean and a Neoarchean deposital basin? Elsevier, Precambrian Research 275, 48-69.

Lehtonen, E., Heilimo, E., Halkoaho, T., Hölttä, P. & Huhma H. 2016b. The temporal variation of Mesoarchean volcanism in the Suomussalmi greenstone belt, Karelia Province, Eastern Finland. International Journal of Earth Sciences, volume 106, 763–781.

Lesher, C.M., Groves, D.I., 1986. Controls on the formation of komatiite-associated nickel-copper sulphide deposits, in Friedrich, G., Genkin, A.D., Naldrett, A.J., Ridge J.D., Sillitoe, R.H., Vokes, F.M. (Editors), Geology and Metallogeny of Copper Deposits. Springer-Verlag, Heidelberg, 43-62.

Li, C., Arndt, N.T., Tang, Q., Ripley, E.M. 2015. Trace element indiscrimination diagrams. Lithos 232, 76-83.

Lindsay, M.D., Perrouty, S., Jessell, M.W., Aillères, L. 2013. Making the link between geological and geophysical uncertainty: geodiversity in the Ashanti Greenstone Belt. Geophysical Journal International, volume 195, Issue 2, November 2013, 903–922.

Ludwig K.R. 2003. Isoplot 3.00: A geochronological toolkit for Microsoft Excel. Berkeley Geochronology Center, Berkeley, 70.

Luukkonen, E.J. 1992. Late Archean and Early Proterozoic structural evolution in the Kuhmo-Suomussalmi terrain eastern Finland. Publications of the University of Turku, Series A. II. University of Turku Biologica-Geographica-Geologica 78. 115p

Morel, M.L.A., Nebel, O., Nebel-Jackobsen, Y.J., Miller, J.S., Vroon, P.Z. 2008. Hafnium isotope characterization of the GJ-1 zircon reference material by solution and laser-ablation MC-ICPMS. Elsevier, Chemical Geology, volume 255, issues 1-2, 231-235.

Müller, W., Shelley, M., Miller, P., Broude, S. 2009. Initial performance metrics of a new custom-designed ArF excimer LA-ICPMS system coupled to a two-volume laser-ablation cell. Journal of Analytical Atomic Spectrometry, 24, 209-214.

Naipal, R., Kroenberg, S., Mason, P.R.D., 2019. Ultramafic rocks of the Paleoproterozoic greenstone belt in the Guiana Shield of Suriname, and their mineral potential. 11th Inter Guiana Geological Conference, Paramaribo, SurinameAt: Mededeling Geologisch Mijnbouwkundige Dienst Suriname 29, 143-146.

Nisbet, E.G., Cheadle, M.J., Arndt, N.T., Bickle, M.J. 1993. Constraining the potential temperature of the Archaean mantle: A review of the evidence from komatiites. Lithos, volume 30 issues 3-4, 291-307.

Papunen, H., Halkoaho, T., Luukkonen, E. 2009. Archean evolution of the Tipasjärvi-Kuhmo-Suomussalmi Greenstone complex, Finland. Geological Survey of Finland, Bulletin 403, pp 68

Patchett, P.J., Tatsumoto, M., 1981. A routine high-precision method for Lu-Hf isotope geochemistry and chronology. Contributions to Mineralogy and Petrology, 75, 263-267.

Piirainen, T. 1998. The geology of the Archean greenstone-granitoid terrain in Kuhmo, Eastern Finland. In: Mattila, E. (Ed.) Archean geology of the Fennoscandian shield. Geological Survey of Finland Special Paper 4, 39-51.

Pokki, J., Kohonen, J., Rämö, O.T., Andersen, T., 2013. The Suursaari conglomerate (SE Fennoscandian shield; Russia) – Indication of cratonic conditions and rapid reworking of quartz arenitic cover at the outset of the emplacement of the rapakivi granites at ca. 1.65 Ga. Precambrian Research 233, 132-143. https://doi.org/10.1016/j.precamres.2013.04.008

Rasilainen, K., Lahtinen, R., Bornhorst, T. 2007. The rock geochemical database of Finland manual Edition: Report of Investigation 164Publisher: Geological Survey of Finland ISBN: 978-951-690-984-7

Salmirinne, H., Iljina, M. 2003. Koillismaan kerrosintuusiokomplexin tulokanavamuodostuman painovoimatulkinta ja alueen malmimahdollisuudet (osa 1). GTK (in Finnish)

Segal, I., Halicz, L., Platzner, I.T., 2003. Accurate isotope ratio measurements of ytterbium by multiple collection inductively coupled plasma mass spectrometry applying erbium and hafnium in an improved double external normalization procedure. Journal of Analytical Atomic Spectometry 18, 1217-1223.

Scherer, E.E., Münker, C., Mezger, K. (2001). Calibration of the lutetium hafnium clock. Science 293, 683-687.

Scherer, E.E., Münker, C., Mezger, K. (2007). The Lu-Hf systematics of meteorites: Consistent or not. Goldschmidt Conference Abstracts 2007. Geochimica et Cosmochimica Acta, 71(15S), A888

Sorjonen-Ward, P., and Luukonen, E., 2005. Archean rocks In: Lehtinen, M., Nurmi, P., and Rämö, O. T. (eds.) The Precambrian Geology of Finland – Key to the evolution of the Fennoscandian shield. Amsterdam: Elsevier, 19-99.

Söderlund, U., Patchett, P.J., Vervoort, J., Isachsen, C.E. (2004). The 176 Lu decay constant determined by Lu-Hf and U-Pb isotope systematics of Precambrian mafic intrusions. Earth and Planetary Sciences Letters 219, 311-324.

Smithies, R. H., Champion, D.C., Cassidy, K.F. 2003. Formation of Earth's early Archaean continental crust. Precambrian Research, volume 127, 1-3, 89-101.

Stein, M., Hofmann, A. W. 1994. Mantle plumes and episodic crustal growth. Nature 372, 63-68.

Tepsell, J., Ramö, O. T., Heinonen, A., Lahaye, Y., Halkoaho, T., Heinonen, J. S., Höytiä, H., Konnunaho, J., Järvinen, V. 2020. Some new insights into the geochronology of the Western Karelia Subprovince, Finnish Lapland. Bulletin of the Geological Society of Finland, volume 92, 2020, 5–17. https://doi.org/10.17741/bgsf/92.1.001

Tomlinson, K. Y., Condie, K. C. 2001. Archean mantle plumes: Evidence from greenstone belt geochemistry. Geological Society of America Special Papers 2001, 352, 341-357. https://doi.org/10.1130/0-8137-2352-3.341

Thurston, P. C. 2015. Greenstone Belts and Granite−Greenstone Terranes: Constraints on the Nature of the Archean World Geoscience Canada, volume 42 (4). https://doi.org/10.12789/geocanj.2015.42.081

Vaasjoki, M., Kärki, A., Laajoki, K. 2001. Timing of Paleoproterozoic crustal shearing in the central Fennoscandian Shield according to U-Pb data from associated granitoids, Finland. Bulletin of the Geological Society of Finland 73(1-2), 87-101.

Vearncombe, J.R., Barton, J.M., Jr., van Reenen D.D., Phillips, G.N., Wilson, A.H. 1986. Greenstone belts: Their components and structure. Conference paper, Lunar and Planetary Institute Workshop on the Tectonic Evolution of Greenstone Belts.

Vervoort, J.D., Patchett, P.J., Söderlund, U., Baker, M. 2004. Isotopic composition of Yb and the determination of Lu concentrations and Lu/Hf ratios by isotope dilution using MC-ICPMS. Geochemistry, Geophysics, Geosystems volume 5, 11.

Vesanto, J. 2003. Kaivoslain 19 §:n mukainen tutkimustyöselostus Kuusamon Kuparivaaran alueella valtauksilla Kuparivaara 1 - 3 suoritetuista malmitutkimuksista. Outokumpu Mining Oy, Report 080/4523/JJV/03. 5 p. (in Finnish).

Vogt, K., Gerya, T.V. 2014. From oceanic plateaus to allochthonous terranes: Numerical modelling. Gondwana Research 25, 494-508.

de Wit, M. J., Ashwall, L. D. 1995. Greenstone belts: what are they? South African Journal of Geology,1995, 98(4), 505-520.

Woodhead, J., Hergt, J., Eggins, S. 2004. Zircon Hf-isotope analysis with an excimer laser, depth profiling, ablation of complex geometries, and concomitant age estimation. Chemical Geology 209,121-135.

9. APPENDICES

9.1. Characteristic drill core images

Figure 22: Representative part of the CALC1 unit, taken from drill hole R339 at the area of U-Pb sampling for sample R339. The schistosity of the rock is visible as well as some veinlets

Fig. 23: Representative part of the KOMBAS unit taken from drill hole R318 (left dry, right wet). The boxes include some mafic volcanic rocks, while some felsic veins are visible (lower part of the lower box)

Fig. 24: Representative sample picture from the CALC2 unit, taken from drill hole R322 (left dry, right wet). The area includes felsic to intermediate rocks and at points the schistosity is obvious. Some veins are included. Notice the similarity of this unit to CALC1.

Fig. 25: Representative sample picture of the unit CALC3, taken from drill hole R332 at the depth of U-Pb sampling for the correspondent R332 sample. There are felsic volcanosedimentary rocks with visible schistosity and quartz veins penetrating them.

9.2. Isotopic and geochemical data

Table 1: The Lu-Hf isotope composition data

samples		176Hf/177Hf	1σ	178Hf/177Hf	1σ	176Lu/177Hf	1σ	176Yb/177Hf	1σ	176Hf/177Hf i	1σ	εHf*	1σ	Time (Ga)
	R332-50m-5Hz-5mJ-3.0cm2-40%-10	0.281073	0.000014	1.467264843	1.24715E-05	0.00	2.6118E-06	0.01273942	6.0702E-05	0.28104	0.000014	-0.2	0.5	2.70
	R332-50m-5Hz-5mJ-3.0cm2-40%-17	0.281154	0.000018	1.467284596	1.44822E-05	0.00	9.23303E-06	0.030084321	0.000119981	0.28109	0.000018	1.4	0.6	2.70
	R332-50m-5Hz-5mJ-3.0cm2-40%-3	0.281104	0.000012	1.467202951	1.21738E-05	0.00	1.46629E-06	0.009535063	5.05112E-05	0.28109	0.000012	1.3	0.4	2.70
	R332-50m-5Hz-5mJ-3.0cm2-40%-32	0.281123	0.000014	1.467210013	1.27103E-05	0.00	1.46888E-06	0.02305606	5.20722E-05	0.28108	0.000014	1.3	0.5	2.70
	R332-50m-5Hz-5mJ-3.0cm2-40%-35	0.281120	0.000012	1.467224689	1.08471E-05	0.00	1.60496E-06	0.023361367	5.86976E-05	0.28108	0.000012	1.0	0.4	2.70
	R332-50m-5Hz-5mJ-3.0cm2-40%-42	0.281126	0.000014	1.467229881	1.2499E-05	0.00	8.8304E-06	0.037089002	0.000352482	0.28106	0.000014	0.6	0.5	2.70
	R332-50m-5Hz-5mJ-3.0cm2-40%-43	0.281078	0.000015	1.467171347	1.37674E-05	0.00	7.508E-06	0.021698754	0.000231546	0.28104	0.000015	-0.4	0.5	2.70
	R332-50m-5Hz-5mJ-3.0cm2-40%-44	0.281133	0.000015	1.46734155	1.20088E-05	0.00	2.83206E-06	0.011489534	8.89436E-05	0.28111	0.000015	2.2	0.5	2.70
	R332-50m-5Hz-5mJ-3.0cm2-40%-5	0.281164	0.000014	1.467231138	1.13826E-05	0.00	4.25945E-06	0.020496645	0.000146737	0.28112	0.000014	2.7	0.5	2.70
	R332-50m-5Hz-5mJ-3.0cm2-40%-50	0.281088	0.000016	1.467181352	1.07011E-05	0.00	6.03546E-07	0.010397149	1.40016E-05	0.28107	0.000016	0.8	0.6	2.70
	R339-50m-5Hz-5mJ-3.0cm2-40%-25a	0.280872	0.000014	1.467229384	1.46443E-05	0.00	2.83307E-06	0.032790006	0.000141571	0.28082	0.000014	-8.0	0.5	2.70
	R339-50m-5Hz-5mJ-3.0cm2-40%-25b	0.280785	0.000014	1.467200794	1.16327E-05	0.00	1.10845E-06	0.025267195	7.86033E-05	0.28075	0.000014	-10.6	0.5	2.70
	R339-50m-5Hz-5mJ-3.0cm2-40%-2a	0.280745	0.000014	1.467238764	1.43912E-05	0.00	1.61473E-06	0.024918166	4.03007E-05	0.28070	0.000014	-6.4	0.5	2.95
	R339-50m-5Hz-5mJ-3.0cm2-40%-2b	0.280751	0.000014	1.46727146	1.16467E-05	0.00	2.77023E-06	0.007577812	6.35569E-05	0.28074	0.000014	-11.0	0.5	2.70
	R339-50m-5Hz-5mJ-3.0cm2-40%-30a	0.280845	0.000013	1.467196697	1.21531E-05	0.00	5.93982E-06	0.024170578	0.000242348	0.28081	0.000013	-2.5	0.5	2.96
	R339-50m-5Hz-5mJ-3.0cm2-40%-30b	0.280741	0.000012	1.467246234	1.27614E-05	0.00	2.23401E-06	0.016507543	5.93327E-05	0.28072	0.000012	-11.7	0.4	2.70
	R339-50m-5Hz-5mJ-3.0cm2-40%-33	0.280811	0.000015	1.467228047	1.16398E-05	0.00	6.35597E-06	0.034665108	0.000130408	0.28075	0.000015	-4.7	0.5	2.95
	R339-50m-5Hz-5mJ-3.0cm2-40%-34	0.280732	0.000014	1.467224183	1.32881E-05	0.00	3.14613E-06	0.026704503	0.000123179	0.28068	0.000014	-6.4	0.5	2.98
	R339-50m-5Hz-5mJ-3.0cm2-40%-35	0.280812	0.000014	1.467238176	1.36161E-05	0.00	1.58178E-06	0.014358592	6.49841E-05	0.28078	0.000014	-3.0	0.5	2.97
	R339-50m-5Hz-5mJ-3.0cm2-40%-37	0.280855	0.000014	1.467246162	1.11877E-05	0.00	3.58558E-06	0.019906216	0.000123413	0.28082	0.000014	-2.1	0.5	2.96
	R339-50m-5Hz-5mJ-3.0cm2-40%-38	0.280822	0.000016	1.467119047	1.30485E-05	0.00	4.82783E-06	0.024870679	0.000117959	0.28078	0.000016	-3.2	0.6	2.97
	R339-50m-5Hz-5mJ-3.0cm2-40%-44	0.280795	0.000015	1.467223374	1.23516E-05	0.00	6.84969E-06	0.018440818	0.000244472	0.28076	0.000015	-4.1	0.5	2.96
	R339-50m-5Hz-5mJ-3.0cm2-40%-45	0.280925	0.000014	1.46725043	1.21306E-05	0.00	4.75341E-06	0.020996887	0.000229474	0.28090	0.000014	-5.4	0.5	2.70

Table 2: The U-Pb isotope composition data for R332

Samples	Points	a-core, b-rim	Sample	207Pb/235U	1s	206Pb/238U	1s	% Concordance	r	207Pb/206Pb
107851	Pt1		R332	14.001	0.216	0.544	0.009	103	0.46	2714
107852	Pt2		R332	13.138	0.196	0.520	0.008	101	0.47	2682
107853	Pt3	a	R332	13.090	0.215	0.520	0.008	101	0.44	2676
~~107854~~	~~Pt3~~	~~b~~	~~R332~~	~~9.669~~	~~0.166~~	~~0.491~~	~~0.008~~	~~114~~	~~0.42~~	~~2262~~
107855	Pt4		R332	13.391	0.205	0.535	0.008	104	0.47	2668
107856	Pt5	a	R332	13.170	0.199	0.518	0.008	100	0.47	2693
107857	Pt5	b	R332	13.256	0.200	0.519	0.008	100	0.47	2701
107858	Pt6		R332	13.475	0.210	0.522	0.008	100	0.46	2719
107859	Pt7		R332	13.551	0.202	0.528	0.008	101	0.48	2708
107860	Pt8		R332	13.032	0.195	0.524	0.008	102	0.48	2657
107863	Pt10		R332	13.171	0.204	0.519	0.008	100	0.46	2690
107868	Pt11		R332	13.072	0.197	0.520	0.008	101	0.47	2674
107869	Pt12		R332	13.510	0.220	0.521	0.008	99	0.44	2725
107870	Pt13		R332	13.594	0.209	0.530	0.008	101	0.46	2707
107871	Pt14		R332	13.282	0.199	0.524	0.008	101	0.48	2688
107872	Pt15		R332	14.168	0.238	0.534	0.009	100	0.43	2764
107873	Pt16	a	R332	12.995	0.196	0.511	0.008	99	0.47	2692
107874	Pt16	b	R332	13.354	0.206	0.517	0.008	99	0.46	2719
107875	Pt17		R332	13.512	0.203	0.525	0.008	100	0.47	2714
107876	Pt18		R332	13.531	0.206	0.527	0.008	101	0.47	2710
107877	Pt19		R332	12.952	0.218	0.507	0.008	98	0.43	2701
107878	Pt20	a	R332	13.145	0.221	0.507	0.008	97	0.43	2725
107879	Pt20	b	R332	13.030	0.224	0.517	0.008	100	0.42	2680
~~107880~~	~~Pt21~~	~~a~~	~~R332~~	~~12.981~~	~~0.198~~	~~0.502~~	~~0.008~~	~~96~~	~~0.47~~	~~2722~~
107881	Pt21	b	R332	13.423	0.204	0.526	0.008	101	0.47	2699
107882	Pt22		R332	13.429	0.208	0.521	0.008	99	0.46	2717
~~107887~~	~~Pt23~~		~~R332~~	~~12.611~~	~~0.204~~	~~0.543~~	~~0.009~~	~~110~~	~~0.45~~	~~2543~~
107888	Pt24	a	R332	13.563	0.207	0.525	0.008	100	0.47	2718
107889	Pt24	b	R332	13.243	0.203	0.514	0.008	99	0.47	2713
107890	Pt25		R332	13.958	0.215	0.539	0.008	102	0.47	2722
107891	Pt26		R332	13.314	0.203	0.527	0.008	102	0.47	2682
107892	Pt27		R332	13.433	0.205	0.528	0.008	101	0.47	2695
~~107893~~	~~Pt28~~		~~R332~~	~~14.059~~	~~0.226~~	~~0.548~~	~~0.009~~	~~104~~	~~0.45~~	~~2707~~
107894	Pt29		R332	13.774	0.210	0.535	0.008	102	0.47	2712
107895	Pt30		R332	12.918	0.201	0.505	0.008	97	0.46	2704
107896	Pt31	a	R332	13.098	0.203	0.519	0.008	101	0.47	2680
107897	Pt31	b	R332	13.167	0.210	0.507	0.008	97	0.45	2727
107898	Pt32		R332	13.239	0.220	0.523	0.008	101	0.44	2684
107899	Pt33	a	R332	13.254	0.222	0.515	0.008	99	0.44	2713
107900	Pt33	b	R332	12.814	0.197	0.510	0.008	99	0.47	2673
107901	Pt34		R332	13.285	0.209	0.523	0.008	101	0.46	2692
107902	Pt35		R332	13.290	0.210	0.524	0.008	101	0.46	2689
107903	Pt36		R332	13.078	0.208	0.527	0.008	103	0.46	2653
107908	Pt37	a	R332	13.459	0.209	0.527	0.008	101	0.46	2700
107909	Pt37	b	R332	12.926	0.201	0.524	0.008	103	0.46	2643
107910	Pt38		R332	13.674	0.212	0.531	0.008	101	0.46	2714
107911	Pt39		R332	13.649	0.210	0.532	0.008	101	0.47	2709
107912	Pt40		R332	12.897	0.203	0.527	0.008	104	0.46	2629
~~107913~~	~~Pt41~~		~~R332~~	~~10.758~~	~~0.210~~	~~0.505~~	~~0.009~~	~~110~~	~~0.39~~	~~2398~~
107914	Pt42	a	R332	13.063	0.202	0.524	0.008	102	0.47	2661
107915	Pt42	b	R332	13.902	0.220	0.535	0.008	101	0.46	2729
107916	Pt43	a	R332	13.389	0.234	0.523	0.009	100	0.42	2703
107917	Pt43	b	R332	13.342	0.211	0.525	0.008	101	0.46	2691
107922	Pt44		R332	13.621	0.214	0.534	0.008	102	0.46	2697
107923	Pt45		R332	12.258	0.195	0.508	0.008	101	0.45	2608
107924	Pt46		R332	12.633	0.198	0.514	0.008	101	0.46	2638
107925	Pt47		R332	13.892	0.231	0.540	0.009	103	0.44	2713
107926	Pt48		R332	13.631	0.217	0.534	0.008	102	0.45	2699
107927	Pt50	a	R332	12.785	0.202	0.519	0.008	102	0.46	2640
107928	Pt50	b	R332	12.870	0.204	0.518	0.008	101	0.46	2656

Table 3: The U-Pb isotope composition data for R339

Samples	Points	a-core, b-rim	Sample	207Pb/235U	1s	206Pb/238U	1s	% Concordance	r	207Pb/206Pb
107935.00000	Pt1		R339	17.74866	0.27989	0.59258	0.00928	101.33916	0.45895	2960.24992
107936.00000	Pt2	a	R339	17.29766	0.27375	0.57930	0.00909	99.68235	0.45861	2955.29482
107937.00000	Pt2	b	R339	13.41785	0.21106	0.50780	0.00794	96.04430	0.45984	2756.28177
107938.00000	Pt3		R339	17.66514	0.27881	0.58768	0.00920	100.47007	0.45847	2966.05396
107939.00000	Pt4		R339	17.10103	0.26985	0.58507	0.00915	101.66412	0.45857	2920.80565
107940.00000	Pt5		R339	17.32050	0.27434	0.58981	0.00923	102.05776	0.45700	2928.38983
107941.00000	Pt6		R339	17.85722	0.28370	0.59265	0.00929	101.01825	0.45597	2969.90812
107942.00000	Pt7	a	R339	17.86204	0.28353	0.59357	0.00930	101.21536	0.45626	2967.82676
107943.00000	Pt7	b	R339	16.01778	0.25463	0.58100	0.00910	104.49406	0.45492	2825.81526
107944.00000	Pt8	a	R339	17.67170	0.28185	0.58834	0.00923	100.60142	0.45401	2964.84330
107945.00000	Pt8	b	R339	17.81425	0.28441	0.62280	0.00976	108.15428	0.45473	2885.74237
107946.00000	Pt9	a	R339	17.83313	0.28539	0.59829	0.00939	102.38827	0.45268	2952.44300
107947.00000	Pt9	b	R339	17.28268	0.27601	0.58160	0.00911	100.26325	0.45315	2947.51194
107948.00000	Pt10	a	R339	17.22932	0.27650	0.57916	0.00909	99.86459	0.45213	2949.30926
107949.00000	Pt10	b	R339	13.58418	0.21778	0.52954	0.00830	101.18056	0.45196	2707.56028
107954.00000	Pt11	a	R339	19.79986	0.31993	0.66842	0.01049	112.14624	0.44871	2942.39275
107955.00000	Pt11	b	R339	16.10629	0.26097	0.58020	0.00911	103.96739	0.44703	2837.02677
107956.00000	Pt12	a	R339	13.59919	0.22068	0.52304	0.00821	99.35106	0.44761	2729.75783
107957.00000	Pt12	b	R339	14.75751	0.23989	0.57729	0.00907	108.72931	0.44686	2701.81917
107958.00000	Pt13		R339	18.01040	0.29340	0.60073	0.00944	102.39456	0.44529	2961.84773
107959.00000	Pt14		R339	17.80818	0.29038	0.59263	0.00931	101.16471	0.44557	2965.52960
107960.00000	Pt15		R339	17.88421	0.29438	0.59245	0.00935	100.89095	0.44220	2972.87248
107961.00000	Pt16		R339	18.12883	0.29735	0.59851	0.00942	101.52640	0.44320	2978.37096
107962.00000	Pt17		R339	18.72387	0.30661	0.63447	0.00997	107.86415	0.44317	2936.33526
107963.00000	Pt18		R339	17.49556	0.28794	0.58730	0.00924	100.91246	0.44120	2951.53080
107964.00000	Pt19		R339	17.35330	0.28602	0.58953	0.00928	101.88515	0.44213	2932.22528
107965.00000	Pt20		R339	18.53623	0.30598	0.61181	0.00963	103.30626	0.44050	2978.76415
107966.00000	Pt21		R339	17.69168	0.29235	0.58781	0.00925	100.41974	0.43942	2968.09686
107967.00000	Pt22	a	R339	18.65050	0.30962	0.62214	0.00981	105.29167	0.43836	2961.69458
107968.00000	Pt22	b	R339	17.78963	0.29599	0.58841	0.00928	100.25617	0.43630	2975.35735
107973.00000	Pt23		R339	17.77931	0.29860	0.59402	0.00938	101.57380	0.43429	2959.12957
107974.00000	Pt24	a	R339	18.50670	0.31120	0.60613	0.00957	102.11640	0.43261	2991.20085
107975.00000	Pt24	b	R339	17.61751	0.29644	0.62323	0.00983	108.93765	0.43220	2866.56919
107976.00000	Pt25	a	R339	18.18379	0.31084	0.61132	0.00971	104.27806	0.42704	2949.11131
107977.00000	Pt25	b	R339	13.26658	0.22495	0.51178	0.00809	97.77672	0.42903	2724.80561
107978.00000	Pt26		R339	17.19644	0.29147	0.58584	0.00925	101.53268	0.42815	2927.67577
107979.00000	Pt27		R339	17.52824	0.29744	0.59204	0.00935	101.90824	0.42989	2941.55887
107980.00000	Pt28		R339	18.02279	0.30746	0.61338	0.00970	105.26573	0.42733	2929.28829
107981.00000	Pt29	a	R339	18.82733	0.32177	0.61883	0.00979	104.01274	0.42533	2985.47620
107982.00000	Pt29	b	R339	18.81893	0.33107	0.61898	0.00992	104.07099	0.41624	2984.37239
107983.00000	Pt30	a	R339	17.77533	0.30511	0.59138	0.00936	100.97883	0.42338	2965.96427
107984.00000	Pt30	b	R339	14.62940	0.25122	0.56211	0.00889	105.27170	0.42345	2731.36015
107985.00000	Pt31		R339	18.08103	0.31080	0.60489	0.00956	103.12857	0.42280	2957.01352
107986.00000	Pt32		R339	17.59132	0.30340	0.59740	0.00945	102.95036	0.42280	2932.81072
107987.00000	Pt33		R339	18.51310	0.31993	0.62367	0.00986	106.06663	0.42200	2945.79219
107992.00000	Pt34		R339	17.79673	0.31188	0.58666	0.00930	99.83506	0.41539	2980.79396
107993.00000	Pt35		R339	17.72508	0.31158	0.58738	0.00932	100.21841	0.41504	2972.31641
107994.00000	Pt36	a	R339	18.73720	0.33026	0.63186	0.01002	107.22854	0.41211	2944.14040
107995.00000	Pt36	b	R339	19.47317	0.34314	0.67288	0.01067	114.19273	0.41329	2904.71976
107996.00000	Pt37		R339	18.48563	0.32771	0.61443	0.00976	104.05252	0.41003	2967.47005
107997.00000	Pt38		R339	17.83532	0.32457	0.58974	0.00949	100.42051	0.40407	2975.85540
107998.00000	Pt39		R339	12.59901	0.22634	0.50974	0.00813	100.35747	0.40690	2646.05304
107999.00000	Pt40		R339	17.45994	0.31103	0.58630	0.00931	100.79244	0.40838	2951.00094
108000.00000	Pt41		R339	18.26490	0.32784	0.61406	0.00977	104.65078	0.40649	2949.07524
108001.00000	Pt42	a	R339	19.23204	0.34437	0.66782	0.01060	113.83352	0.40597	2896.74581
108002.00000	Pt42	b	R339	14.19058	0.25478	0.55038	0.00875	104.07944	0.40513	2715.94385
108003.00000	Pt43	a	R339	18.74290	0.33829	0.62615	0.00996	105.91431	0.40335	2959.30632
108004.00000	Pt43	b	R339	17.51851	0.31665	0.58870	0.00937	101.16328	0.40235	2949.81444
108005.00000	Pt44		R339	17.86013	0.32445	0.59278	0.00945	101.04053	0.40057	2969.80014
108006.00000	Pt45		R339	14.15979	0.26470	0.54213	0.00874	102.01341	0.39117	2737.23816
108007.00000	Pt46		R339	17.45126	0.31979	0.58241	0.00930	99.92168	0.39836	2960.91448
108008.00000	Pt47		R339	18.02475	0.32940	0.60501	0.00964	103.33022	0.39726	2951.68134
108009.00000	Pt48	a	R339	16.97724	0.31181	0.57819	0.00922	100.45075	0.39698	2928.18215
108010.00000	Pt48	b	R339	13.83390	0.25421	0.55480	0.00884	106.93457	0.39401	2660.62195
108011.00000	Pt49		R339	19.34998	0.35708	0.66330	0.01058	112.41768	0.39506	2917.66127
108012.00000	Pt50		R339	17.58351	0.32668	0.58975	0.00943	101.20180	0.39222	2952.90960

Table 4 : Major oxides and important trace elements

HoleID	from	to	SiO_2	TiO_2	Al_2O_3	FeO_tot.	MnO	MgO	CaO	Na_2O	K_2O	Cr_ppm	Cu_ppm	Ni_ppm	Zr_ppm
KUV-1	25.10	26.10	42.7	0.117	2.285	11.5	0.2	43	0.164			3708		2277	
KUV-1	42.00	43.00	51.1	0.257	3.755	8.7	0.2	21.3	14.557	0.118	0.021	2378		545	10
KUV-1	59.00	60.00	50	0.268	4.124	9.4	0.2	21.5	14.392	0.118	0.021	2569	54	573	
KUV-1	78.90	79.90	48.1	0.261	4.179	11.2	0.2	26.2	9.823	0.087	0.033	2838	20	850	
KUV-1	93.50	94.50	46.9	0.23	4.004	11.8	0.2	29.7	7.152	0.077	0.022	3048		1013	
KUV-1	118.10	119.10	43.3	0.154	4.025	13.4	0.2	35.5	3.043	0.099	0.187	3710	35	1393	
KUV-1	127.20	128.20	61.7	0.795	15.101	6.5	0.1	4.9	4.046	3.757	2.756	201		86	234
KUV-3	16.70	17.70	42.6	0.137	2.671	11.8	0.2	42.5	0.068		0.034	3913		2478	
KUV-3	29.90	30.70	49.5	0.2	15.123	6.4	0.1	12	14.46	1.861	0.305	609		218	
KUV-3	56.20	57.10	50.6	0.343	5.555	10.3	0.2	21.6	11.174	0.235	0.054	2398	89	621	16
KUV-3	79.75	80.75	49.8	0.333	5.314	9.5	0.2	21.4	13.187	0.151	0.043	2263	25	587	16
KUV-3	100.80	101.80	45.2	0.288	4.835	12.2	0.2	33.6	3.557		0.046	4136	71	1598	10
KUV-3	115.40	116.40	62	0.744	14.876	6.5	0.1	4.3	4.766	3.132	3.236	176	37	79	216
KUV-3	164.30	165.25	55.1	1.239	14.145	12.7	0.2	5.5	6.818	3.07	1.26	134	179	91	110
R318	11.50	11.75	53	0.72	14.087	10	0.2	8	11.896	1.899	0.167	254	57	51	45
R318	25.75	26.00	64	0.685	14.716	5.6	0.1	4.4	4.957	2.964	2.402	219		88	191
R318	35.20	35.45	50.9	0.917	14.272	12	0.2	7.8	10.939	2.5	0.396	65	102	71	50
R318	42.75	43.00	75.7	0.211	13.954	1.1	0	0.4	2.64	5.371	0.522	17	38	4	211
R318	45.45	45.70	48.4	0.791	11.218	12.3	0.2	13.9	10.406	1.1	1.603	924	91	334	44
R318	47.30	48.30													
R318	48.30	49.30													
R318	49.30	50.30													
R318	50.30	51.30													
R318	55.50	55.70	50.7	1.123	14.058	13.2	0.3	7.5	9.641	3.137	0.315	217		115	63
R318	65.00	65.25	49	0.317	8.558	9.6	0.2	22.7	9.345	0.24	0.044	2136		889	18
R318	69.60	69.80	48.9	0.696	12.735	12.1	0.2	12.9	9.878	1.798	0.631	549	52	360	36
R318	79.70	79.90	67.4	0.496	15.788	3.9	0.1	1.9	3.937	4.24	2.075	52		22	144
R318	90.00	91.00													
R318	91.00	92.00													
R318	102.70	102.90	55.4	0.536	12.304	8.5	0.2	12	7.246	2.051	1.693	1148	47	392	80
R318	114.20	114.40	68.9	0.444	15.02	3.8	0.1	1.8	3.901	4.153	1.865	46		21	124
R319	18.50	18.75	65.3	0.689	14.894	5.2	0.1	3.2	5.339	2.665	2.432	141	38	52	205
R319	22.55	22.75	73.7	0.282	13.79	2	0	0.4	1.429	3.322	4.942	16		6	270
R319	53.40	53.60	50.3	0.909	14.623	12.2	0.2	8.4	9.735	3.05	0.428	256	140	138	48
R319	77.10	77.30	74.4	0.271	13.674	1.7	0	0.6	2.735	4.705	1.83	23		10	235
R319	79.25	79.45	50.1	0.685	15.694	10.4	0.2	9.4	10.744	2.17	0.506	368	70	127	40
R319	83.30	83.50	64.2	0.669	14.488	5.5	0.1	4.2	5.441	2.888	2.229	225		80	191
R319	85.35	85.60	48.6	0.643	13.713	10.9	0.3	8.4	16.285	0.921	0.161	549	27	213	38
R319	88.10	88.35	48.3	0.467	9.724	10.7	0.2	20.2	9.67	0.564	0.087	1708	148	703	26
R319	95.00	95.20	52.6	1.512	13.771	9.6	0.2	7	11.39	3.52	0.321	23	314	52	88
R319	97.15	97.30	47.3	0.722	9.102	12.8	0.2	20	9.485	0.295	0.044	1387	96	497	37
R319	101.40	101.65	49.8	0.906	14.494	12.2	0.2	8.5	10.061	2.249	1.545	168	89	89	52
R319	104.60	105.60	55.5	1.548	13.625	13.1	0.2	4	7.009	3.809	1.032	25			142
R319	105.60	106.60	53.9	1.373	12.791	16.5	0.2	4	6.238	3.816	1.132	53	141	143	126
R319	106.60	107.60	49	0.625	8.875	14.5	0.2	17.1	8.207	0.82	0.625	1162	332	470	47
R319	107.60	108.60	63.9	0.692	13.938	9	0.1	3.8	2.953	3.644	1.827	122	120	139	118
R319	108.60	109.60	57.4	0.733	14.565	9.2	0.2	5.4	9.193	2.231	1.002	183	144	112	75
R319	109.60	110.60	52.6	0.828	14.352	10.9	0.2	7	11.523	1.969	0.471	235	119	84	60
R319	125.70	125.90	58.8	0.744	14.166	9.5	0.2	4.4	8.024	2.44	1.551	39	99	46	114
R319	135.75	135.95	67.8	0.46	15.237	4	0.1	2.2	4.326	3.354	2.362	44	110	20	130
R320	19.20	19.40	49.9	0.902	14.584	12.2	0.2	8.6	10.419	2.403	0.692	257	74	167	50
R320	46.00	46.20	50.1	0.961	14.525	12.6	0.2	8.3	10.867	2.121	0.303	227	123	171	50
R320	53.10	53.30	50.1	0.597	15.198	10.2	0.2	9.9	11.11	2.432	0.273	423	81	170	33

R320	59.60	59.80	51.9	0.657	14.49	10.5	0.2	8.9	10.529	2.418	0.396	334	109	69	40
R320	66.70	66.90	50.4	0.639	15.704	10.1	0.2	9.7	10.343	2.481	0.482	410	89	145	38
R320	84.00	84.20	48.7	0.809	11.596	12.1	0.2	14.1	10.277	1.851	0.266	916	113	361	43
R320	94.40	95.30													
R320	95.30	95.40													
R320	96.20	96.40	55.5	1.579	13.523	13.2	0.2	3.7	7.557	3.923	0.64	29	75	24	146
R320	96.40	97.40													
R320	97.40	98.40													
R321	18.50	18.70	50.1	0.885	14.534	11.9	0.2	8.2	11.058	2.717	0.263	257	69	148	46
R321	32.40	32.60	50.5	0.968	14.409	12.5	0.2	7.6	11.043	2.387	0.337	223	151	133	53
R321	43.45	43.65	50.9	1	14.208	12.3	0.2	7.6	10.735	2.347	0.579	223	82	112	55
R321	46.40	47.40													
R321	47.40	47.60	71.4	0.515	15.155	2.3	0	0.9	3.576	4.799	1.091	22	87	12	245
R321	59.35	59.55	51.1	0.628	14.855	10.2	0.2	9.1	11.298	2.218	0.398	376	95	146	35
R321	99.40	99.60	48.7	0.7	12.059	11.4	0.2	14	10.874	1.292	0.668	1013	115	362	37
R321	108.40	108.60	50.9	0.683	9.815	10.9	0.2	13.6	12.163	1.184	0.469	1634		207	35
R321	117.40	117.60	55.5	1.594	13.647	13.3	0.2	3.9	6.855	4.146	0.667	30	76	27	142
R321	123.15	123.35	55.6	1.557	13.581	13.4	0.2	4.2	6.738	3.876	0.804	23	72	26	149
R321	130.00	131.00													
R321	131.00	132.00													
R321	132.00	132.45													
R321	132.45	133.00													
R321	133.00	134.00													
R321	134.00	135.00													
R321	135.00	136.00													
R321	136.35	136.55	54.5	1.405	14.257	12.4	0.2	5.4	7.286	3.407	1.027	34	50	47	120
R321	137.00	137.55													
R321	137.55	138.00													
R321	138.00	139.00													
R321	139.00	140.00													
R321	140.00	140.90													
R321	140.90	141.00													
R322	15.70	15.90	65.1	0.712	15.555	4.9	0.1	3.2	5.439	3.416	1.403	125		59	205
R322	28.30	28.50	64.7	0.665	14.226	6.7	0.1	4	4.268	2.763	2.426	202	22	72	176
R322	74.90	75.10	72.9	0.306	14.506	2	0	0.5	2.166	4.199	3.177	14		10	164
R322	93.70	93.90	64.8	0.701	14.953	5.7	0.1	3.5	4.847	2.516	2.712	113	27	47	208
R322	115.20	115.40	58.1	0.805	13.491	9.3	0.2	6.3	6.683	3.096	1.882	285	95	112	88
R322	115.40	116.40													
R322	116.40	117.40													
R322	117.40	117.50													
R322	117.50	118.40													
R322	118.40	119.40													
R322	119.40	120.40													
R322	123.00	123.20	69	0.548	16.021	3.3	0.1	1.2	3.174	4.948	1.582	23		8	211
R322	132.40	132.60	51.8	0.621	14.003	9.9	0.2	9.5	11.266	2.285	0.326	393	65	135	35
R324	16.85	17.05	42.4	0.103	1.985	11.4	0.2	43.2	0.605			3723	53	2293	
R324	24.55	24.75	42.5	0.113	2.537	11.2	0.2	43.1	0.317			4006		2366	
R324	40.50	40.70	47.8	0.182	3.347	11.5	0.3	25	11.86	0.053	0.021	2359		740	
R324	48.85	49.05	50	0.224	3.676	8.9	0.2	22.2	14.78	0.107	0.021	2782		559	
R324	70.90	71.10	47.7	0.194	3.651	11	0.2	26.6	10.519	0.097	0.022	2590		826	
R324	82.10	82.30	46.2	0.207	3.239	12.3	0.2	29.1	8.615	0.055	0.022	3133		973	
R325	15.30	15.50	42.9	0.106	2.008	10.4	0.2	43.9	0.446		0.082	3966		2445	
R325	30.80	30.95	41.8	0.094	1.556	10.1	0.2	46.1	0.118		0.012	4058		2545	
R325	51.80	52.00	43.4	0.204	5.755	8.8	0.2	37	4.387		0.305	2171		1983	12
R326	24.95	25.95													

R326	25.95	26.95													
R326	26.95	27.95													
R326	27.95	28.95													
R326	28.95	29.95													
R326	29.95	30.95													
R326	35.90	36.90													
R326	36.90	37.90													
R326	37.90	38.90													
R326	38.90	39.60													
R326	39.60	39.90													
R326	39.90	40.90													
R329	14.00	14.20	42.2	0.078	1.529	9.4	0.2	46.6	0.022			3555		2548	
R329	54.80	55.00	71.8	0.534	14.601	2.4	0	1.3	2.286	5.619	1.269	33		18	228
R329	74.55	74.75	64.5	0.726	15.743	5.3	0.1	4.7	3.261	3.087	2.402	125	22	59	207
R329	94.30	94.50	58.4	0.744	14.365	9.6	0.2	4.5	7.658	3.1	1.364	39	112	46	116
R329	129.70	129.90	51.9	0.775	14.775	11.4	0.2	7.5	10.584	2.389	0.44	256	123	127	56
R329	198.15	198.35	60.6	0.6	17.191	5.7	0.1	3.6	5.961	5.544	0.57	89	47	93	149
R330	22.95	23.15	67	0.487	15.731	4.2	0.1	2.4	3.684	4.364	2.02	56	199	27	138
R330	25.10	25.30	65.8	0.681	16.98	4	0.1	1.6	3.976	4.647	2.064	27	86	6	253
R330	28.30	28.50	67.4	0.485	15.563	4.1	0.1	2.2	3.8	4.184	2.062	56	46	24	133
R330	42.15	42.35	75.3	0.07	13.474	1.2	0	0.1	1.176	3.791	4.816	21		6	239
R330	47.45	47.70	68.3	0.434	15.538	3.7	0.1	1.7	3.834	4.44	1.867	48		23	125
R330	56.65	56.85	70.3	0.477	15.238	2.9	0.1	1	2.926	4.602	2.387	24		6	180
R330	66.20	66.40	70.4	0.373	15.019	3.1	0.1	1.4	3.054	4.828	1.724	38		19	124
R330	67.40	67.60	70.7	0.405	15.194	2.6	0.1	0.9	2.765	4.508	2.836	21		6	152
R331	18.40	18.60	72.2	0.454	14.724	2.7	0	0.8	2.551	4.004	2.501	18		4	271
R331	29.00	30.40													
R332	29.40	29.65	61.7	1.159	20.226	3	0.1	2.6	4.157	5.712	1.291	445	80	157	64
R332	34.50	35.50													
R332	35.50	36.50													
R332	36.50	37.50													
R332	98.40	98.60	68.5	0.589	15.245	3.9	0.1	2.1	3.242	4.116	2.114	54		21	217
R333	30.10	30.30	62.9	0.805	18.03	5.1	0.1	1.5	7.069	3.616	0.886	395	154	121	54
R333	66.70	67.70													
R333	69.80	70.00	52	2.081	12.57	16	0.2	4.5	8.292	3.19	0.919	51	177	44	197
R336	31.65	31.85	48	0.484	8.565	11.1	0.2	21.1	10.194	0.264	0.044	2138		813	19
R336	33.25	33.45	67.7	0.569	15.247	3.7	0.1	3	2.856	6.404	0.366	104		51	208
R337	17.80	18.00	74.4	0.05	14.624	0.8	0	0.2	1.311	5.063	3.469	12		12	66
R338	27.10	27.30	77.2	0.07	13.546	0.7	0	0.3	0.963	6.683	0.602	16		5	43
R338	61.80	62.00	75.9	0.01	14.06	0.5	0	0.1	1.085	4.811	3.435	16	20	2	33
R339	10.16	10.40	64.6	0.707	15.043	5.7	0.1	4.2	4.816	2.686	2.009	150		66	
R339	15.92	16.38	21.1	0.644	4.465	12.5	0.7	8.7	46.158	0.507	0.342	63	40	29	
R339	21.33	21.55	80.2	0.151	9.669	2	0	1	4.111	2.362	0.422	35			
R339	34.50	34.80	72.5	0.423	14.894	2.5	0	0.8	2.435	4.347	1.982				
R339	40.12	40.39	58.8	0.83	17.906	6.3	0.1	4.1	5.695	2.914	3.166	160	61	55	
R339	43.00	44.00													
R339	44.00	44.25													
R339	44.45	44.77	50	1.027	15.509	11.8	0.2	7.5	10.682	2.65	0.452	316	111	155	
R339	48.30	50.30													
R339	62.00	64.00													
R339	77.70	78.00	52.6	0.798	13.704	11	0.2	8.2	9.613	3.733	0.133	322	31	161	
R339	84.00	86.00													
R339	89.00	91.00													
R339	93.17	93.47	50.4	1.003	14.846	12.3	0.2	7.4	10.546	3	0.205	227	117	138	
R339	97.00	99.00													

R339	108.00	110.00												
R339	148.46	148.95	52	0.767	14.315	11.2	0.2	8.2	10.429	2.403	0.337	243	76	61
R339	159.00	161.00												
R339	165.00	166.00												
R339	174.00	176.00												
R339	181.10	181.50	51.1	0.695	15.336	10.1	0.2	8.3	11.655	2.198	0.296	370	72	104
R339	189.00	191.00												
R339	203.35	205.35												
R339	230.60	230.87	50	0.943	12.434	12.3	0.2	9.7	11.709	2.052	0.539	515	141	169
R339	236.00	236.40												
R339	236.40	237.00												
R339	237.00	238.00												
R339	238.00	239.00												
R339	239.00	240.00												
R339	240.00	241.00												
R339	241.00	242.00												
R339	242.00	242.08												
R339	242.08	242.55												
R339	242.55	242.75												
R339	248.70	249.10	48.6	0.826	16.21	11.7	0.2	8.6	10.395	2.018	1.36	177		191
R339	260.05	260.45	50	0.948	14.633	12.5	0.2	8	11.129	2.226	0.33	260	126	149
R339	268.00	269.00												
R339	273.10	273.40	48.4	0.76	12.395	12.9	0.2	12.8	10.395	1.5	0.49	466	71	379
R339	274.00	275.50												
R339	275.50	276.50												
R339	276.50	276.95												
R339	276.95	277.50												
R339	277.75	278.05	72	0.413	14.5	2.9	0.1	1	2.296	3.081	3.625	31		
R339	280.00	281.00												
R339	286.60	288.00												
R339	296.40	296.73	67.3	0.515	15.436	4.2	0.1	2.2	3.682	4.379	2.068	47		24
R339	297.00	298.75												
R339	313.60	314.00	68.3	0.463	15.504	3.9	0.1	2.1	3.463	3.916	2.165	41		21
R339	314.00	316.00												
R339	316.00	318.00												
R339	326.00	328.00												
R339	330.00	331.00												
R339	331.00	332.00												
R339	332.00	333.00												
R339	336.00	336.35	68.6	0.453	15.715	3.6	0.1	1.6	3.939	4.09	1.843	40		24
R339	347.00	347.68												
R339	347.68	348.55												
R339	348.55	349.00												
R339	359.55	360.05	70.5	0.402	14.583	3.2	0.1	1.6	2.253	4.797	2.464	42		
R339	363.95	364.30	66.5	0.464	16.435	3.8	0.1	1.8	4.396	4.436	2.017	40		25
R339	369.23	369.65	66.6	0.524	15.831	4.2	0.1	2.1	4.165	4.457	1.956	50		30
R339	371.30	373.00												
R339	398.50	400.00												
R339	402.90	404.00												
R339	407.60	409.00												
R339	410.05	410.41	61.4	0.666	17.365	5.2	0.1	2.7	5.714	4.826	1.858	59		26
R339	413.00	414.50												
R339	429.00	430.00												
R339	430.00	431.00												
R339	438.30	438.70	63.3	0.656	16.46	5.2	0.1	2.6	5.685	4.403	1.414	62	29	35

R339	440.00	441.00												
R339	461.95	463.00												
R339	463.00	464.00												
R339	482.00	483.00												
R339	489.00	489.34	64.4	0.605	16.127	4.7	0.1	2.5	5.241	4.536	1.623	51		32
R339	490.00	491.00												
R339	491.00	492.00												
R339	493.15	495.00												
R339	497.10	497.50	72.3	0.262	14.687	2.4	0.1	0.8	2.696	4.577	2.183			
R339	513.00	514.00												
R339	532.00	533.00												
R339	533.00	534.00												
R339	536.10	536.50	69.1	0.383	15.71	3.3	0.1	1.2	3.907	4.431	1.742			
R339	552.00	553.00												
R339	553.00	553.50												
R339	560.00	561.00												
R339	571.97	572.34	71.4	0.493	14.195	3.6	0.1	1.1	3.181	3.896	1.862			
R339	586.60	587.40												
R339	587.40	587.60												
R339	608.91	609.18	72.7	0.282	14.589	2.3	0	0.7	2.948	4.729	1.62			
R339	611.80	612.15												
R339	612.15	612.25												
R339	647.00	647.55	74.9	0.121	13.861	1.2	0	0.2	1.647	3.847	4.078			
R339	655.60	656.55												
R339	668.00	669.00												
R339	686.30	687.30												
R339	692.60	693.00	73.6	0.231	14.472	1.8	0.1	0.6	2.07	4.784	2.382			
R339	698.00	699.00												
R339	729.50	730.50												
R339	740.03	740.54	75.5	0.07	13.864	1	0	0.2	1.346	4.38	3.607			
R339	746.30	747.30												
R339	769.80	770.80												
R339	773.50	774.36												
R339	774.36	774.50												
R339	780.10	780.51	69.6	0.443	16.009	3.3	0	1.4	2.265	3.977	2.9			
R339	795.00	796.00												
R339	822.60	823.60												
R339	833.94	834.20	67.5	0.554	16.022	3.7	0.1	1.3	3.96	4.756	1.884	31		
R339	856.15	857.15												
R339	885.34	885.67	67.8	0.565	15.524	3.8	0.1	1.3	3.569	4.425	2.702			
R339	918.36	918.53	61	0.392	12.96	3.4	0.1	3.8	10.161	5.979	1.677		31	
R339	918.53	918.67	30.2	2.357	7.31	9.9	0.3	16.1	27.981	1.084	3.353	103	337	61
R339	918.67	919.10	37.3	3.626	7.322	10.1	0.2	21.5	14.713	1.228	3.626	53	561	108
R339	919.10	920.00												
R339	920.00	921.00												
R339	956.20	956.50	75	0.09	14.073	1	0	0.2	1.618	3.81	4.131			
R339	967.15	968.15												
R339	992.10	993.00												
R339	999.55	999.86	74.3	0.151	14.167	1.3	0	0.3	1.577	4.099	3.959			
R339	1042.00	1043.00												
R339	1047.20	1047.50	68.1	0.392	16.995	2.9	0.1	0.9	3.409	5.39	1.78			
R339	1054.20	1055.20												
R339	1055.20	1056.20												
R339	1099.34	1099.65	73.8	0.191	14.483	1.5	0	0.4	2.203	4.325	2.947			
R339	1100.80	1101.70												

R339	1144.80	1145.75									
R339	1150.78	1150.95									
R339	1203.05	1204.00									
R339	1208.75	1209.55									
R339	1218.67	1218.95	71	0.302	15.688	2.4	0	0.9	3.349	4.787	1.519

9.3. P lots of major oxide variation and combined plots of the Takanen units

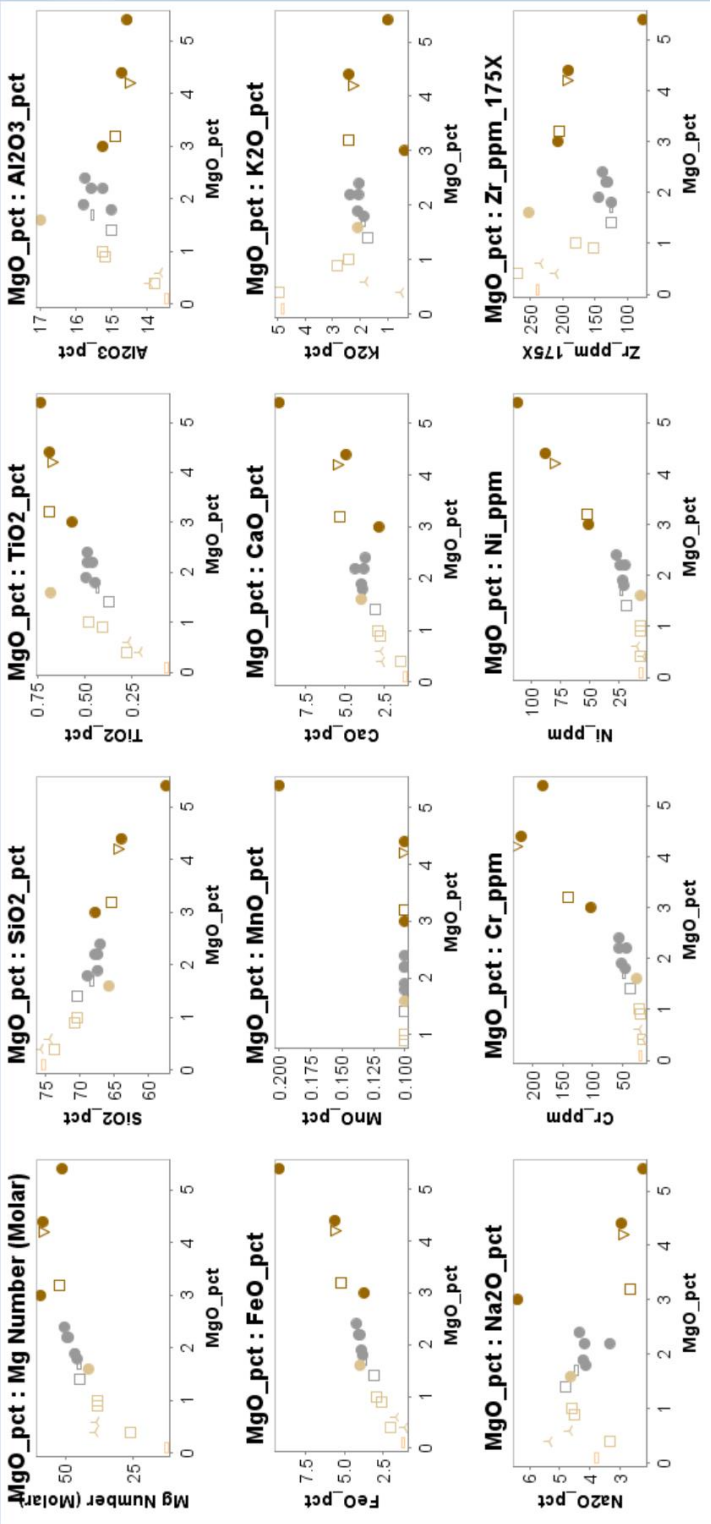

Fig. 26: Major oxides of the CALC1unit

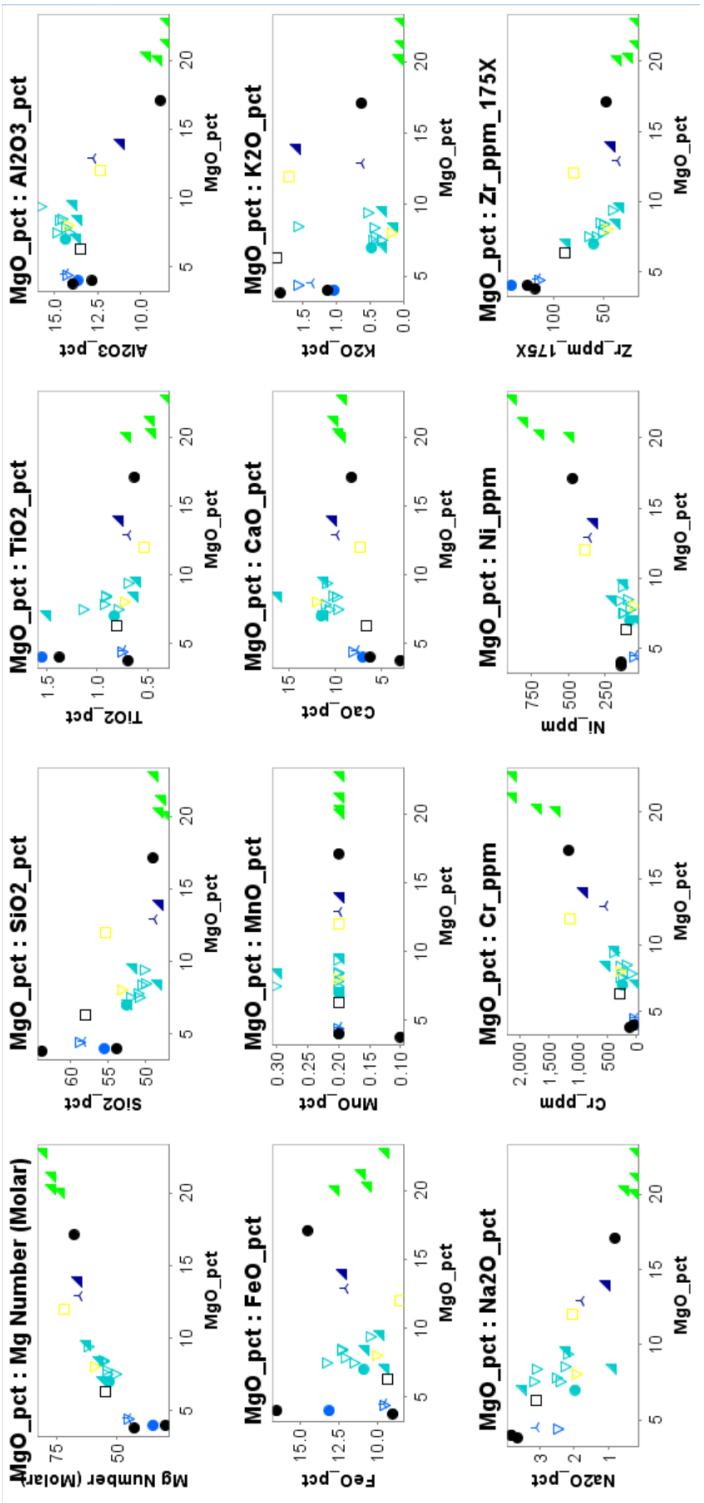

Fig. 27: Major oxides of the KOMBAS unit

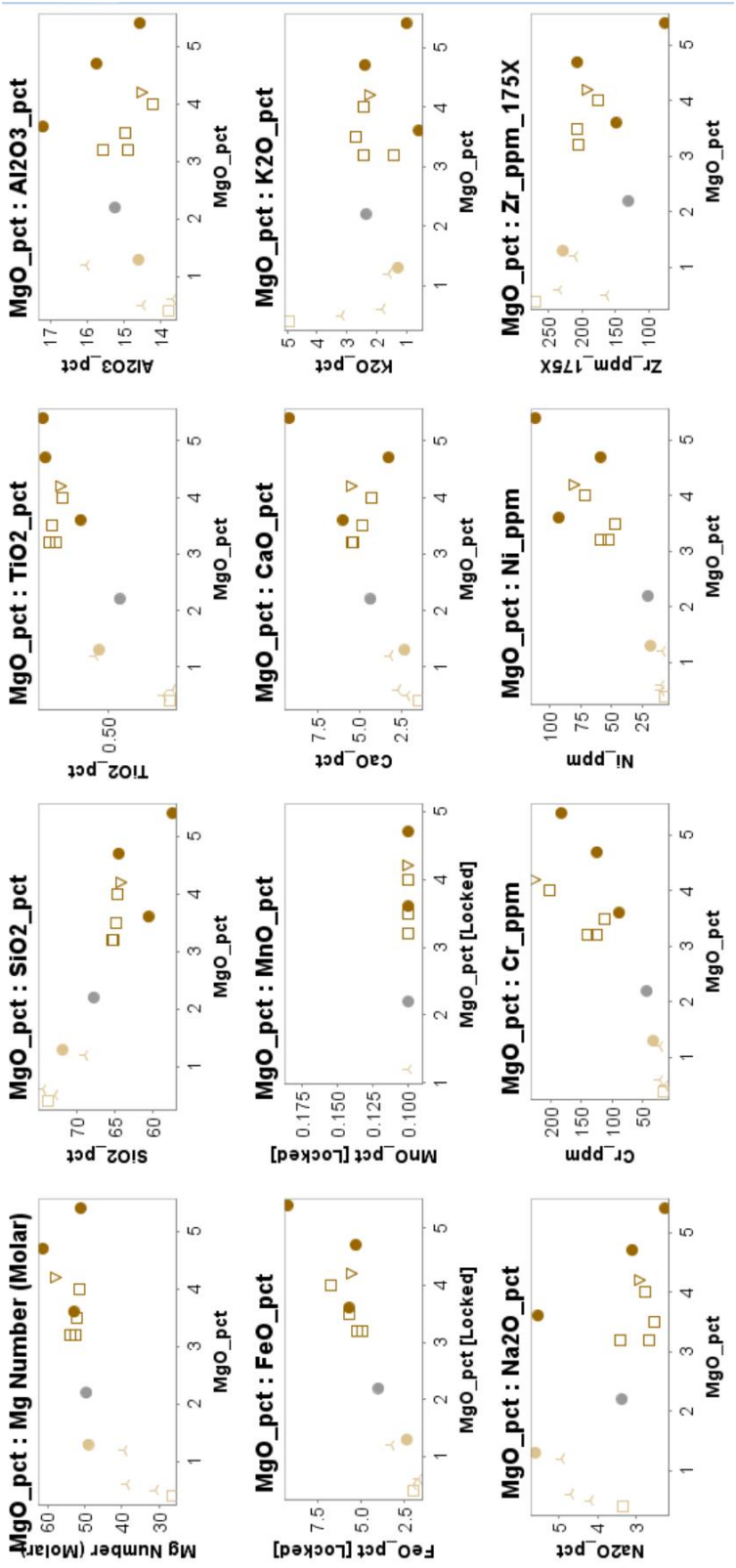

Fig. 28: Major oxides of the CALC2 unit

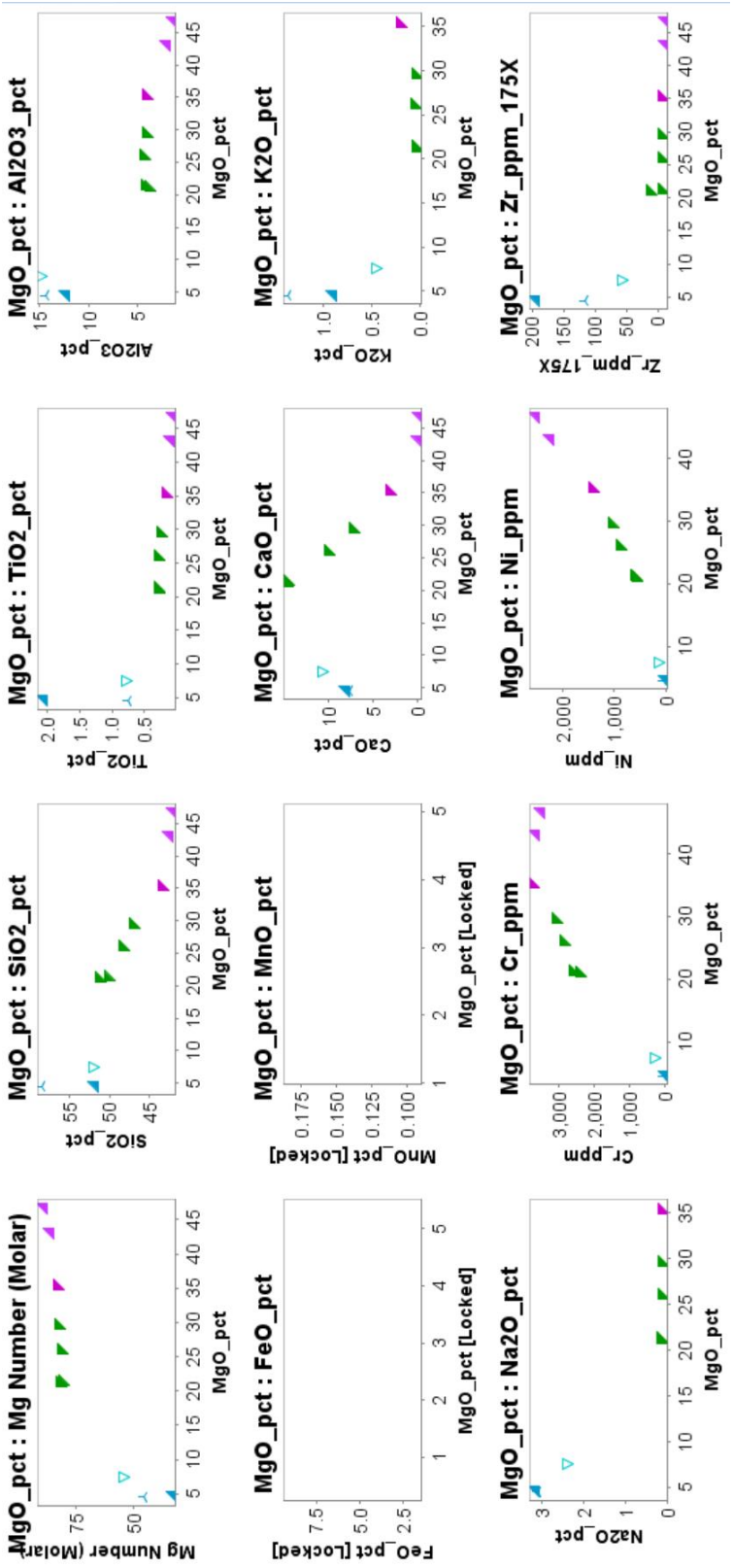

Fig. 29: Major oxides of the OLIAD unit

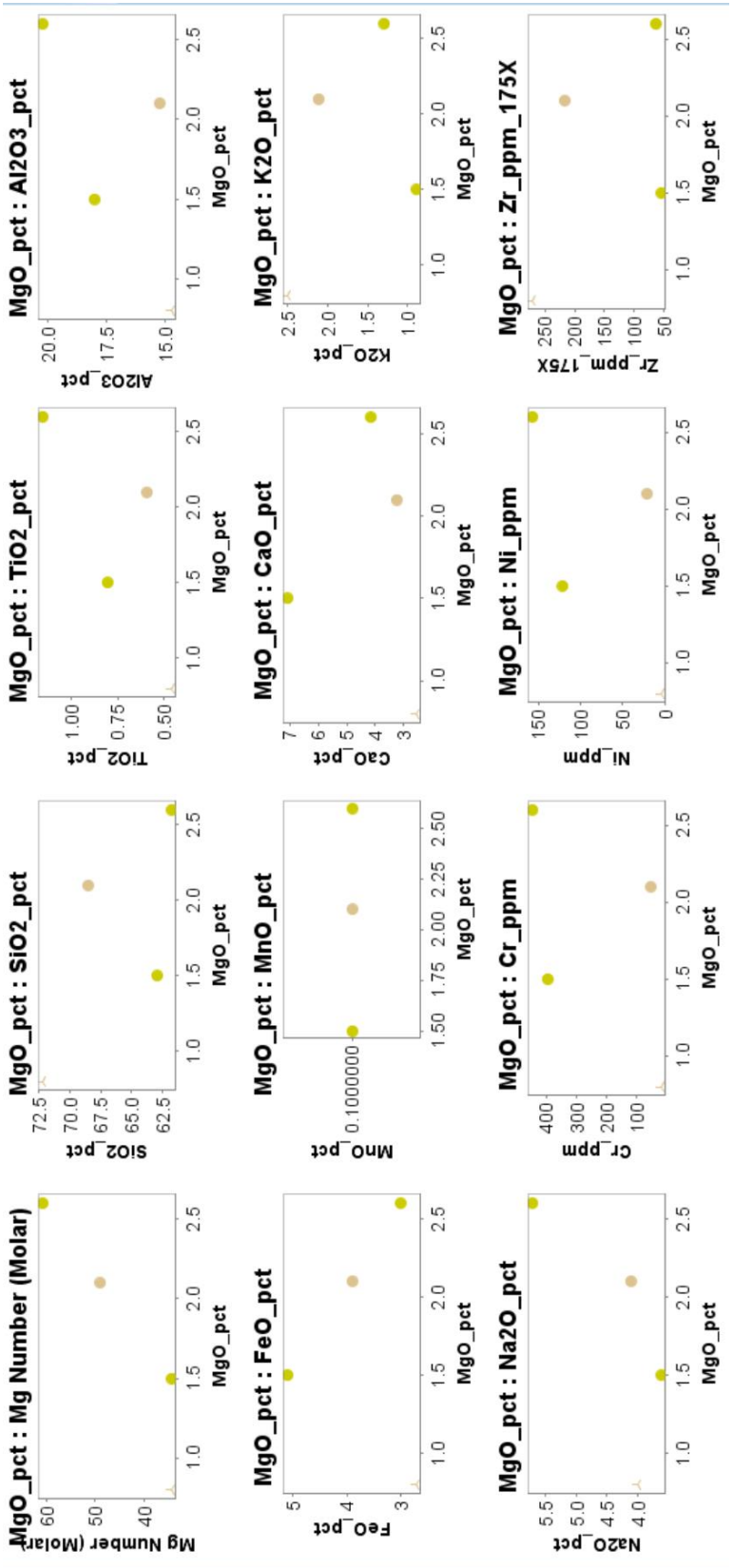

Fig. 30: Major oxides of the CALC3 unit

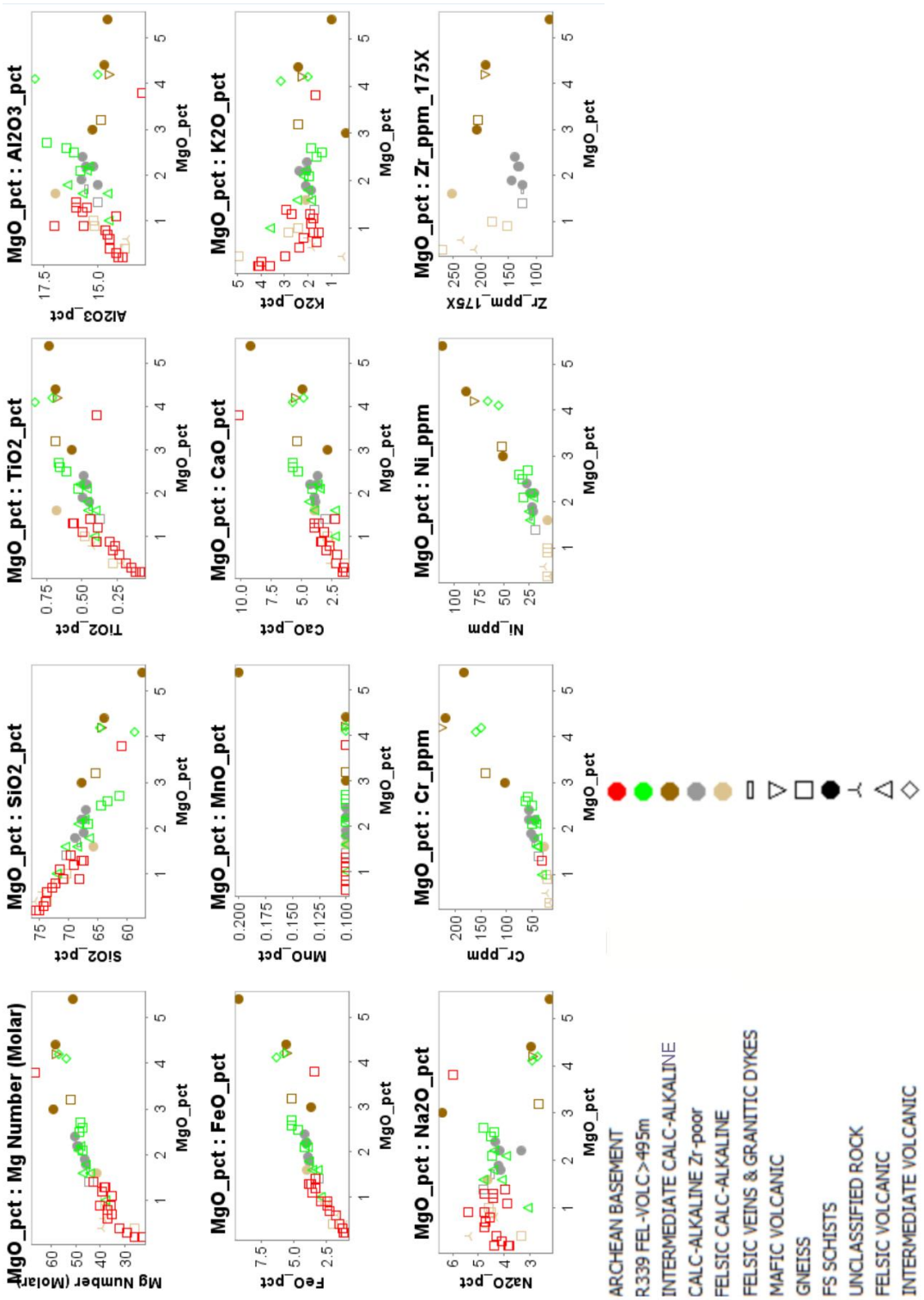

Fig. 31: Combined major oxides of the Archean basement and CALC1.The basement is shown in red color. The green color represents the lowermost volcanosedimentary layers in R339, which in fact belong to CALC1 too.

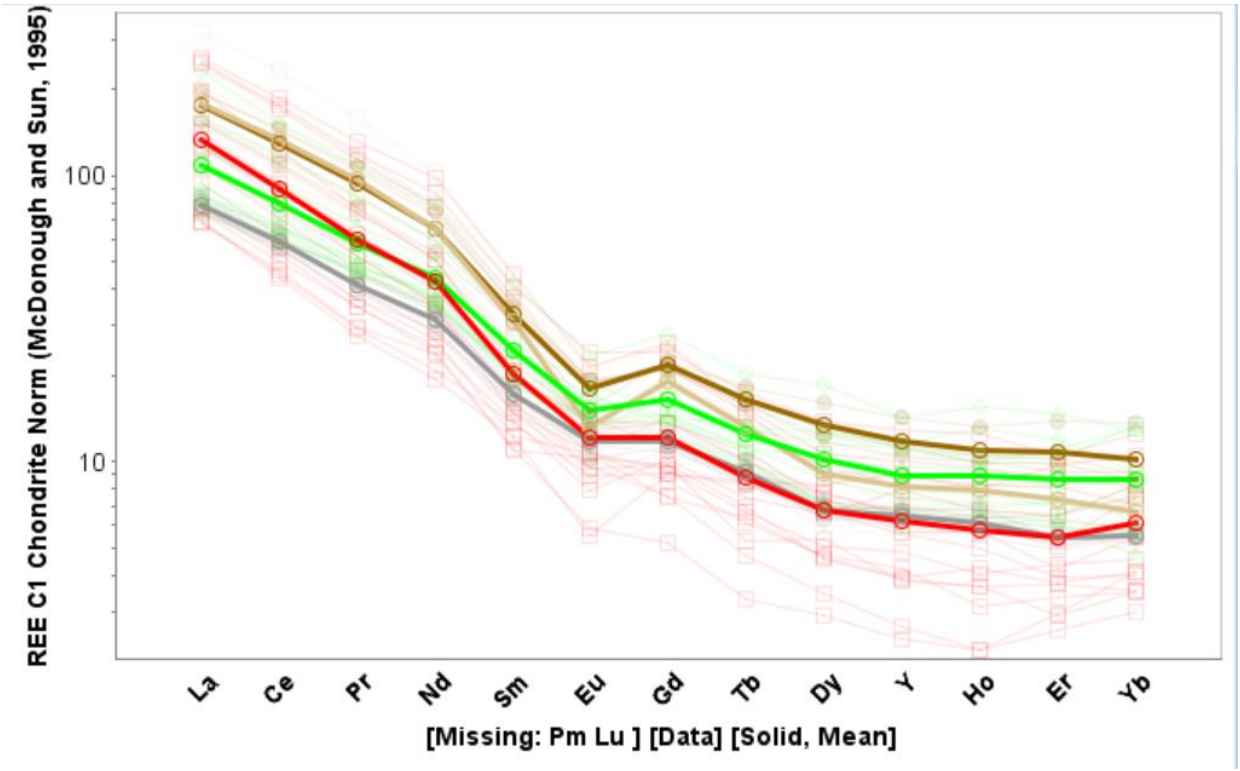

Fig. 32: Combined REE pattern of the Archean basement and CALC1. The basement is shown in red color. The green color represents the lowermost volcanosedimentary layers in R339, which in fact belong to CALC1 too.

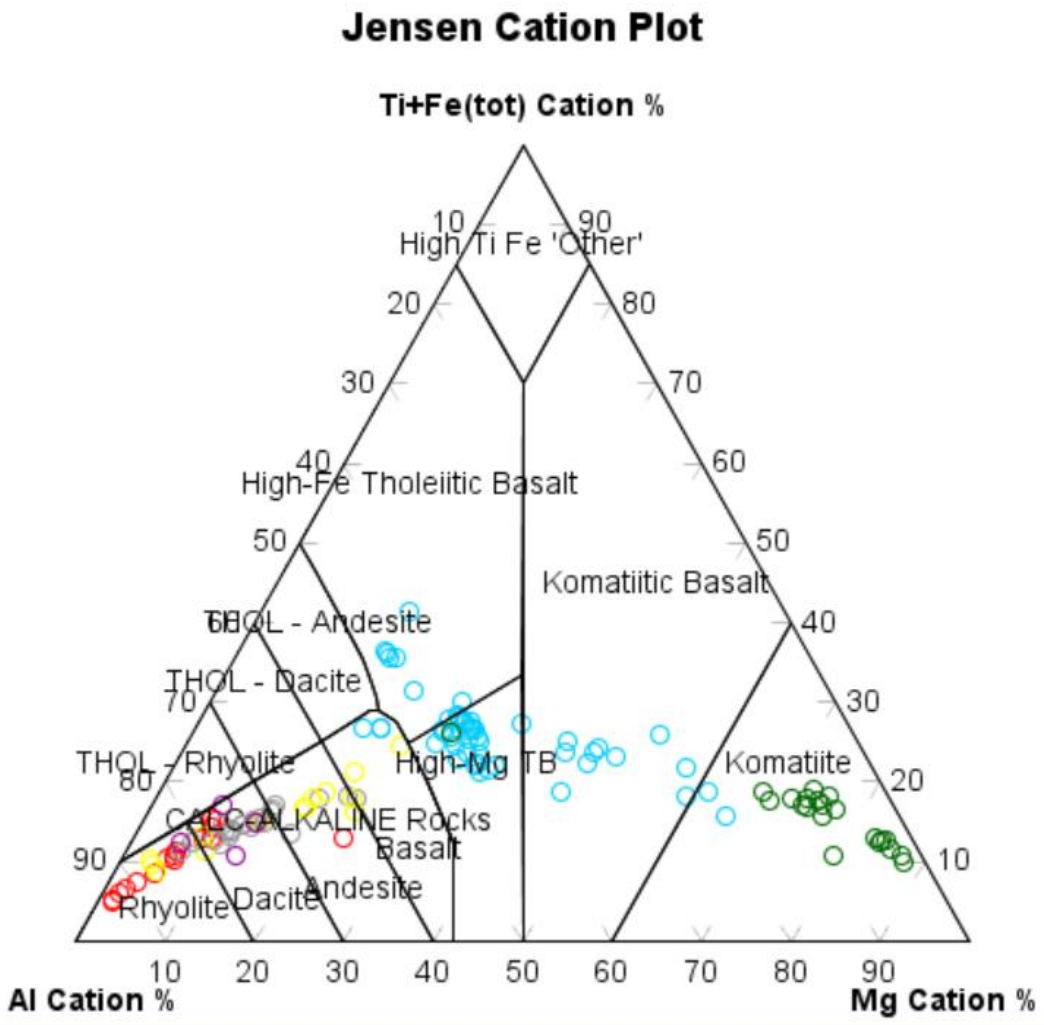

Fig. 33: Simplified collective Jensen diagram of the 5 major units of the TGB. The Archean basement is also presented in this Jensen diagram to better visualize compositional comparison, although it is not volcanic in origin.

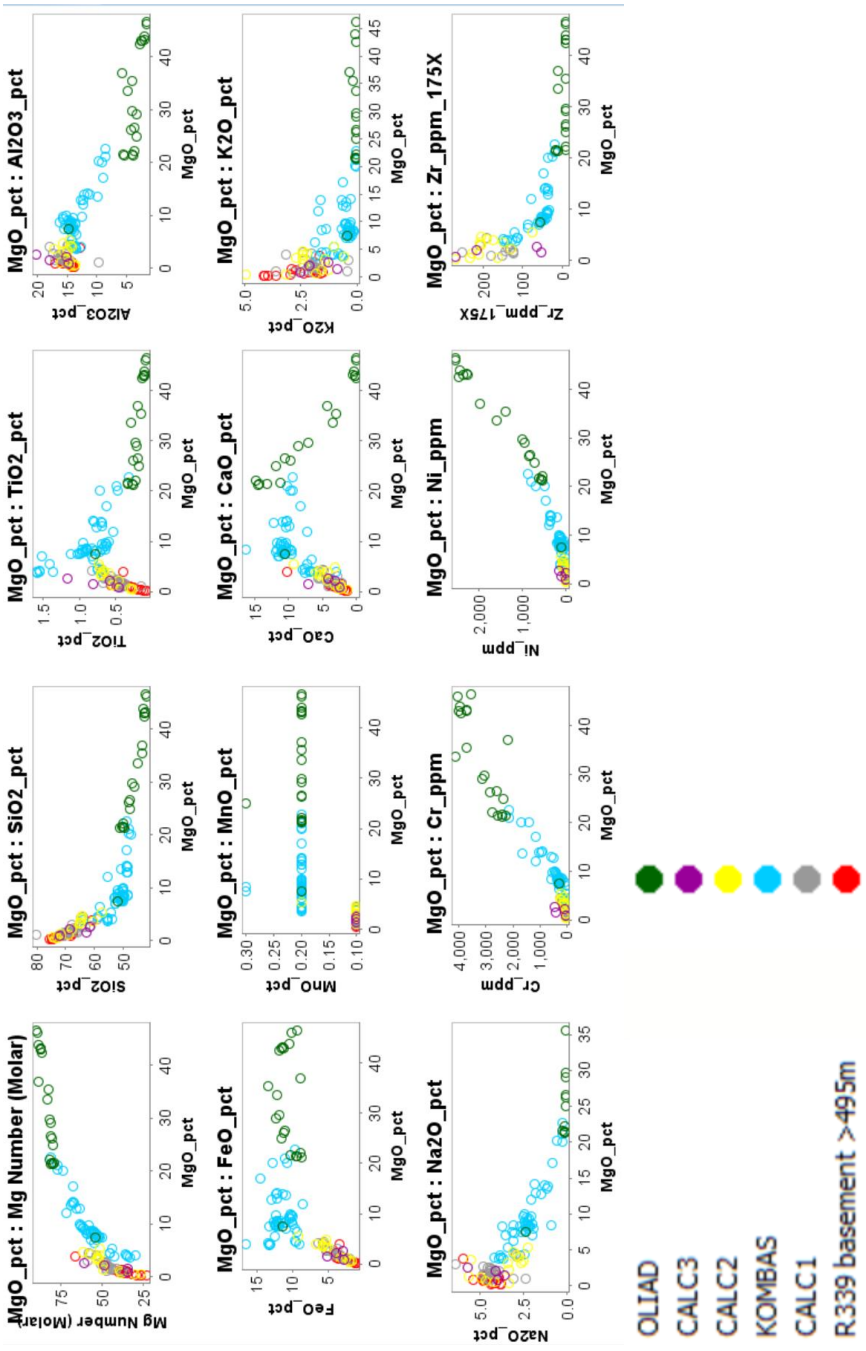

Fig. 34: Simplified collective major oxide diagram of the major 5 units and the Archean basement of the TGB.